Dissertation

submitted to the
Combined Faculties for the Natural Sciences and for Mathematics
of the Ruperto-Carola University of Heidelberg, Germany

for the degree of

Doctor of Natural Sciences

presented by

Diplom-Physiker Sebastian Schätzel

born in Kiel, Germany

Oral examination: 11 February 2004

Measurements of Dijet Cross Sections in Diffractive Photoproduction and Deep-Inelastic Scattering at HERA

Referees: Prof. Dr. Franz Eisele
Prof. Dr. Johanna Stachel

Übersicht

Es wurden differentielle Wirkungsquerschnitte von Zweijet-Ereignissen in diffraktiven ep-Kollisionen des Typs $ep \to eXY$ gemessen, in denen das dissoziative Photonsystem X durch eine große Rapiditätslücke vom baryonischen System Y niedriger Masse getrennt ist und in denen am Protonvertex nur ein geringer Impuls übertragen wird. Die Daten entsprechen einer integrierten Luminosität von 18 pb^{-1}. Zweijet-Ereignisse sind definiert über den inklusiven k_T-Jetalgorithmus. Die Wirkungsquerschnitte sind auf das Niveau stabiler Hadronen korrigiert und umfassen den kinematischen Bereich $Q^2 < 0.01$ GeV^2 (Photoproduktion) bzw. $4 < Q^2 < 80$ GeV^2 (tief-inelastische ep Streuung, DIS) und $165 < W < 242$ GeV, $x_{I\!P} < 0.03$, $E_T^{\mathrm{jet1}} > 5$ GeV and $E_T^{\mathrm{jet2}} > 4$ GeV. Sowohl die Photoproduktions- als auch die DIS-Wirkungsquerschnitte werden im Rahmen der experimentellen Genauigkeit durch Modellvorhersagen beschrieben, die auf diffraktiven Partondichten basieren, die in inklusiver diffraktiver DIS extrahiert wurden. Die Messungen sind kompatibel mit QCD- und Regge-Faktorisierung. Die 'gap survival probability' in diffraktiven Zweijetereignissen der Photoproduktion relativ zum gleichen Prozeß in DIS wurde zu 0.89 ± 0.15 bestimmt. Diese Unterdrückung ist für Prozesse mit einem aufgelösten Photon und einem direkten Photon gleich.

Abstract

Measurements are presented of differential dijet cross sections in low $|t|$ diffractive ep collisions of the type $ep \to eXY$, in which the photon dissociation system X is separated from a leading low mass baryonic system Y by a large rapidity gap. The measurements are based on an integrated luminosity of 18 pb^{-1}. Dijet events are identified using the inclusive k_T cluster algorithm. The cross sections are corrected to the level of stable hadrons and are measured in the kinematic region $Q^2 < 0.01$ GeV^2 (photoproduction) or $4 < Q^2 < 80$ GeV^2 (deep-inelastic ep scattering, DIS) and $165 < W < 242$ GeV, $x_{I\!P} < 0.03$, $E_T^{\mathrm{jet1}} > 5$ GeV, and $E_T^{\mathrm{jet2}} > 4$ GeV. Both the photoproduction and the DIS measurement are described within the experimental precision by model predictions based on diffractive parton distributions obtained in inclusive diffractive DIS. The measurements are compatible with QCD and Regge factorisation. The gap survival probability in diffractive dijet photoproduction relative to the same process in DIS is determined to be 0.89 ± 0.15. This suppression is the same for direct and resolved photon processes.

Contents

List of Tables **iv**

List of Figures **v**

1 Introduction **1**

2 Diffractive scattering at HERA **4**
2.1 Diffractive parton densities 4
2.1.1 Kinematics of inclusive DDIS 4
2.1.2 Diffractive structure function of the proton 6
2.1.3 Regge factorisation and the pomeron 6
2.1.4 Pomeron parton density functions 7
2.2 Diffractive dijet production 9
2.2.1 QCD hard scattering factorisation 9
2.3 Monte Carlo generators 9
2.3.1 RAPGAP implementation of the pomeron model 9
2.3.2 Generator for inclusive dijet production 10
2.3.3 DIFFVM model for proton dissociation 10
2.3.4 Diffractive dijet production in DIS 11
2.3.4.1 Kinematics of diffractive dijet production in DIS 11
2.3.4.2 Previous H1 results on diffractive dijet production in DIS 12
2.3.5 Diffractive dijet production at the Tevatron 14
2.3.6 Diffractive dijet photoproduction 15
2.3.6.1 Resolved photon processes 15
2.3.6.2 Kinematics of diffractive dijets in photoproduction . . . 16
2.3.6.3 Previous H1 results on diffractive dijet photoproduction 16
2.3.7 Motivation for the present analyses 18

3 The HERA collider and the H1 detector **19**
3.1 The HERA collider 19
3.2 The H1 detector 22
3.2.1 Overview 22
3.2.2 Tracking detectors 22
3.2.3 Liquid argon calorimeter (LAr) 24
3.2.4 Backward calorimeter SPACAL 26
3.2.5 Forward detectors 26
3.2.6 Electron and photon detectors 26

4 Correction of detector effects **29**
4.1 Partons, hadrons and detector response . . . 29
4.2 Event variable spectra and migrations . . . 29
4.3 Simulation of the H1 detector response . . . 30
4.4 Bin-to-bin correction method . . . 31
4.5 Reweighting of the correction Monte Carlo . . . 31
4.6 Systematic uncertainties of the correction factor . . . 32
4.7 Irrelevant detector level phase space . . . 32
4.8 Energy flow in the event . . . 32

5 Analysis of dijets in diffractive photoproduction **33**
5.1 Reconstruction of kinematic variables . . . 33
5.2 Monte Carlo modelling of the data . . . 41
5.3 Event selection . . . 42
5.3.1 Basic event selection . . . 42
5.3.2 Triggers and trigger efficiency . . . 42
5.3.3 Raw event rate and integrated luminosity . . . 44
5.3.4 Electron detector cuts . . . 47
5.3.5 Photon detector energy . . . 47
5.3.6 Event vertex requirement . . . 47
5.3.7 Reconstruction of the hadronic final state . . . 49
5.3.8 Dijet selection . . . 49
5.3.9 Selection of diffractive events in photoproduction . . . 51
5.3.9.1 Cut on $x_{I\!P}$ . . . 51
5.3.9.2 Cut on most forward cluster in the LAr calorimeter . . . 51
5.3.9.3 Activity in the FMD . . . 54
5.3.9.4 Hits in the PRT . . . 55
5.4 Control plots for diffractive dijets in photoproduction . . . 56
5.4.1 Description of kinematic variables in photoproduction . . . 56
5.4.2 Energy flow in diffractive photoproduction dijet events . . . 59
5.5 Correction to the level of stable hadrons . . . 64
5.5.1 Cross section formula . . . 64
5.5.2 Correction factor, purity and stability . . . 64
5.5.3 Cut monitoring . . . 65
5.5.4 Inefficiency of the rapidity gap selection . . . 70
5.5.5 Correction for noise in the FMD . . . 70
5.5.6 Correction for proton dissociation . . . 70
5.6 Systematic uncertainties . . . 72
5.6.1 Incomplete understanding of detector parameters . . . 73
5.6.2 Imperfect description of data distributions . . . 73
5.7 Summary . . . 74

6 Analysis of dijets in diffractive DIS **78**
6.1 Reconstruction of kinematic variables . . . 78
6.2 Monte Carlo modelling of the data . . . 85
6.3 Event selection . . . 87

6.3.1 Basic event selection . . . 87
6.3.2 Triggers and trigger efficiency . . . 87
6.3.3 Raw event rate and integrated luminosity . . . 88
6.3.4 Cuts on the electron candidate . . . 88
6.3.5 Event vertex requirement . . . 95
6.3.6 Containment of the event . . . 95
6.3.7 Transverse momentum balance . . . 97
6.3.8 Dijet selection . . . 97
6.3.9 Selection of diffractive events in DIS . . . 99
6.3.9.1 Cut on $x_{I\!P}$ . . . 99
6.3.9.2 Cut on most forward cluster in the LAr calorimeter . . . 99
6.3.9.3 Activity in the FMD . . . 99
6.3.9.4 Hits in the PRT . . . 99
6.4 Control plots for diffractive dijets in DIS . . . 102
6.4.1 Description of kinematic variables in DIS . . . 102
6.4.2 Energy flow in diffractive DIS dijet events . . . 102
6.5 Correction to the level of stable hadrons . . . 105
6.5.1 Cross section formula . . . 105
6.5.2 Correction factor, purity and stability . . . 108
6.5.3 Cut monitoring . . . 108
6.5.4 Inefficiency of the rapidity gap selection . . . 111
6.5.5 Correction for noise in the FMD and proton dissociation . . . 111
6.5.6 Radiative corrections . . . 114
6.6 Systematic uncertainties . . . 114
6.6.1 Incomplete understanding of detector parameters . . . 114
6.6.2 Imperfect description of data distributions . . . 116
6.7 Summary . . . 117

7 Results and interpretation **120**
7.1 Dijet cross sections in diffractive photoproduction . . . 121
7.1.1 Total diffractive dijet cross section in photoproduction . . . 121
7.1.2 Dependence on the fractional momenta x_γ, $z_{I\!P}$ and $x_{I\!P}$ . . . 122
7.1.3 Dependence on jet variables . . . 122
7.1.4 Dependence on other variables . . . 124
7.1.5 Uncertainties of the model prediction . . . 124
7.2 Dijet cross sections in diffractive DIS . . . 128
7.2.1 Total diffractive dijet cross section in DIS . . . 128
7.2.2 Dependence on the fractional momenta x_γ, $z_{I\!P}$ and $x_{I\!P}$ . . . 129
7.2.3 Dependence on jet variables . . . 130
7.2.4 Dependence on other variables . . . 130
7.2.5 Uncertainties of the model prediction . . . 134
7.3 Survival probability in diffractive dijet photoproduction . . . 134
7.4 Summary and outlook . . . 136

List of Tables

2.1 Flux parameters of the pomeron PDF fit 7

5.1 Selection of photoproduction events 42
5.2 Dijet selection 50
5.3 Diffractive selection 56
5.4 Average numbers in the photoproduction analysis 77

6.1 DIS selection cuts 97
6.2 Average numbers of the DIS analysis 119

7.1 Kinematic region of the γp cross section 121
7.2 Kinematic region of the DIS cross section 128

List of Figures

2.1 Diagram of inclusive DDIS 5
2.2 Display of an inclusive DDIS event in the H1 detector 6
2.3 Pomeron parton density functions 8
2.4 Diffractive dijet BGF production process in the pomeron model 11
2.5 Previous results on DDIS dijet production 13
2.6 Diffractive structure function of the antiproton 14
2.7 Diffractive dijet resolved photon process in the pomeron model 15
2.8 Previous results on diffractive dijet photoproduction 17

3.1 The HERA collider and its pre-accelerators 20
3.2 Integrated luminosities recorded by H1 21
3.3 The central H1 detector 23
3.4 The tracking system 24
3.5 The central tracking system, radial view 25
3.6 The H1 luminosity system 27
3.7 Detection of Bethe-Heitler processes in the H1 luminosity system 28

4.1 Picture of our understanding of an ep collision 30
4.2 Migrations 31

5.1 Correlations hadron/detector level γp 35
5.2 Resolutions hadron/detector level γp 36
5.3 Correlations parton/hadron level γp 37
5.4 Resolutions parton/hadron level γp 38
5.5 Correlations for W γp 39
5.6 Electron detector acceptance and trigger efficiency parameterisation . . . 43
5.7 Trigger efficiency for diffractive dijets γp 45
5.8 Event yield vs. integrated luminosity γp 46
5.9 Distributions for inclusive dijet events γp 48
5.10 Dijet distributions inclusive γp 50
5.11 Diffractive selection variables 96 γp 52
5.12 Diffractive selection variables 97 γp 53
5.13 Noise in the FMD γp 54
5.14 Kinematic variables for diffractive dijets 96 γp 57
5.15 Kinematic variables for diffractive dijets 97 γp 58
5.16 Average energy flow in a diffractive dijet event γp 60
5.17 Average track and cluster multiplicity in a diffractive dijet event γp . . . 61
5.18 Average LAr cell energy in a diffractive dijet event γp 62
5.19 Jet profiles for diffractive dijet events γp 63

5.20 Correction factor for detector effects γp 66
5.21 Correction factor for detector effects as a function of W γp 67
5.22 Cut monitoring pomeron γp 68
5.23 Cut monitoring reggeon γp 69
5.24 Detection efficiency for scattered protons 71
5.25 Effect of reweighting in $\hat{p}_T$ γp 75
5.26 Effect of reweighting in $z_{I\!P}$ γp 76

6.1 Correlations hadron/detector level DIS 80
6.2 Resolutions hadron/detector level DIS 81
6.3 Correlations parton/hadron level DIS 82
6.4 Resolutions parton/hadron level DIS 83
6.5 Correlations for W DIS 84
6.6 Correlations for x_γ DIS 86
6.7 Trigger efficiency for inclusive dijets 96 DIS 89
6.8 Trigger efficiency for inclusive dijets 97 DIS 90
6.9 Event yield vs. integrated luminosity DIS 91
6.10 Distributions of electron related variables DIS 93
6.11 Distributions of the electron candidate cluster DIS 94
6.12 Distributions for inclusive dijet events DIS 96
6.13 Distributions of jet variables in inclusive DIS 98
6.14 Diffractive selection variables 96 DIS 100
6.15 Diffractive selection variables 97 DIS 101
6.16 Kinematic variables for diffractive dijets 96 DIS 103
6.17 Kinematic variables for diffractive dijets 97 DIS 104
6.18 x_γ distribution diffractive dijets 97 DIS 105
6.19 Average energy flow in a diffractive dijet event DIS 106
6.20 Average track and cluster multiplicity in a diffractive dijet event DIS . . 107
6.21 Average LAr cell energy in a diffractive dijet event DIS 108
6.22 Jet profiles for diffractive dijet events DIS 109
6.23 Correction factor for detector effects DIS 110
6.24 Correction factor for detector effects as a function of W and x_γ DIS . . . 111
6.25 Cut monitoring pomeron DIS 112
6.26 Cut monitoring reggeon DIS 113
6.27 QED radiative corrections DIS 115
6.28 Effect of reweighting in $x_{I\!P}$ DIS 118

7.1 Total diffractive dijet cross section γp 122
7.2 Cross section differential in x_γ γp 123
7.3 Cross section differential in $z_{I\!P}$ γp 123
7.4 Cross section differential in $\log_{10}(x_{I\!P})$ γp 124
7.5 Cross section as a function of jet variables γp 125
7.6 Cross section as a function of other variables γp 126
7.7 Dependence on the factorisation and normalisation scale γp 127
7.8 Total diffractive dijet cross section DIS 129
7.9 Cross section differential in x_γ^{jets} DIS 130

7.10 Cross section differential in $z_{I\!P}^{\text{jets}}$ DIS 131
7.11 Cross section differential in $\log_{10}(x_{I\!P})$ DIS 131
7.12 Cross section as a function of jet variables DIS 132
7.13 Cross section as a function of other variables DIS 133
7.14 Dependence on the factorisation and normalisation scale DIS 135

Chapter 1

Introduction

Quantum Chromodynamics (QCD) is the generally accepted theory of strong interactions. It is a non-abelian field theory based on the group $SU(3)$. Many phenomena can be successfully described and predicted using perturbative expansion ('perturbative QCD'). Because of the non-abelian character, however, the renormalization procedure leads to a running coupling constant, which is small only at small distances. The perturbative approach to QCD calculations is therefore limited to hard scales $Q \gg \Lambda_{\mathrm{QCD}} \approx 0.2$ GeV.

The total cross section of hadronic interactions is dominated by peripheral collisions. Since the beginnings of particle physics it has been the aim of physicists to understand this regime. In 1935, Yukawa introduced the pion as the exchange particle of the strong force. Because of its low mass, however, according to Heisenberg's uncertainty principle, it can only describe the long range part of the interaction. An extension to this model is provided by Regge phenomenology [1], which can describe hadronic interactions well. However, it has remained a difficult task to understand the domain of soft hadronic interactions within the QCD framework.

A prime example is elastic pp scattering, where the two protons exchange energy and momentum but no discrete quantum numbers. Within QCD, this exchange must be mediated by a colourless state of quarks or gluons. At hadron colliders, a class of events has been observed in which a proton is scattered elastically and a large gap exists between the directions of this proton and the hadrons produced in the interaction. These gaps arise naturally if no net colour is exchanged (absence of colour strings). From the hadronic cross section differential in the squared momentum t transferred at the proton vertex, which at high energies resembles a diffraction pattern, these events have been given the name 'diffractive.'

Diffractive processes with a hard scale can be treated in perturbative QCD by making assumptions on how final colour singlet states occur. In the resolved pomeron model [2], a colourless particle is exchanged in the early stage of the interaction. This exchange,

the so-called pomeron, has a partonic structure. An alternative approach is used in soft colour neutralisation models. They assume that initially exchanged colour is rearranged during the interaction without changing the momentum configuration of the system.

The observation of diffractive events at the HERA ep collider has started a revival of experimental studies on diffractive scattering. Parton densities of the pomeron were extracted in diffractive deep-inelastic scattering (DDIS) at HERA. These parton densities can be used to obtain predictions for hard diffractive final states, such as jets or heavy flavour production. Diffractive dijet and D^* production has been measured and compared to the predictions. It was found that, within the uncertainties of the data distributions, the predictions based on the pomeron densities give a good description of both the normalisation and the shape of the data distributions.

At the Tevatron $p\bar{p}$ collider, diffractive dijet and W production have been measured and compared to predictions based on the pomeron parton densities obtained at HERA. It was found that the predictions overestimate the production rate by approximately a factor of 10. This discrepancy has given rise to a lot of models which predict a survival probability of less than unity for diffractive events in hadron-hadron collisions. The basic idea behind these models is that the additional hadronic system which is present in $p\bar{p}$ compared to ep collisions, leads to additional interactions which destroy the diffractive signature of the event. These models have free parameters and have been adjusted to describe the Tevatron data.

The transition from DDIS to $p\bar{p}$ scattering can be studied in photoproduction (γp scattering) at HERA. In contrast to DIS, the photon is on-shell in photoproduction which means that it can fluctuate into an hadronic system before interacting with the proton. In that sense, the γp reaction is similar to a hadron-hadron collision.

In this thesis, cross sections for diffractive dijet photoproduction are measured and compared with predictions based on HERA pomeron densities. The models which describe the suppression at the Tevatron must also be able to predict the production rates in diffractive photoproduction. The knowledge of the gap survival mechanism is essential for the prediction of double diffractive Higgs production at the LHC. Soft colour neutralisation models have also been successful in the simultaneous description of diffractive production rates at both HERA and the Tevatron. The photoproduction measurement presented in this thesis will also provide a testing ground for them. However, in this thesis the measured distributions will be compared only to predictions based on the pomeron parton densities. Unfortunately, it was not possible to obtain predictions for the other models. Further comparisons must therefore be postponed to the future.

The pomeron parton densities are dominated by the gluon distribution. In contrast to inclusive DDIS measurements which are mainly sensitive to the diffractive quark content, dijet production is sensitive to the gluon. In this thesis, the survival probability in hard diffractive photoproduction is determined by measuring the suppression in diffractive dijet photoproduction relative to the same process in DDIS. The photoproduction analysis presented here uses the inclusive k_T cluster algorithm to indentify jets and applies asymmetric cuts on the transverse energy of the jets. The existing analysis of dijet production in diffractive DIS used a cone jet algorithm and did not apply asymmetric jet cuts. In addition, the kinematic range in which the DIS measurement was performed was differ-

ent. To determine the suppression in photoproduction as directly as possible without any uncertainty related to different algorithms and kinematic ranges, the analysis was repeated in DIS with the same jet algorithm and kinematic cuts as in photoproduction. Furthermore, the asymmetric jet cuts allow comparisons with NLO predictions which will become available in the near future.

The text is organised as follows. First, the underlying physics of diffraction at HERA is reviewed. The extraction of pomeron parton densities and the predictions for dijet production in diffractive DIS and photoproduction are explained and the kinematic variables are introduced. In the second chapter, the HERA collider and the H1 experiment are introduced where the data under study have been recorded in the years 1996–97. In the next chapter some general aspects concerning the correction of detector smearing are addressed. The analyses of diffractive dijet photoproduction and DIS are described in chapters 5 and 6, respectively. The results are presented and compared with predictions based on diffractive PDFs determined in inclusive diffractive DIS in the last chapter. Throughout the text natural units are used in which $c = \hbar = 1$.

This work was funded by the German National Merit Foundation.

Chapter 2

Diffractive scattering at HERA

2.1 Diffractive parton densities

This section describes how diffractive parton densities are extracted in ep collisions at HERA. The procedure is analogous to the extraction of the parton content of the proton in inclusive deep-inelastic ep scattering (DIS). Diffractive parton densities of the proton are determined in diffractive DIS (DDIS).

2.1.1 Kinematics of inclusive DDIS

Fig. 2.1 shows the inclusive DDIS process $ep \to eXY$ in the pomeron model. The electron (with 4-momentum k) exchanges a photon (q) which interacts with a quark in the proton. The proton momentum is denoted by P. Kinematic variables are defined as

$$s \equiv (k+P)^2; \qquad Q^2 \equiv -q^2; \qquad x \equiv \frac{Q^2}{2P \cdot q}, \tag{2.1}$$

where $\sqrt{s}$ is the ep centre-of-mass energy, Q^2 is the virtuality of the exchanged photon and x is the longitudinal proton momentum fraction carried by the struck quark. The inelasticity variable y and the photon-proton centre-of-mass energy W are given by

$$y \equiv \frac{q \cdot P}{k \cdot P} \approx \frac{Q^2}{xs}; \qquad W^2 \equiv (q+P)^2 \approx ys - Q^2, \tag{2.2}$$

where proton and electron masses have been neglected in the approximations.

For the separation of the final state hadrons into the systems X and Y, the stable hadrons are sorted in rapidity (not pseudorapidity) in the photon-proton centre-of-mass system. The largest rapidity gap between two neighbouring particles then separates the

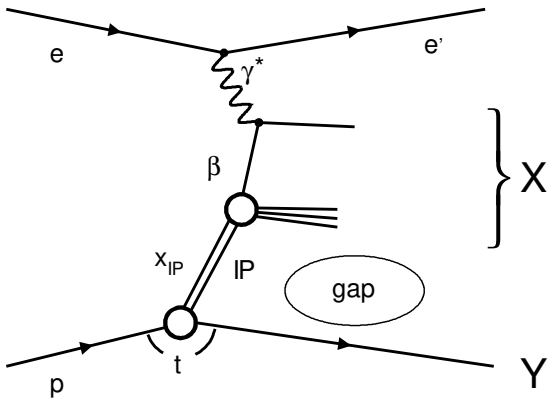

Fig. 2.1. Inclusive DDIS process in the resolved pomeron model. The virtual photon scatters off a parton from the pomeron with momentum fraction β. The pomeron ($I\!P$) carries a fraction $x_{I\!P}$ of the proton momentum. A gap is observed between the systems X and Y.

systems X and Y of which Y is the proton system. The squared 4-momentum t transferred at the proton vertex and the mass M_Y of the proton system are given by

$$t \equiv (P - p_Y)^2; \qquad M_Y \equiv (p_Y)^2, \tag{2.3}$$

with p_Y denoting the 4-momentum of the Y system, The analyses under discussion here are limited to $-t < 1$ GeV^2.

The longitudinal proton momentum fraction $x_{I\!P}$ transferred to the system X is given by

$$x_{I\!P} \equiv \frac{q \cdot (P - p_Y)}{q \cdot P} = \frac{Q^2 + M_X^2 - t}{Q^2 + W^2 - m_P^2} \approx \frac{Q^2 + M_X^2}{Q^2 + W^2}, \tag{2.4}$$

in which m_P and M_X are the invariant masses of the proton and the X system, respectively. The invariant mass M_X of the X system is given by

$$M_X^2 = x_{I\!P}\, W^2 + t - Q^2.$$

Diffractive events are a characterised by small values of $x_{I\!P}$ (< 0.1). Then even a small transferred transverse momentum separates the systems X and Y in space ('rapidity gap').

The quantity β is defined as

$$\beta \equiv \frac{x}{x_{I\!P}} = \frac{Q^2}{2q \cdot (P - p_Y)} = \frac{Q^2}{Q^2 + M_X^2 - t} \approx \frac{Q^2}{Q^2 + M_X^2} \tag{2.5}$$

In the resolved pomeron model, β is the pomeron momentum fraction carried by the struck quark.

Fig. 2.2 shows an inclusive DDIS event in the H1 detector. The initial state proton (p) enters from the right. It is scattered quasi-elastically (p') and escapes detection through the beam pipe. The initial electron enters from the left and is scattered into the detector. No signals are detected between the centrally produced hadronic system X and the outgoing proton. This region spans the rapidity gap.

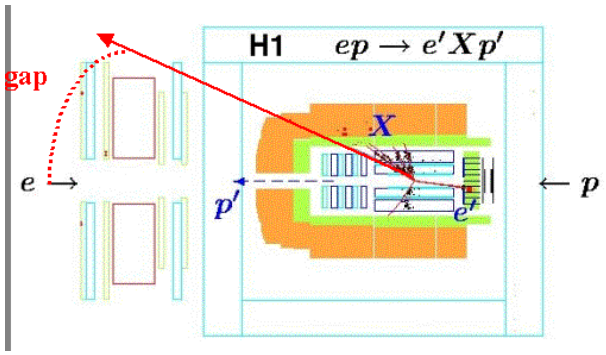

Fig. 2.2. An inclusive DDIS event in the H1 detector. The scattered electron is detected, whereas the scattered proton system p' escapes through the beam pipe. Between the centrally produced system X and p' no signals are detected (rapidity gap).

2.1.2 Diffractive structure function of the proton

The cross section for inclusive DDIS is related to the diffractive structure function F_2^D of the proton. In principle, the cross section depends on five characteristic variables:

$$\frac{d^5\sigma_{ep\to eXY}}{dx_{I\!P}d\beta dQ^2 dM_Y dt} = \frac{4\pi\alpha_{\text{em}}^2}{\beta^2 Q^4}\left(1 - y + \frac{y^2}{2(1+R^{D(5)})}\right) F_2^{D(5)}.$$

$R^{D(5)}$ is the ratio of longitudinal to transverse photon cross sections. It is neglected in the following. In the measurements under discussion here, the system Y was not directly detected and the cross section is integrated over $M_Y < 1.6$ GeV and $-t < 1$ GeV^2, leaving a three-fold differential cross section and the structure function $F_2^{D(3)}(x_{I\!P}, \beta, Q^2)$:

$$\frac{d^3\sigma_{ep\to eXY}}{dx_{I\!P}d\beta dQ^2} = \frac{4\pi\alpha_{\text{em}}^2}{\beta^2 Q^4}\left(1 - y + \frac{y^2}{2}\right) F_2^{D(3)}(x_{I\!P}, \beta, Q^2).$$

2.1.3 Regge factorisation and the pomeron

In the pomeron model, diffractive scattering is mediated by an hadronic object called the pomeron. This object is composed of gluons and quarks and its structure is described in terms of parton distribution functions. The model is based on the assumption of Regge factorisation which implies that $F_2^D(x_{I\!P}, \beta, Q^2)$ can be decomposed into a pomeron flux factor $f_{I\!P/p}$ depending on $x_{I\!P}$ (and t) and a pomeron structure function $F_2^{I\!P}(\beta, Q^2)$:

$$F_2^{D(3)}(x_{I\!P}, \beta, Q^2) = f_{I\!P}(x_{I\!P})\ F_2^{I\!P}(\beta, Q^2).$$

The flux factor $f_{I\!P/p}$ can be interpreted as the probability of finding a pomeron in the proton.

Within the experimental precision of the data, the H1 F_2^D measurements can indeed be described with this factorising ansatz if diffraction is considered as a sum of pomeron and reggeon exchanges:

$$F_2^D(x_{I\!P}, \beta, Q^2) = f_{I\!P/p}(x_{I\!P})\, F_2^{I\!P}(\beta, Q^2) + f_{I\!R}(x_{I\!P})\, F_2^{I\!R}(\beta, Q^2).$$

Parameter	Value
$\alpha'_{I\!P}$	0.26 ± 0.26 GeV^{-2}
$B_{I\!P}$	$4.6^{+3.4}_{-2.6}$ GeV^{-2}
$\alpha'_{I\!R}$	0.90 ± 0.10 GeV^{-2}
$B_{I\!R}$	2.0 ± 2.0 GeV^{-2}
$\alpha(0)_{I\!R}$	0.50 ± 0.16

Tab. 2.1. Pomeron and reggeon flux parameters used for the pomeron PDF extraction in [3].

Due to different flux factors, the reggeon contribution is only a small correction for $x_{I\!P} < 0.01$. The flux factors are parameterised in a Regge-inspired form:

$$f(x_{I\!P}) = \int_{t_{\rm cut}}^{t_{\rm max}} dt \frac{1}{{x_{I\!P}}^{2\alpha_{\{I\!P,I\!R\}}(t)-1}} e^{B_{\{I\!P,I\!R\}}\, t},$$

in which $t_{\rm cut} = -1.0$ GeV^2 and $t_{\rm max}$ is the kinematically allowed maximum value of t. Linear pomeron and reggeon trajectories are assumed:

$$\alpha_{\{I\!P,I\!R\}}(t) = \alpha_{\{I\!P,I\!R\}}(0) + t\,\alpha'_{\{I\!P,I\!R\}}.$$

In a recent analysis of H1 F_2^D data [3], the following value for $\alpha_{I\!P}$ was obtained from a fit to the $x_{I\!P}$ dependence of the data

$$\alpha_{I\!P}(0) = 1.173 \pm 0.018\ (\text{stat.}) \pm 0.017\ (\text{syst.})^{+0.063}_{-0.035}\ (\text{model}).$$

The other flux parameters used in the fit are listed in Tab. 2.1. With these parameters, the H1 F_2^D data can be described within the experimental uncertainties.

2.1.4 Pomeron parton density functions

The diffractive quark and anti-quark densities of the proton are related to $F_2^{I\!P}$ by

$$F_2^{I\!P}(\beta, Q^2) = \sum_i e_i^2\, \beta(q_i(\beta, Q^2) + \bar{q}_i(\beta, Q^2)), \tag{2.6}$$

in which the sum runs over all quark flavours, and the quark charges in units of the proton charge are denoted by e_i. Parton densities are not constant because quarks can radiate gluons and gluons can create quark anti-quark pairs as well as split into several gluons. In the DIS regime for $Q^2 > 4$ GeV^2 and $\beta > 0.01$, the DGLAP equations describe the evolution of the parton densities.

The pomeron parton densities are determined in DGLAP fits to F_2^D. The PDFs are parameterised at a starting scale $Q_0 = 3$ GeV^2. Then they are evolved to larger Q^2 according to the DGLAP equations and compared to the F_2^D measurement. The result of the fit are the parameterisations of the PDFs which give the best description of F_2^D.

Fig. 2.3 shows the parton distributions of the pomeron obtained in the recent analysis [3]. They are shown as a function of the momentum fraction z which in the notation of this chapter is β. The gluon carries $\approx 80\%$ of the pomeron momentum.

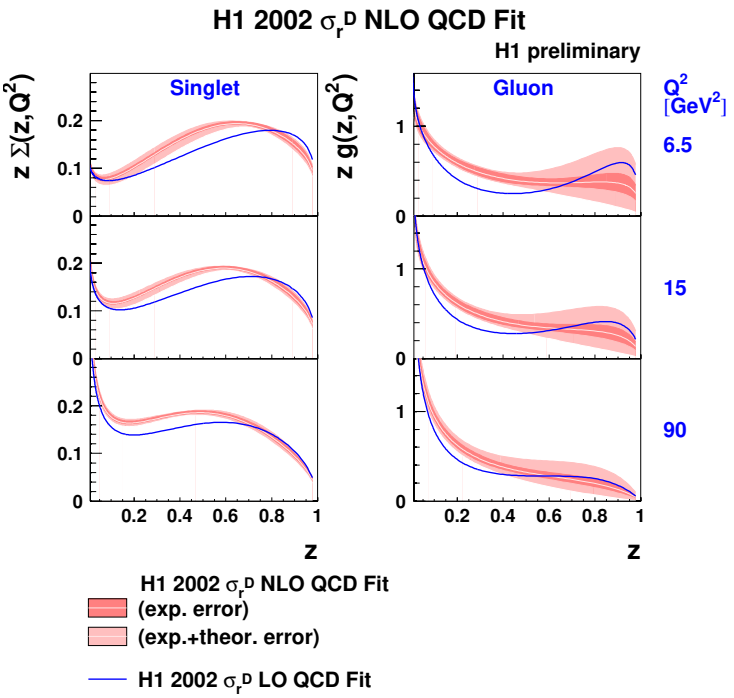

Fig. 2.3. Parton distributions of the pomeron at the LO and at the NLO as determined in DGLAP fits to H1 F_2^D data. They are shown as a function of the parton momentum fraction z at different scales Q^2. The left plots show the quark distributions, the right plots show the gluon (from [3]).

2.2 Diffractive dijet production

This section describes how predictions for diffractive dijet production are obtained with Monte Carlo event generators based on pomeron parton densities. Then the kinematics of diffractive dijet production are introduced and previous measurements are discussed.

2.2.1 QCD hard scattering factorisation

It has been proven within QCD [4] that the hard diffractive $\gamma^* p$ cross section can be written as a convolution of diffractive parton densities of the proton f_i^D with the hard parton-photon cross section $\hat{\sigma}^{\gamma^* i}$:

$$\frac{d^2\sigma(x, Q^2, x_{I\!P}, t)^{\gamma^* p \to Xp}}{dx_{I\!P}\, dt} = \sum_i \int_x^{x_{I\!P}} d\xi\, \hat{\sigma}^{\gamma^* i}(x, Q^2, \xi)\, f_i^D(\xi, Q^2, x_{I\!P}, t),$$

in which the sum runs over all quark and anti-quark flavours. This proof states that the hard subprocess is independent of the soft part of the interaction at the proton vertex. Based on QCD hard scattering factorisation it is possible to make predictions for hard diffractive final states (e.g., jets and heavy quarks) using diffractive PDFs determined in inclusive DDIS. It is noted that the proof does not include Regge factorisation. The latter is an additional assumption which is compatible with the inclusive F_2^D data at the present level of experimental precision. The diffractive quark and gluon densities can be used to predict production rates for hard diffractive final states, such as dijets or heavy quarks, for which the cross section for the hard subprocess is calculable in QCD. QCD factorisation serves as the basis for Monte Carlo event generator programs which are used to obtain predictions for diffractive dijet production.

2.3 Monte Carlo generators

Monte Carlo programs generate particle collision events according to a certain physics model. For a specific initial configuration of beam particles and their momenta, a large number of final state configurations are generated. The frequency with which a certain final state configuration occurs is given by its cross section. Different Monte Carlo programs are used in this analysis. They are introduced in the following.

2.3.1 RAPGAP implementation of the pomeron model

The RAPGAP 2.08 Monte Carlo program [5] is an implementation of the pomeron model. The program uses pomeron parton densities and the pomeron flux factor as described in Sec. 2.1.4. To obtain predictions for dijet production, leading order matrix elements for the hard QCD $2 \to 2$ subprocess are convoluted with parton distributions of the pomeron and the photon, taken at the scale $\mu = \sqrt{\hat{p}_T^2 + m_{q\bar{q}}^2}$, where $\hat{p}_T$ is the transverse momentum of the emerging hard partons and $m_{q\bar{q}}$ is the mass of the produced quarks.

Higher order effects are simulated using parton showers [6] in the leading $\log(\mu)$ approximation (MEPS), and the Lund string model [7] is used for hadronisation.

Reggeon contributions are simulated using the corresponding reggeon flux parameterisation from the pomeron PDF extraction and parton density functions of the pion [8].

RAPGAP for diffractive photoproduction

The following additional settings are used to generate dijet events in diffractive photoproduction. RAPGAP can also predict resolved photon processes (cf. Sec. 2.3.6.1) in which the proton structure is chosen to be given by the leading order GRV parton distribution functions [9] which were found to give a good description of the effective photon structure function as measured by H1 [10]. To avoid divergences in the calculation of the matrix elements, a cut $\hat{p}_T > 2$ GeV is applied at the generator level. No significant losses are seen for the selected jets with $E_T^{\text{jet1}} > 5$ GeV and $E_T^{\text{jet2}} > 4$ GeV due to this cut. RAPGAP does not include so-called additional multiple interactions between the photon remnant and the other hadronic systems (the outgoing proton system and the pomeron remnant).

RAPGAP for diffractive DIS

Processes with a resolved virtual photon are generated in which the structure of the photon is given by the SaS-2D parameterisation [11]. These PDFs have been found to give a reasonable description of inclusive DIS dijet production at low Q^2 [12]. Divergences in the $2 \to 2$ matrix elements for light quarks are avoided by a cut $\hat{p}_T > 3$ GeV. Photon radiation by the electron before or after the interaction is simulated using the program HERACLES [13].

2.3.2 Generator for inclusive dijet production

The PYTHIA 6.1 Monte Carlo program [14] is used to simulate inclusive dijet photoproduction processes in order to evaluate migrations from high M_Y and high $x_{I\!P}$. The predictions are based on the CTEQ5L leading order proton PDFs [15]. RAPGAP is also used to simulate inclusive DIS dijet production to determine migrations from high M_Y and high $x_{I\!P}$. For these processes, the GRV '94 NLL proton PDFs (DIS scheme) are used [16].

2.3.3 DIFFVM model for proton dissociation

The Monte Carlo generator DIFFVM [17] simulates diffractive vector meson production. Unlike the other generators mentioned here, DIFFVM is able to simulate proton dissociation. It is used to determine a correction factor for smearing across the cross section boundary $M_Y = 1.6$ GeV. This factor is not determined in the framework of the work presented here. Instead it is taken from a previous analysis which applied the same cuts in the outgoing proton direction.

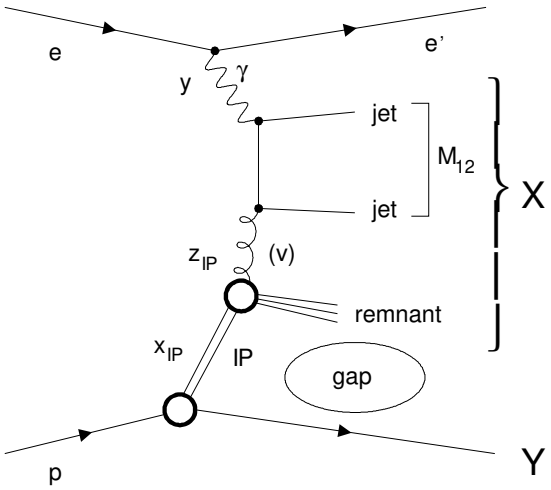

Fig. 2.4. Diffractive dijet BGF production in the pomeron model.

2.3.4 Diffractive dijet production in DIS

2.3.4.1 Kinematics of diffractive dijet production in DIS

It was shown in Sec. 2.1.4 that the gluon distribution is the dominating parton density of the pomeron. Measurements of inclusive DDIS are only sensitive to the electrically charged quarks. The gluon has to be inferred indirectly from the scaling violations of the structure function.

Diffractive dijet production in DIS occurs mainly through the process of boson gluon fusion depicted in Fig. 2.3.4.1. The photon undergoes a hard scatter with a gluon from the pomeron which forms to two outgoing partons. Diffractive dijet production is therefore directly sensitive to the gluon content in the pomeron. The variable $z_{I\!P}$ denotes the longitudinal fractional momentum carried by the parton from the pomeron. With v being the full momentum of the parton from the pomeron, $z_{I\!P}$ is given by

$$z_{I\!P} \equiv \frac{q \cdot v}{q \cdot (P - p_Y)} = \beta\,(1 + \hat{s}/Q^2).$$

The fractional proton momentum x_p entering the hard scatter is given by

$$x_p = x_{I\!P}\, z_{I\!P}, \tag{2.7}$$

with $x_{I\!P}$ defined according to (2.4). The fraction x_p is approximately fixed in this analysis by the requirement of two central jets.

The partons from the subprocess fragment into two hadron jets in the process of hadronisation. The jets with the largest and second highest p_T are called the leading and subleading jet, respectively.

To study the dynamics of QCD in dijet production, the photon-proton centre-of-mass system is the relevant system. In DIS, the electron is scattered with a significant transverse momentum and the photon-proton collision axis is different from the beam axis. In the DIS analysis, the jets are therefore identified in the $\gamma^* p$ system. The cross

section is measured as a function of the transverse energy $E_T^{*,\mathrm{jet1}}$ of the leading jet. The superscript '$*$' indicates that the transverse momentum is evaluated in the $\gamma^* p$ system. The jets are massless and the terms transverse energy and transverse momentum are used synonymously for jets throughout this document.

The directions of the particles are described by the azimuthal angle Φ and the polar angle θ. The latter is measured with respect to the positive z axis which is defined by the direction of the incoming proton momentum. Unlike Φ, θ is not invariant under Lorentz boosts along z. The rapidity y' is defined as

$$y' \equiv \frac{1}{2} \ln \frac{E + p_z}{E - p_z}.$$

Intervals in y' are invariant under boosts along z. The pseudorapidity η is defined as

$$\eta \equiv \frac{1}{2} \ln \frac{p + p_z}{p - p_z} = -\ln \left(\tan \frac{\theta}{2} \right) \tag{2.8}$$

and is a good approximation of y' in the limit of large energies, when $E \approx |\vec{p}| \equiv p$.

The difference between the pseudorapidities of the two leading jets

$$\left| \Delta \eta^*_{\mathrm{jet}} \right| \equiv |\eta^*_{\mathrm{jet1}} - \eta^*_{\mathrm{jet2}}| \tag{2.9}$$

is related to the scattering angle $\hat{\theta}$ in the centre-of-mass system of the hard subprocess:

$$\cos \hat{\theta} = \tanh \frac{\Delta \eta^*_{\mathrm{jet}}}{2}.$$

For the mean pseudorapidity

$$\langle \eta^{\mathrm{lab}}_{\mathrm{jet}} \rangle \equiv 0.5 \, (\eta^{\mathrm{lab}}_{\mathrm{jet1}} + \eta^{\mathrm{lab}}_{\mathrm{jet2}}), \tag{2.10}$$

the jets are boosted back into the laboratory frame.

The centre-of-mass energy of the hard scattering process is given by the invariant mass of the dijet system.

$$\sqrt{\hat{s}} = M_{12} = \sqrt{(u + v)^2}. \tag{2.11}$$

Processes with a resolved photon (cf. Sec. 2.3.6.1) are suppressed in DIS because of the large virtuality Q^2 of the photon. In the range $4 < Q^2 < 80$ GeV^2, for which the DIS analysis is performed the contribution from resolved photon processes is at the level of 7%.

2.3.4.2 Previous H1 results on diffractive dijet production in DIS

The latest published H1 result on diffractive dijet production in DIS [18] is based on data taken in 1996–97, corresponding to an integrated luminosity of 18 pb^{-1}. A large number of differential and double-differential cross sections were measured for $4 < Q^2 < 80$ GeV^2, $0.1 < y < 0.7$, $x_{I\!P} < 0.05$ (and $x_{I\!P} < 0.01$) and $p_T^{\mathrm{jet}} > 4$ GeV. The jets were identified using a cone algorithm. Fig. 2.5 shows the measured cross section as a function of $z_{I\!P}$. The data are compared to LO predictions based on the pomeron model with LO pomeron parton

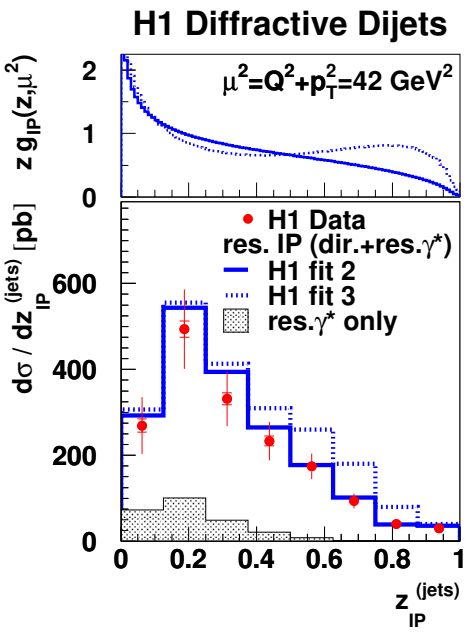

Fig. 2.5. Previous result on DDIS dijet production [18]. Shown at the bottom is the diffractive dijet cross section as a function of $z_{I\!P}$. Also shown are LO predictions based on LO pomeron parton densities in which the scale $\mu = \sqrt{Q^2 + p_T^2}$ is used as the renormalisation and factorisation scale. The contribution of resolved photon processes according to the prediction based on H1 fit 2 is shown as the hatched histogram. The corresponding gluon densities in the pomeron are shown at the top. They are evolved to the mean value of the scale and are normalised such that the pomeron flux factor $f_{I\!P/p}(x_{I\!P} = 0.003, t = 0)$ is unity.

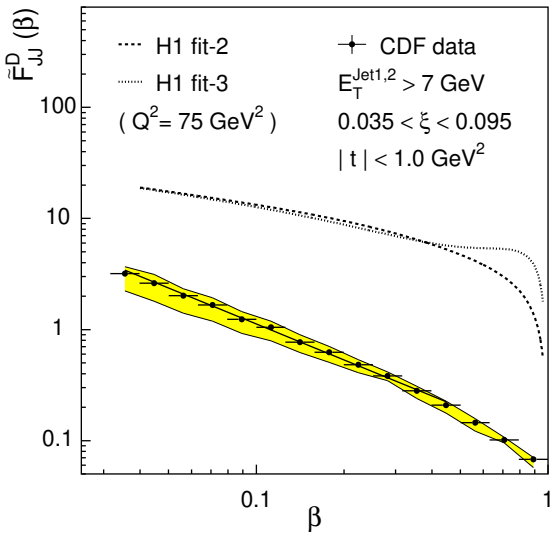

Fig. 2.6. The diffractive structure function of the antiproton as measured by the CDF Collaboration (from [20]). The lower (upper) boundary of the filled band represents the data distribution obtained using only the two leading jets (up to four jets of $E_T > 5$ GeV) in evaluating β. The additional systematic uncertainty of the data is ± 25 %. The straight line is a fit of the form β^{-n}. The expectations from the H1 fits 2 (3) are the dashed (dotted) lines.

densities extracted in inclusive DDIS. The conclusion was that, within the experimental uncertainties, the dijet data can be described both in normalisation and in shape by the RAPGAP model introduced in Sec. 2.3.1 based on the H1 fit 2 pomeron PDFs [19] and the corresponding flux factor. A small reggeon contribution is predicted according to the H1 fit 2 reggeon flux parameterisation and is needed to describe the data.

2.3.5 Diffractive dijet production at the Tevatron

At the Fermilab Tevatron $p\bar{p}$ collider, diffractive dijets with an elastically scattered antiproton have been studied at a centre-of-mass energy of 1800 GeV [20]. The diffractive structure function of the antiproton was measured and compared to predictions based on the pomeron parton densities determined in DDIS at HERA. The result is shown in Fig. 2.6. The prediction overestimates the measured structure function by approximately one order of magnitude. A similar discrepancy was observed in comparing diffractive W boson and dijet production rates at the Tevatron [21] with expectations based on ZEUS results [22] obtained from DDIS and diffractive dijet photoproduction at HERA.

A number of models have been suggested to account for the discrepancy observed between the measured distributions at the Tevatron and the predictions based on pomeron parton densities extracted at HERA in DDIS. They can be classified into two categories.

- **Survival probability models**
  These models describe diffractive scattering by the exchange of a universal colourless

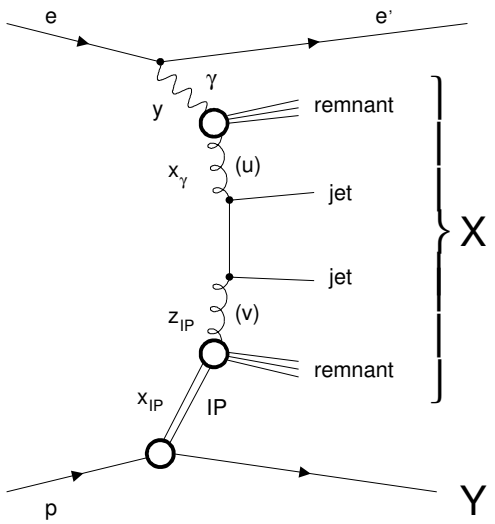

Fig. 2.7. Diffractive dijet resolved photon process in the pomeron model.

pomeron. Universal means that it has the same PDFs and the same intercept and flux factor in different diffractive interactions, such as ep, pp, $p\bar{p}$ and γp collisions. In these models, the discrepancy is due to secondary interactions in hadron-hadron collisions which destroy the diffractive signature of the event. An example of such a model is described in [23].

- **Soft colour neutralisation models**
  In these models, no pomeron is used to mediate diffractive scattering. Instead, the diffractive interaction is similar to the non-diffractive case in which colour is exchanged. Diffraction occurs through colour reconfigurations between the final state partons. This mechanism is called soft because it does not change the momenta of the partons. The reconfiguration can lead to the formation of colour singlet states which can be separated by a large rapidity gap. An example of such a model is the soft colour interaction model SCI [24].

Both types of models have free parameters which are tuned to describe the diffractive production rates measured at the Tevatron. They must also be able to predict the cross section in diffractive dijet photoproduction.

2.3.6 Diffractive dijet photoproduction

2.3.6.1 Resolved photon processes

Due to the Heisenberg uncertainty principle, for some time Δt a photon can fluctuate into a $q\bar{q}$ pair. The time Δt is related to the inverse of the virtuality Q^2 of the photon. In photoproduction, the exchanged photon is quasi-real with an invariant mass close to zero: $Q^2 \approx 0$. The fraction of resolved photon processes is large in photoproduction. Fig. 2.3.6.1 shows a resolved photon process. The photon fluctuates into a hadronic system from which one parton undergoes the hard scatter with the parton from the proton. The variable x_γ

denotes the longitudinal photon momentum fraction entering the hard scatter. For direct photon processes $x_\gamma = 1$, whereas for resolved photon processes $x_\gamma < 1$. With u denoting the momentum of the parton from the photon, x_γ is defined as

$$x_\gamma \equiv \frac{P \cdot u}{P \cdot q}.$$

For resolved photon processes, the structure of the photon is described by parton density functions.

2.3.6.2 Kinematics of diffractive dijets in photoproduction

In the photoproduction kinematic region analysed in this work, the electron is almost not deflected from its original direction ($\theta_e \approx 180^\text{o}$). This implies that the photon-proton system is simply Lorentz-boosted along z. For simplicity, all variables in the photoproduction analysis will therefore be given in the laboratory frame.

In photoproduction, the inelasticity y corresponds to the fractional photon energy

$$y = E_\gamma / E_e = 1 - \frac{E'_e}{E_e}, \tag{2.12}$$

in which E'_e is the energy of the scattered electron and E_e is the initial electron beam energy. The photon-proton centre-of-mass energy W is given by

$$W = \sqrt{y\, s}. \tag{2.13}$$

The invariant mass of the hadronic system X is calculated according to

$$M_X = \sqrt{x_{I\!P}\, y\, s}.$$

The average pseudorapidity and the difference of the pseudorapidities of the leading and the subleading jet are defined in the laboratory frame as

$$\langle \eta^\text{lab}_\text{jet} \rangle \equiv \frac{1}{2}\left(\eta^\text{lab}_\text{jet1} + \eta^\text{lab}_\text{jet2}\right); \qquad |\Delta\eta_\text{jet}| \equiv |\eta^\text{lab}_\text{jet1} - \eta^\text{lab}_\text{jet2}|. \tag{2.14}$$

2.3.6.3 Previous H1 results on diffractive dijet photoproduction

The latest published H1 result on diffractive dijet photoproduction [25] is based on data taken in 1995, corresponding to an integrated luminosity of 2.2 pb^{-1}. The kinematic range of the measurement was $Q^2 < 0.01$ GeV^2, $0.25 < y < 0.7$, $x_{I\!P} < 0.05$, $-1 < \eta^\text{lab}_\text{jet1,2} < 2$. Exactly two jets were required with $p_T^\text{jet} > 5$ GeV. The jets were identified using a cone algorithm. Differential cross sections as a function of η_jet, p_T^jet, x_γ^had and $z_{I\!P}^\text{jets}$ were measured. Fig. 2.8 shows the measured cross section as a function of x_γ. The distribution corresponds to one entry per jet. This is in contrast to the present analysis, where the distributions correspond to one entry per dijet event. The data are compared to LO predictions based on the pomeron model with LO pomeron parton densities extracted in inclusive DDIS. The POMPYT generator program [26] was used for the predictions. The dijet distributions are described both in normalisation and in shape by the POMPYT model based on the H1

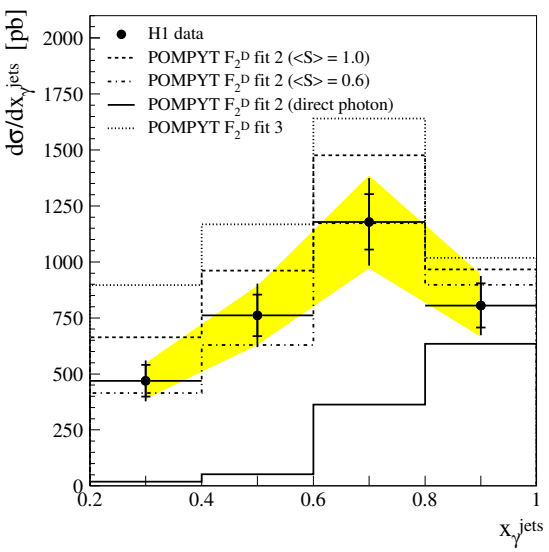

Fig. 2.8. Previous result on diffractive dijet photoproduction [25]. Shown is the diffractive dijet cross section as a function of x_γ with one entry per jet. The shaded band shows the overall normalisation uncertainty. Also shown are LO predictions based on LO pomeron parton densities in which the scale $\mu = p_T$ is used as the renormalisation and factorisation scale. The dash-dotted curve shows the prediction based on the H1 fit 2 densities with a gap survival probability of 0.6 applied to events with $x_\gamma < 0.6$. The contribution of direct photon processes according to the prediction based on H1 fit 2 is also indicated.

fit 2 pomeron PDFs and the corresponding flux factor. The best description of the data is obtained when a survival probability factor of 0.6 is applied to events with $x_\gamma < 0.6$. However, a factor of unity could not be excluded due to the uncertainties of the data distributions.

2.3.7 Motivation for the present analyses

The first measurement done in this thesis work was the analysis of diffractive dijet photoproduction. The aim was to improve the precision of the previous measurement and to see whether the diffractive parton densities which are able to describe the DIS dijets can also describe diffractive dijet photoproduction. The additional hadronic system into which the photon can fluctuate makes photoproduction at HERA similar to hadron-hadron collisions. If secondary interactions due to the additional hadronic system would be the reason for the suppression in diffractive $p\bar{p}$ collisions then this mechanism should also be visible in diffractive photoproduction.

Unlike the previous H1 analyses on diffractive jet production, the γp analysis presented here applies asymmetric cuts on the transverse energies of the jets to allow comparisons with NLO predictions which will be available in the near future. Pomeron parton densities at the NLO have been extracted and to obtain predictions for dijet production is now a matter of incorporating these densities and the pomeron flux into existing NLO programs for dijet photoproduction. In addition, the photoproduction analysis presented here employs the inclusive k_T cluster jet algorithm instead of the cone algorithm which was used for the old analyses.

To be able to compare the results in photoproduction and DIS as directly as possible, the analysis was repeated in the DIS kinematic region with the same jet algorithm, the same kinematic cuts, and the same data sets.

Chapter 3

The HERA collider and the H1 detector

At the DESY facility[1] in Hamburg, Germany, the unique lepton hadron collider HERA[2] is located. Since the end of 1991, electrons (or positrons[3]) are scattered off protons at a centre-of-mass energy of ≈ 300 GeV. The present analysis is concerned with data obtained in 1996 and 1997 by the H1 experiment, one of the large scale detectors grouped around HERA. This chapter briefly introduces the collider and gives a description of the H1 detector and the components which are most important for this analysis. The HERA collider has been subject to various upgrades. The machine parameters quoted here are the ones that were relevant in the period 1996–97.

3.1 The HERA collider

Fig. 3.1a shows a diagrammatic view of the HERA collider. Electrons and protons are stored in two separate accelerators, HERA-e and HERA-p, respectively, with circumferences of 6.4 km. The particles are not continuously distributed along the ring but grouped in 180 bunches. These packets are accelerated by electromagnetic fields of high frequency mostly on the straight line sections. In the curves, conventional dipole magnets with field strengths of 0.17 T bend the electron beam, whereas for the proton beam superconducting magnets with a strength of up to 4.5 T are used.

After electron energies of 27.5 GeV and proton energies of 820 GeV have been reached, the beams are brought to collision in two interaction zones in the experiment halls North and South at a centre-of-mass energy of 300 GeV. The time between electron and proton bunch crossings is 96 ns corresponding to a frequency of 10^7 Hz.

1. Deutsches Elektronen-Synchrotron.
2. Hadron-Elektron-Ring-Anlage.
3. Throughout this thesis, the word 'electron' will be used as a synonym for both electrons and positrons.

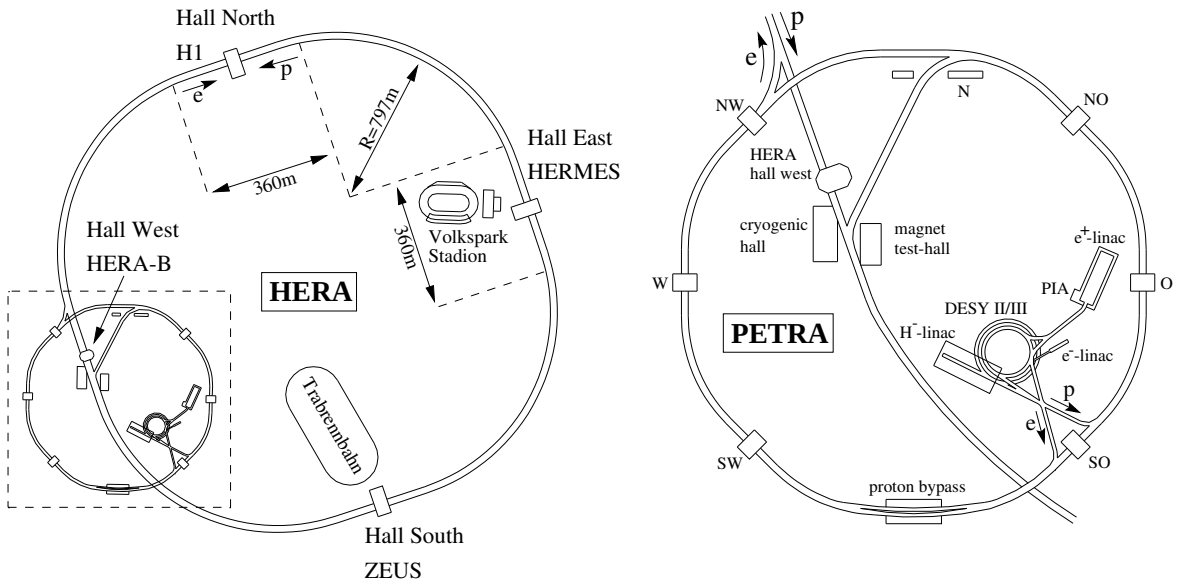

(a) (b)

Fig. 3.1. The HERA collider (a) and its pre-accelerators (b).

Pre-Acceleration

Before being filled into HERA, the particles undergo several pre-acceleration steps (Fig. 3.1b). Electrons emerging from a LINAC[4] at energies of 450 MeV are accelerated up to 7.5 GeV in DESY II and then stored in PETRA II. After 60 electron bunches have been accumulated, they are accelerated to 12 GeV and injected into HERA-e. To produce free protons, negatively charged hydrogen ions of 50 MeV energy are shot onto a thin foil, which strips off the electrons. The remaining protons are accelerated to 7.5 GeV in DESY III and to 40 GeV in PETRA II before being injected into HERA-p.

Luminosity

The interaction rate is determined by the luminosity $\mathscr{L}$. It is determined by the beam parameters according to

$$\mathscr{L} = \frac{\nu \; n_b \; n_e \; n_p}{A} \approx 10^{31} \; \mathrm{cm}^{-2}\,\mathrm{s}^{-1} = 10 \; \mu\mathrm{b}^{-1}\,\mathrm{s}^{-1}, \tag{3.1}$$

with

- ν revolution frequency ($5 \cdot 10^5$ Hz)
- n_b number of bunches (180)
- n_e number of electrons per bunch (10^{10}–10^{11})
- n_p number of protons per bunch (10^{10}–10^{11})

4. Linear Accelerator.

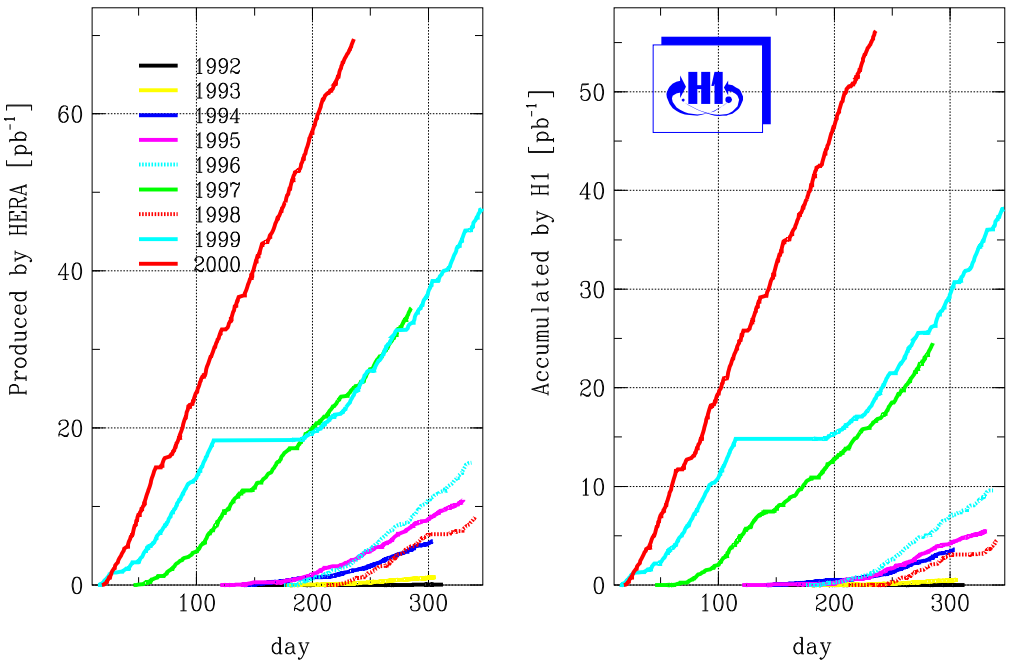

Fig. 3.2. HERA (a) and H1 (b) integrated luminosities shown separately for every year of operation.

A transverse extension of the interaction region (0.17 mm^2)

The values correspond to the operation in the year 1996.

The number of events collected at a collider is proportional to the timely integrated luminosity L:

$$L = \int \mathscr{L}(t)\, dt. \tag{3.2}$$

Fig. 3.2a displays the integrated luminosity delivered by HERA for each of its years of service. The integrated luminosity actually recorded by the H1 experiment is shown in Fig. 3.2b. The continuous gain of knowledge about the HERA machine made it possible to achieve a better performance every year. By the end of 2000, H1 had taken more than 100 pb^{-1} of data.

HERA physics programme

The main aspects of particle physics research done at HERA are tests of the standard model and the search for physics beyond it. Among the physics topics that are addressed with the multipurpose detectors H1 and ZEUS are

- precision measurements of the proton structure functions,
- search for substructures of quarks and leptons,

- heavy flavour production mechanisms,
- the structure of the photon,
- diffractive phenomena,
- searches for new physics beyond the standard model,
- measurements of α_s.

In the hall East, the HERMES experiment uses the electron beam to measure the spin structure functions of the proton and neutron. The HERA-B experiment that studied CP violation in B meson decays stopped data taking in 2003. It used the proton beam on a fixed target. More information on HERA can be obtained from [27].

3.2 The H1 detector

3.2.1 Overview

A diagram of the central H1 detector is shown in Fig. 3.3. The detector has a mass of 2800 t and a size of 12×10×15 m^3. The interaction point is located near the origin of the H1 coordinate system (small mark near 2). Electrons are entering from the left and protons come from the right, The positive z axis is defined by the direction of the incoming proton beam momentum. This direction is called the 'forward' direction. The coordinate x points to the centre of the accelerator ring, and y is pointing upwards. The polar scattering angle θ is measured with respect to the forward direction.

The general structure of the H1 detector follows the conventional design established for high energy particle physics experiments. The interaction region is surrounded by a tracking system which measures the transverse momenta of charged particles in a magnetic field. The calorimeter is built around the tracking detector and measures energy depositions. Particles that are not stopped in the inner parts of the detector (mostly muons) are detected in the so-called central muon system. Because of the different beam energies of protons and electrons, the final state is not distributed symmetrically with respect to the interaction point. Instead it is boosted in the forward direction. The detector has a finer granularity in the forward region to obtain a better spatial resolution in that area. A complete description of the detector can be found in [28]. Here, only the components most relevant for the analysis are introduced.

3.2.2 Tracking detectors

A superconducting coil 6 produces a solenoidal magnetic field of strength 1.16 T parallel to the beam axis. Charged particles travelling in the perpendicular $x - y$ plane are subjected to the Lorentz force. The central tracking system (2, and Fig. 3.4) measures the particle trajectories. The transverse momentum and the electrical charge can be determined from the curvature of the trajectory. The tracking system is divided into a forward, a central, and a backward part. Only the central and backward tracking detectors are used in this analysis.

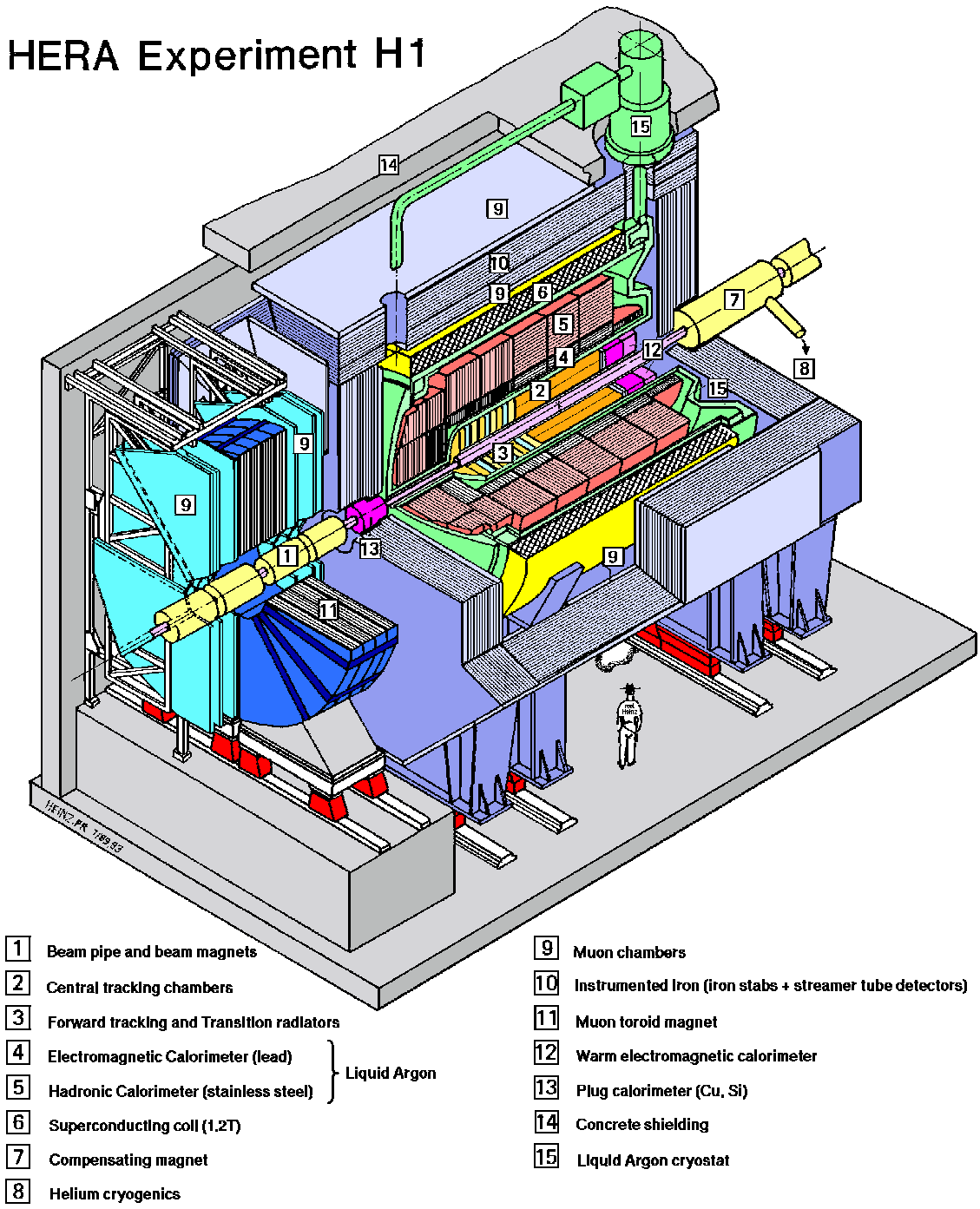

Fig. 3.3. The central H1 detector.

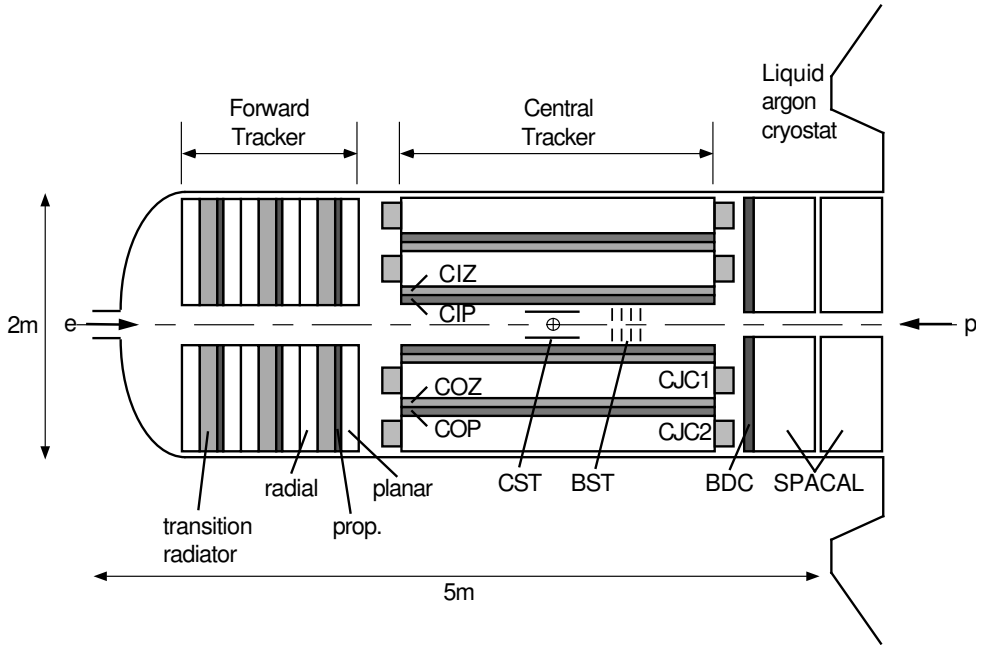

Fig. 3.4. The tracking system of the H1 detector.

A radial view of the central tracking detector is displayed in Fig. 3.5. The beam pipe is surrounded by two concentric drift chambers (CJC1 and CJC2) with a length of 2.2 m. Wires are strung parallel to the beam axis and allow a resolution in (r, Φ) of 170 μm. The position in z is measured by charge division with a resolution of ± 2.2 cm. The z resolution is improved by two additional drift chambers (CIZ and COZ) in which the wires are perpendicular to the beam axis. The obtained z resolution is 260 μm. The combined momentum resolution of all drift chambers is $\sigma(p)/p < 0.01\, p/\text{GeV}$.

A fast tracking signal which is used for the first level trigger is obtained with additional multi-wire proportional chambers (MWPC). The central inner chamber (CIP) is located inside of the CIZ, and the outer chamber resides between the COZ and the CJC2. The signal is delivered with a resolution of 21 ns. This time is much smaller than the time between bunch crossings (96 ns).

In the DIS analysis presented in this thesis, the backward drift chamber (BDC) is used to supplement the electron identification in the SPACAL calorimeter (Fig. 3.4).

3.2.3 Liquid argon calorimeter (LAr)

In the H1 experiment, the main calorimeter is a sandwich type calorimeter. It is composed of absorber plates and liquid argon as the active detection material. The argon is ionised by shower particles created in the absorber plates by the incident particle. The number of created ion-electron pairs is proportional to the energy of the incident particle. The electrons are collected on electrodes and a signal proportional to the electrical charge is read out. Because the ionisation process is of statistical nature, the absolute energy resolution is proportional to $\sqrt{E}$.

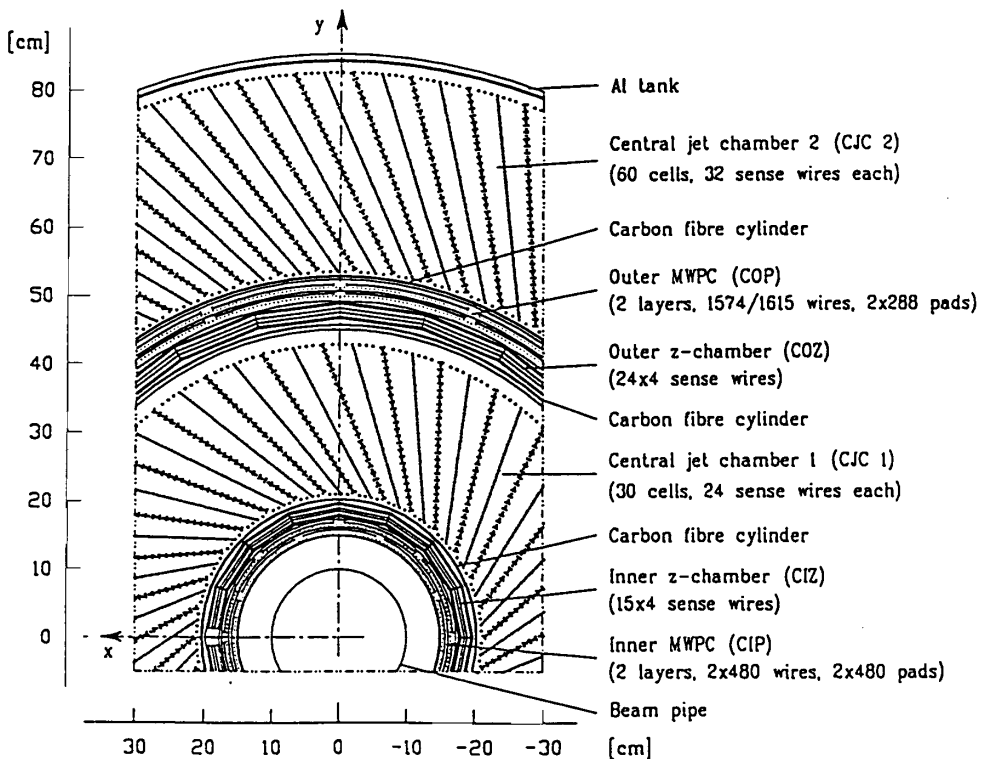

Fig. 3.5. A radial view of the central tracking system consisting of the central drift chambers CJC1 and CJC2, the z chambers CIZ and COZ and the proportional chambers CIP and COP.

The LAr consists of an inner, electromagnetic part [4] with lead absorber plates corresponding to 20–30 radiation lengths with a relative energy resolution $\sigma_E/E = 11\%/\sqrt{E/\mathrm{GeV}}$ and an outer hadronic part [5] with stainless steel plates amounting to 4.5–7 interaction lengths with a relative resolution of $50\%/\sqrt{E/\mathrm{GeV}}$. The energy calibration has an uncertainty of 5%, which has to be added for both parts. The LAr covers the range $3.6 > \eta > -1.4$. The absolute hadronic energy scale is known within 4%.

3.2.4 Backward calorimeter SPACAL

The lead/scintillating fibre calorimeter SPACAL ('spaghetti calorimeter') [12] covers the backward range -1.42 $> \eta >$ −3.82. Incident particles develop a shower in the lead which causes the fibres to scintillate. The light is detect in photomultiplier tubes. The calorimeter consists of an electromagnetic part with a depth of 28 radiation lengths and an hadronic part corresponding to 2 interaction lengths. The energy resolution in the electromagnetic part is $7\%/\sqrt{E/\mathrm{GeV}}$ ([29]). An additional systematic uncertainty of 1% has to be added due to the electronics used to amplify the signals. The absolute electromagnetic energy scale is known to 0.3% for electron energies of 27.5 GeV and 2.0% for electron energies of 8 GeV [30]. The absolute energy scale in the hadronic part of the SPACAL is known to 7%.

3.2.5 Forward detectors

The forward region is covered by the forward muon detector FMD and the proton remnant tagger PRT. The FMD consists of 6 double layers of drift chambers, four with wires perpendicular to the beam axis to measure θ and two with wires along the beam axis to measure Φ. A charged particle produces a hit pair in a double layer. The FMD is placed outside of the massive iron yoke, having the main purpose of identifying muons from a collision event. However, it can also be reached by particles scattered by collimators around the beam pipe. The detector consists of six drift chambers [9], 3 of them being located behind a toroidal magnet [11]. The acceptance region is $2.9 > \eta > 1.4$ with a relative energy resolution of 24–36 %.

The PRT is located at $z = 26$ m in the HERA tunnel. It consists of seven scintillator layers which are shielded with lead. The detector can measure activity in the region $7 > \eta > 5.1$.

3.2.6 Electron and photon detectors

In the photoproduction analysis, the electron is measured in a dedicated electron detector which is located at $z = -33$ m. It has an acceptance for electrons scattered by less than 5 mrad. It is a Čerenkov calorimeter and can measure energies between 5.5 GeV and 22 GeV. The position of the detector is indicated in Fig. 3.6.

Together with the electron detector, the photon detector at $z = -103$ m forms the luminosity system (Fig. 3.6). The photon detector is a Čerenkov calorimeter with photomultiplier read-out and is used to detect photons from Bethe-Heitler processes as depicted in Fig. 3.7.

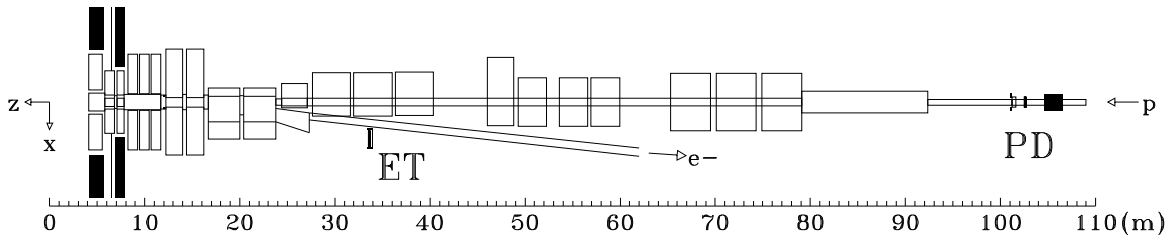

Fig. 3.6. The H1 luminosity system. The small angle electron detector (ET) is located upstream at $z = -33$ m. The photon detector (PD) is placed at $z = -103$ m

Data aquisition and trigger system

The probability for an interaction per bunch crossing is of the order of 10^{-3} [28]. Therefore, the rate of 10^7 bunch crossings per second translates into a collision frequency of 10^4 Hz, dominated by background processes. Physically relevant events are selected by a hardware trigger system. Signal patterns from various detector components are analysed to obtain a decision.

The trigger system is divided into five levels L1–L5. Based on triggers, L1 decides within 2 μs whether an event is rejected or kept. L1 is fully pipelined and therefore dead-time free. If at least one trigger is activated, the event is passed on to L2 for further examination. Typically, the L1 *keep signal* is sent at a rate of 50 Hz. For L2 the pipelines storing the full event information have to be stopped and read out. Based on correlations between the triggers, L2 gives a decision within 20 μs. If the event is not accepted by L2, the read-out is immediately stopped and data taking is continued, otherwise the event is fully read out. In the latter case, the total dead time is 1.5 ms. The event is directed to L4 (L3 is not yet operating), consisting of a parallel processor farm which operates a reduced version of the full reconstruction code. If it can verify the L1 and L2 keep signals, L4 stores the data on tape. The event is fully reconstructed offline by L5.

Luminosity measurement

The luminosity $\mathscr{L}$ is the ratio of the event rate dN/dt and the cross section σ:

$$\frac{dN_i}{dt} = \mathscr{L}\ \sigma_i, \tag{3.3}$$

it is independent of the process i. Integrated over the time t, this relation reads

$$N_i = L\ \sigma_i, \tag{3.4}$$

in which L is the integrated luminosity.

To measure a cross section, the number of events N_i fullfilling certain conditions ('cuts') is determined. The luminosity $\mathscr{L}$ is determined with the luminosity system which measures the rate of Bethe Heitler interactions $ep \to ep\gamma$ (Bremsstrahlung) for which the cross section is calculable in QED with high precision. The luminosity is measured in parallel with the data taking because $\mathscr{L}$ depends on the beam conditions.

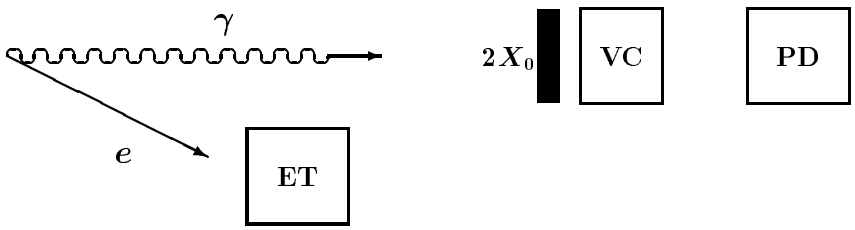

Fig. 3.7. Bethe Heitler Bremsstrahlung process as seen by the H1 luminosity system. The electron and photon are detected in the small angle electron detector ET and the photon detector PD, respectively. The PD is shielded from synchrotron radiation by a lead filter of two radiation lengths and a water Čerenkov counter.

Chapter 4

Correction of detector effects

One of the key ingredients of the analyses presented here is the correction of the smearing introduced by the finite detector resolution and acceptance. Due to the complicated experimental setup that is used in the detection of high energy particle physics collisions, the correction procedure is complex.

4.1 Partons, hadrons and detector response

A picture of our current understanding of the processes involved in high energy *ep* scattering (and its detection) is shown in Fig. 4.1. Different stages can be identified. First, final state partons are produced with certain 4-momenta. The kinematics and event quantities at the parton level are calculable within quantum field theory (supplemented by PDFs, which have to be extracted from measurements). Partons carry the colour quantum number. Colourless hadrons are formed in the process of fragmentation (also called hadronisation). Phenomenological models exist which describe this process. They have been tuned to describe existing measurements. The hadrons are measured in the detector. The finite resolution and geometrical acceptance of the apparatus will affect the measurement.

4.2 Event variable spectra and migrations

Due to the statistical properties of quantum physics, the cross sections have to be extracted by statistical means. The measurement involves a large number of particle collisions which all result from the same initial conditions. For every event variable, a *spectrum* is therefore obtained from the various events. A *bin* is an interval in such a spectrum.

The values of a variable reconstructed at the detector level and at the hadron level are in general different because of the finite detector resolution and acceptance. If the

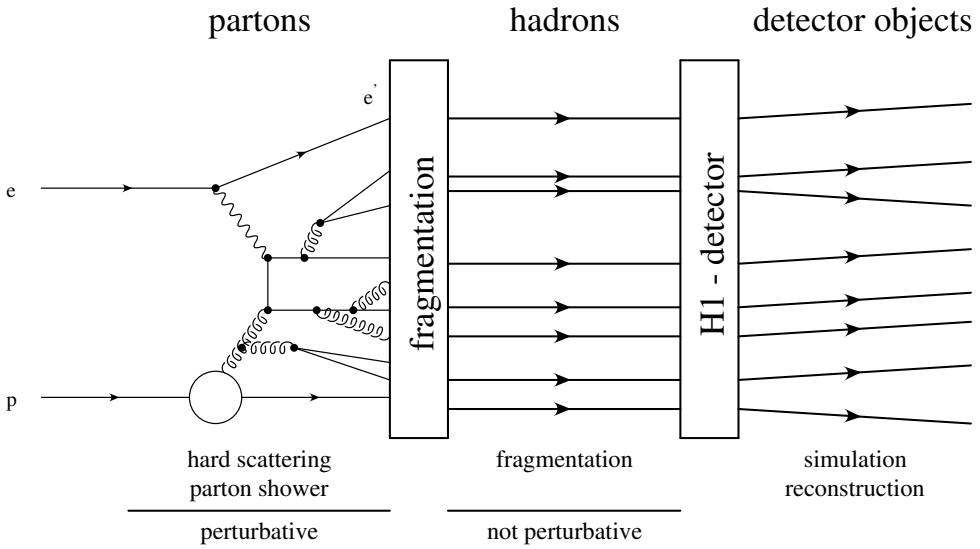

Fig. 4.1. The picture of an *ep* collision and its detection as we currently understand it (from [31]). The time evolves along the horizontal axis.

difference is large the variable can be in one bin of the hadron level spectrum and in another bin at the detector level. This phenomenon is referred to as *migrations*. Migrations can be studied using Monte Carlo events for which the detector response has been simulated (cf. Sec. 4.3). Fig. 4.2 shows a typical situation. Shown at the top is the detector level spectrum of some variable x. This variable is used to define the phase space of the measurement by a cut indicated by the dashed line. The same cut is applied at both the hadron and the detector level. The filled (hatched) area indicates the events which are inside (outside) the phase space region at the hadron level. Some of the events which are inside the hadron level region are lost because of migrations (represented by the filled area to the right of the cut line). There are also events which migrate into the detector sample from outside the hadron level region (the hatched area to the left of the cut line). For a given detector resolution, the amount of migrations depends on the shape of the spectrum. For a flat spectrum, the migrations inside and out of a bin balance each other. For a falling spectrum, the effect will be a net smearing into the bin.

4.3 Simulation of the H1 detector response

The correction for detector smearing is determined using generated Monte Carlo events for which the full detector response has been simulated. A Monte Carlo generator event output consists of a list of particles with certain quantum numbers and their momentum 4-vectors. To obtain the detector response to the event, the interactions of the particles with the detector material must be evaluated. For the H1 detector, the program `H1SIM` [32] based on the `GEANT` package [33] performs these calculations. Each particle is treated individually in its passage through the detector. The probability for a particle to interact with the detector material is evaluated using tabulated cross sections. These interactions

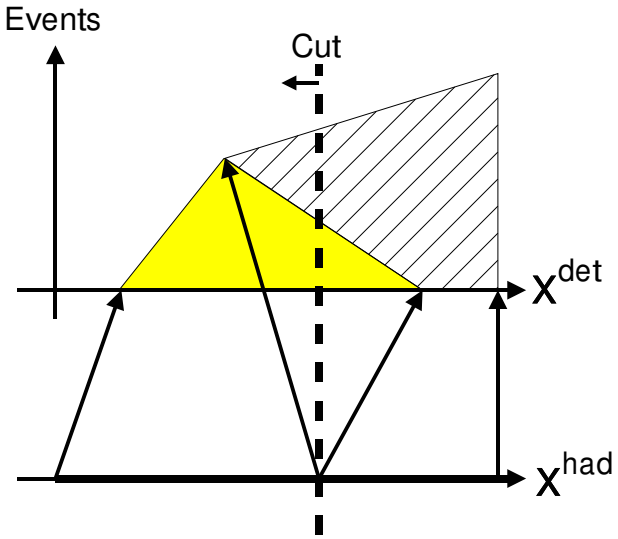

Fig. 4.2. Schematic representation of migrations between hadron and detector level spectra. The events inside the hadron level phase space are indicated by the filled area. The hatched area symbolises the events which are outside the hadron level phase space.

may result in secondary particles, which themselves must be traced. Finally, the detector response is obtained in the form of simulated electronic signals. These signals are then subjected to the same analysis chain as the signals obtained from real particle collisions.

4.4 Bin-to-bin correction method

A detector level spectrum can be corrected statistically by applying a correction factor for every bin of the spectrum. The correction factor is determined with Monte Carlo events for which also the detector response is simulated (cf. Sec. 4.3). From these events, spectra at the hadron and the detector level can be obtained. The correction factor is given by the ratio of these spectra.

The correction factor is sensitive to migrations between the bins of the hadron and detector level spectra and depends on the shape of the spectra. The factor will give a correct treatment of the migrations if the shapes of the data and MC spectra are equal.

4.5 Reweighting of the correction Monte Carlo

For the following it is assumed that the detector simulation models all aspects of the detection process. This assumption ensures that the hadron level spectra of the data and the MC are the same if their detector level spectra are equal.

An *out-of-the-box* Monte Carlo can almost always be improved in its description of the detector level data distributions. This is achieved by applying a factor to every Monte Carlo event (reweighting). It is noted in this respect that the model is changed only for the purpose of correcting the data. For the final comparison of the corrected cross

sections with specific model predictions the model is of course not altered in any way. The reweighting has to be applied to both the detector and the hadron level spectra. However, part of the hadron spectrum cannot be seen at the detector level because the detection efficiency is not 100% and events are lost. Care has to be taken that the reweighting in this regime is physical. The original MC distribution is generated according to the physics model implemented in the generator program and is safe in that respect.

4.6 Systematic uncertainties of the correction factor

A data distribution has statistical uncertainties and the description by the MC will never be perfect. This results in an uncertainty of the correction factor. To evaluate this uncertainty, the Monte Carlo spectrum is varied (by reweighting) within the uncertainties of the data such that the description is still acceptable. Then the correction factors are determined for the reweighted Monte Carlo. The difference between the central correction factor which gives the best description of the data distribution and the other factors is the systematic uncertainty of the correction factor which contributes to the systematic error of the cross section measurement.

4.7 Irrelevant detector level phase space

From the comparison at the detector level, a conclusion about the hadron level similarity can only be drawn in a phase space region where a connection exists between the two levels. At the phase space boundaries, this connection is given by migrations. The regions of the detector level phase space into which no events migrate are irrelevant for the correction process.

In the analyses presented here, a discrepancy is observed between the data distribution of $\log x_{I\!P}$ and the description by the MC at large values of $x_{I\!P}$. However, this region is irrelevant for the measurement because there are no migrations into this region from the cross section phase space at small values of $x_{I\!P}$.

4.8 Energy flow in the event

After the model has been reweighted to the same kinematics as the data the flow of stable hadrons produced in the event has to be studied. These particles are measured in the detector as tracks and energy in calorimeter cells. The multiplicity, energy, and spatial distribution of the tracks and cells must be described by the model. If this is the case the model can be used for the correction.

Chapter 5

Analysis of dijets in diffractive photoproduction

This chapter describes the measurement of dijet cross sections in diffractive photoproduction. The analysis is organised as follows. First, a sample of inclusive dijet events in photoproduction is selected. The data are modelled by a combination of non-diffractive and diffractive photoproduction Monte Carlo events. Non-diffractive events which have migrated into the selected region of the phase space due to the finite detector resolution and acceptance are statistically subtracted. The inclusive dijet sample is used to study the diffractive cut variables. It is shown that the diffractive dijet distributions are well described by the Monte Carlo model. A correction factor is calculated from the Monte Carlo to correct the distributions of the data for detector smearing. Systematic uncertainties involved in the extraction of the cross section are discussed. The results are presented and discussed in Chap. 7.

The analysis is performed separately for the years 96 and 97. With this approach, the differences in the detector setup are taken into account properly. The obtained cross sections can be compared as a consistency check. The corrected event numbers of 96 and 97 are then combined to give the cross section for the sum of both years. Control plots will be shown for one year only, except for the distributions of the especially important diffractive cut variables which are shown for both years.

5.1 Reconstruction of kinematic variables

This section discusses the reconstruction of the kinematic variables at the detector and the hadron level. The correlations between the quantities as defined at the different levels (parton, hadron, and detector) are examined with the diffractive Monte Carlo model which is introduced in Sec. 5.2 below. Fig. 5.1 shows the correlations between the kinematic

variables as reconstructed at the hadron level (horizontal axis) and the detector level (vertical axis). The difference between the hadron and the detector level variable is shown in Fig. 5.2. This difference is effectively the projection along the diagonals indicated in Fig. 5.1. Fig. 5.3 shows the correlations between the variables at the parton level (horizontal axis) and those reconstructed at the hadron level (vertical axis). The difference between the parton and the hadron level variables is shown in Fig. 5.4.

The energy E'_e of the scattered electron is measured in the electron detector and is used to reconstruct the inelasticity variable y at the detector level according to (2.12) The variable at the hadron level is reconstructed according to

$$y^{\mathrm{had}} = \frac{\sum_{\mathrm{X}} E - p_z}{2\,E_{\mathrm{e}}}.$$

The difference between y_{etag} and y^{had} is described by a Gaussian distribution that is centred around zero with a width (resolution) of $\sigma = 0.02$ (Fig. 5.2a). The value of y^{had} is very close to the value of y at the parton level as can be seen in Fig. 5.4a. The difference is of the order of 10^{-4}.

The photon-proton centre-of-mass energy W is reconstructed according to (2.13) The generated true parton level W is used at the hadron level. The resolution at the detector level is 4.5 GeV (Fig. 5.5a).

The hadronic system X, containing the jets, is measured in the LAr and SPACAL calorimeters and the central tracking system. Calorimeter cluster energies and track momenta are combined as explained in Sec. 5.3.7 below. The invariant mass M_X of the hadronic system is reconstructed at the detector level according to

$$M_X = \sqrt{\frac{M_{12}^2}{z_{I\!P}^{\mathrm{jets}}\; x_\gamma^{\mathrm{jets}}}}. \tag{5.1}$$

At the hadron level, M_X is given by

$$M_X^{\mathrm{had}} = \sqrt{p_X^2},$$

in which p_X is the 4-vector of the hadron system X. The systems X and Y are defined at the hadron level as explained in Sec. 2.1.1. The M_X resolution at the detector level is 2 GeV with respect to the hadron level in the range $10 < M_X < 40$ GeV. (Fig. 5.2g). No diffractive cuts are applied in Fig. 5.1g to extend the range to larger masses. It can be seen that the reconstructed value is too small for $M_X > 35$ GeV because the hadronic system is no longer fully contained within the LAr calorimeter for these large masses. This affects mainly the migrations observed in reggeon exchange processes. The reconstruction was not improved because the contribution of reggeon exchange is small. At the parton level, M_X is given by (2.1.1). The hadron level M_X is very well correlated with this value. The difference is of the order of 10^{-4} GeV (Fig. 5.4g).

The fractional proton momentum $x_{I\!P}$ transferred to the system X is reconstructed according to

$$x_{I\!P} = \frac{\sum_X (E + p_z)}{2\,E_p}, \tag{5.2}$$

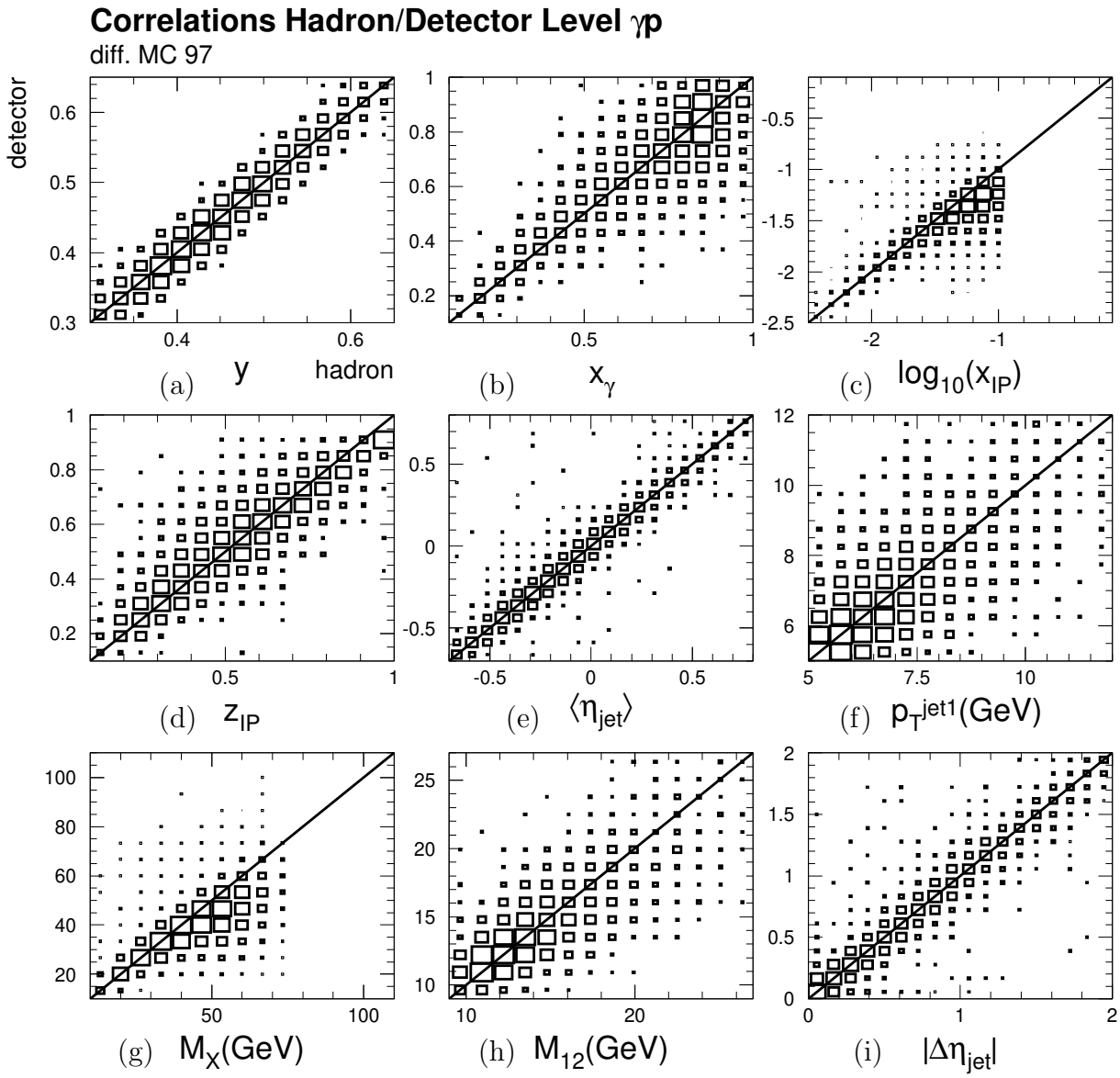

Fig. 5.1. Correlations between the variable reconstructed at the hadron level (horizontal axis) and the detector level (vertical axis). The correlations are evaluated with the diffractive MC for 97. All final selection cuts are applied at the detector level and the hadron level except for the distributions of $\log x_{I\!P}$ and M_X for which no diffractive cuts are applied to extend the populated range.

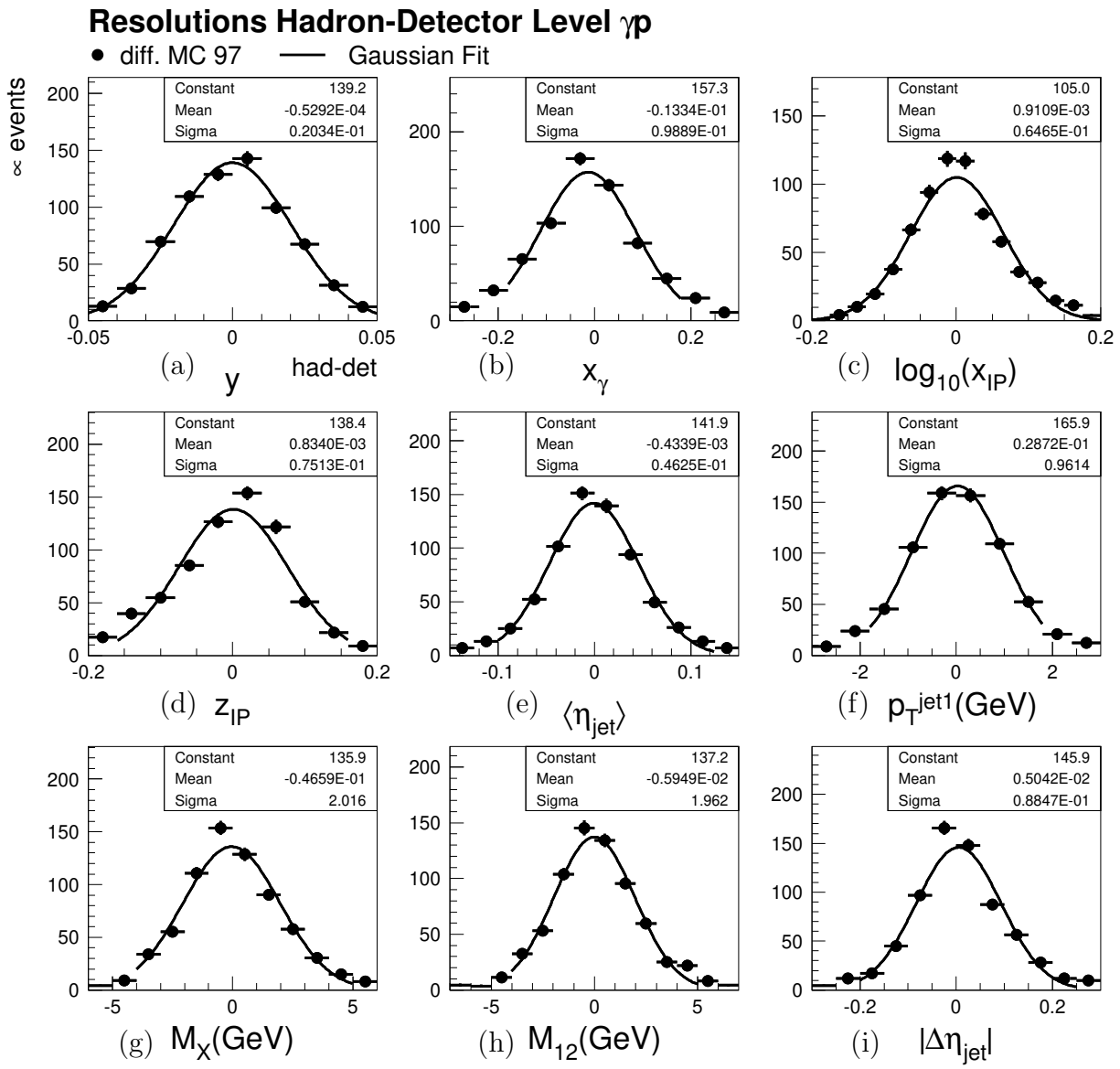

Fig. 5.2. Resolutions for reconstructing the hadron level quantity at the detector level. Shown is the difference between the variable reconstructed at the hadron level and at the detector level. The resolutions are evaluated with the diffractive MC for 97.

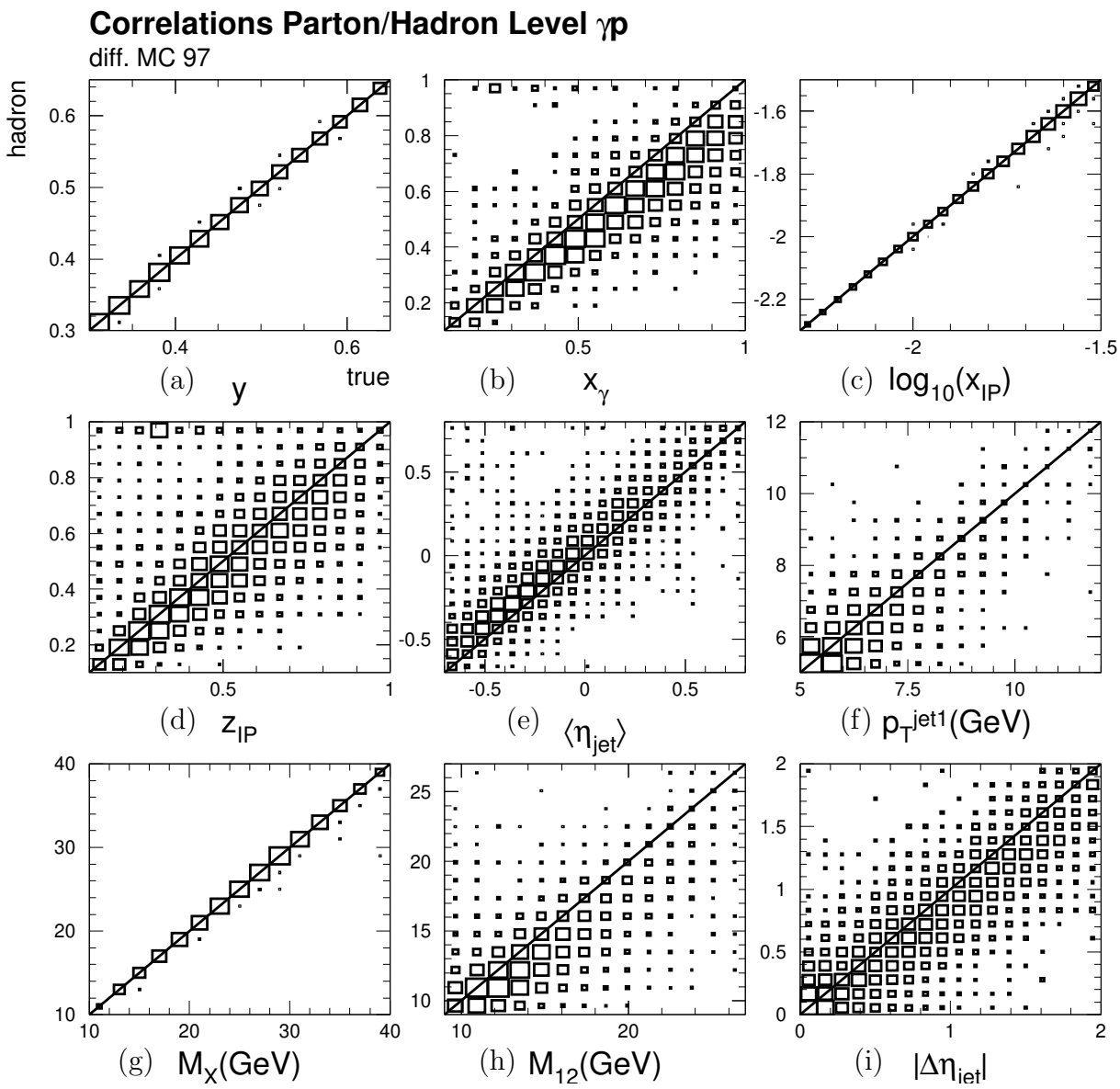

Fig. 5.3. Correlations between the variable at the parton level (horizontal axis) and reconstructed at the hadron level (vertical axis). The correlations are evaluated with the diffractive MC for 97.

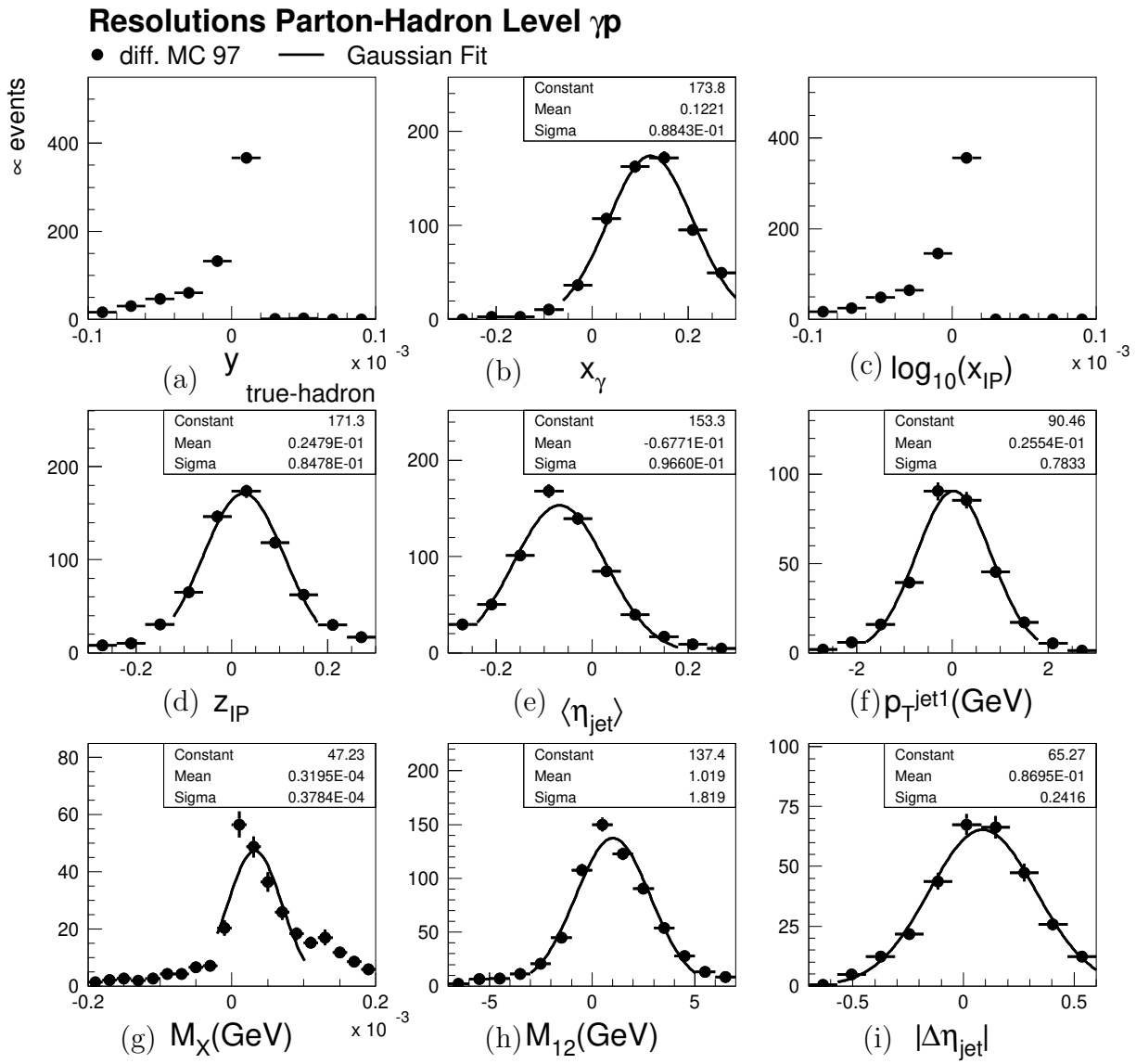

Fig. 5.4. Resolutions for reconstructing the parton level quantity at the hadron level. Shown is the difference between the variable as defined at the parton level and the variable reconstructed at the hadron level. The resolutions are evaluated with the diffractive MC for 97.

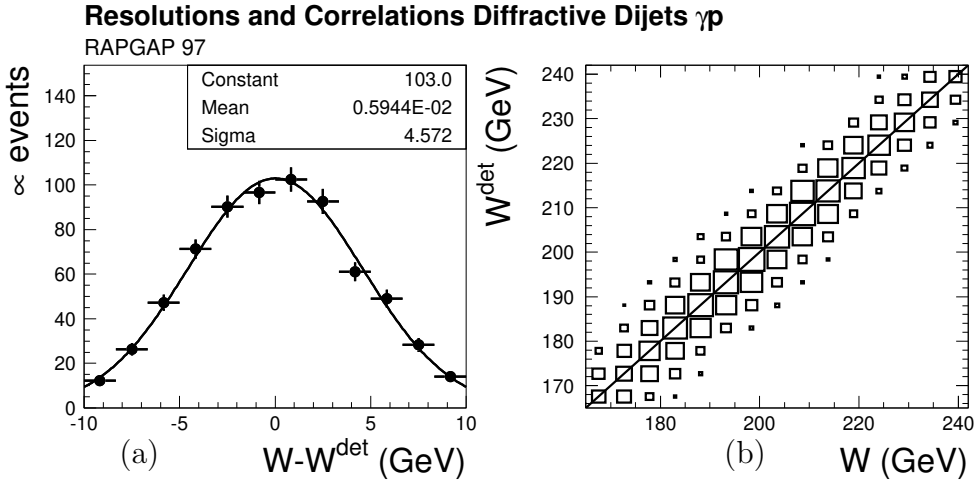

Fig. 5.5. Correlations for W evaluated with the diffractive model for 97. (a) The difference between the value reconstructed at the hadron level and the detector level. (b) The correlation between the hadron level W (horizontal axis) and the detector level W (vertical axis).

at both the detector and the hadron level. The quantity E_p denotes the proton beam energy and the sum runs over all objects in the X system. The parton level $x_{I\!P}$ is only available for the generated diffractive events. The difference between the logarithms of $x_{I\!P}$ reconstructed at the hadron level and at the detector level is shown in Fig. 5.2c. The quantities are well correlated and the resolution is 0.06. For the resolution displayed in Fig. 5.2c, only the range $-2.3 < \log x_{I\!P} < -1.5$ is considered. No diffractive cuts are applied in Fig. 5.1c to extend the range to larger values. It can be seen from Fig. 5.1c that the correlation is no longer diagonal for $\log x_{I\!P} > -1.4$ Instead, $x_{I\!P}$ is measured too small in the detector. This is due to the fact that the hadronic system X is no longer fully contained within the LAr calorimeter. This affects mainly the migrations in processes mediated by reggeon exchange which only contribute at a small fraction. The difference between the logarithms of $x_{I\!P}$ at the parton level and at the hadron level is of the order of $\approx 10^{-4}$ (Fig. 5.4c). The variables t and M_Y at the hadron level are reconstructed according to (2.3) and (2.3), respectively, from the hadron level system Y.

The invariant mass of the the dijet system is given by

$$M_{12} \equiv \sqrt{\left(p_{\mathrm{jet1}} + p_{\mathrm{jet2}}\right)^2}, \tag{5.3}$$

with p_{jet1} and p_{jet2} being the 4-momenta of the leading and sub-leading jet identified at the hadron or at the detector level, respectively. The difference between M_{12} reconstructed at the hadron and at the detector level is shown in Fig. 5.2h. The distribution is described by a Gaussian distribution with a mean value of 0.1 GeV and a width of $\sigma = 2.1$ GeV.

The corresponding quantity at the parton level is $\sqrt{\hat{s}}$. The variable M_{12} is on average reconstructed too low by 1.2 GeV compared to $\sqrt{\hat{s}}$ (Fig. 5.4h). This indicates that the jets reconstructed at the level of stable hadrons are not perfectly matched with the two outgoing partons of the hard subprocess. The resolution of the reconstruction at the hadron level is 1.8 GeV.

The estimator x_γ^{jets} on the fractional momentum of the parton from the photon entering the hard subprocess is reconstructed as

$$x_\gamma^{\text{jets}} = \frac{\sum_{\text{jets}} (E - p_z)}{2\, y\, E_e}, \tag{5.4}$$

at both the hadron and the detector level. The difference of these quantities is shown in Fig. 5.2b. The quantities are well correlated with a resolution of 0.1. Compared to the true x_γ, the quantity at the hadron level is on average reconstructed too low by 0.12 with a resolution of 0.08 (Fig. 5.4b). Again this stems from the fact that the jets and partons are not perfectly matched.

The estimator $z_{I\!P}^{\text{jets}}$ on the fractional momentum of the pomeron parton undergoing the hard scatter is calculated from

$$z_{I\!P}^{\text{jets}} = \frac{\sum_{\text{jets}} (E + p_z)}{2\, x_{I\!P}\, E_p}$$

at both the hadron and the detector level. The resolution of the detector level reconstruction with respect to the hadron level is 0.08 (Fig. 5.2d). The quantities are well correlated. The quantity at the hadron level is also well correlated with the parton level value (Fig. 5.4d). The resolution is 0.08 with the hadron level $z_{I\!P}$ being too small on average by 0.03.

Cross sections are also measured differentially in the transverse momentum of the leading jet p_T^{jet1}. The resolution at the detector level is 1.0 GeV (Fig. 5.2f) with respect to the hadron level. The hadron level p_T^{jet1} is well correlated with the p_T of the outgoing hard scattered partons (Fig. 5.4f). The resolution is 0.8 GeV.

The mean pseudorapidity $\langle \eta_{\text{jet}}^{\text{lab}} \rangle$ of the leading and sub-leading jet is reconstructed according to (2.14) The difference between $\langle \eta_{\text{jet}}^{\text{lab}} \rangle$ as reconstructed at the hadron and the detector level is displayed in Fig. 5.2e. The resolution is 0.05. The hadron level $\langle \eta_{\text{jet}}^{\text{lab}} \rangle$ is on average larger than the mean pseudorapidity of the two outgoing hard partons (Fig. 5.4e) by 0.06. The resolution is 0.09.

The jet separation $|\Delta\eta_{\text{jet}}|$ is reconstructed according to (2.14). The resolution at the detector level with respect to the hadron level quantity is 0.09 (Fig. 5.2i). The quantity at the hadron level is reconstructed too low by 0.08 with respect to the parton level (Fig. 5.4i). The corresponding resolution is 0.23.

All variables are well correlated between the hadron and the detector level. The kinematic region of the cross section is defined in terms of variables reconstructed at the hadron level. The correlation with the true parton level is not perfect. This is due to the fact that sometimes a hadron jet is identified which originates from partons produced in initial of final state QCD radiation.

5.2 Monte Carlo modelling of the data

For the correction of detector acceptance and resolution effects, Monte Carlo generated ep events are used which have been passed through a simulation of the H1 detector. A mixture of diffractive and standard photoproduction processes is used to model the data. To avoid double counting, these different processes are used in distinct regions of the phase space. The Monte Carlo program RAPGAP (cf. Sec. 2.3.1) is used in its diffractive mode to simulate events in the kinematic region

$$x_{I\!P}^{\mathrm{had}} < 0.05 \quad \text{AND} \quad M_Y = m_p.$$

The pomeron PDFs and the pomeron flux factor of the H1 fit 2 are used for the correction of the data.

The standard photoproduction Monte Carlo generator PYTHIA is used for

$$x_{I\!P}^{\mathrm{had}} > 0.05 \quad \text{OR} \quad M_Y > 5 \text{ GeV}. \tag{5.5}$$

In the remaining M_Y region $m_p < M_Y < 5$ GeV, the DIFFVM program is used to calculate the correction factor C_{M_Y}. It is not possible to include dijet predictions covering this M_Y region in the plots shown in the following sections because the DIFFVM model generates only vector mesons. Discrepancies between the data and the model could therefore be due to this missing piece in the model. In the following, the event sample of the PYTHIA standard photoproduction model is referred to as 'non-diffractive' because of the anti-diffractive cuts (5.5).

Normalisation of Monte Carlo models

The normalisation of the two different Monte Carlo model predictions is obtained from the $x_{I\!P}$ distribution shown in Fig. 5.11a and Fig. 5.12a for 96 and 97, respectively. The diffractive MC is normalised to describe the distribution in the low $x_{I\!P}$ region. The non-diffractive MC model is normalised such that the combination of both models gives a good description in the region around the analysis cut $x_{I\!P} < 0.03$. The cut is indicated by the vertical line. The normalisation of the non-diffractive MC determines the number of migrations from $x_{I\!P}^{\mathrm{had}} > 0.05$ into the kinematic range of the cross section measurement. These migrations are not incorporated in the correction factor C_{det} (cf. Sec. 5.5.2). Instead they are subtracted statistically from the data. Their number is found to be small at the level of a few percent. However, because of the bad description at large $x_{I\!P}$ (see below) a large uncertainty of 50% on the number of migrations is assumed as a systematic error. Fortunately, this gives negligible contributions to the total systematic error of the cross section.

Bad description at large $x_{I\!P}$

From Fig. 5.11a and Fig. 5.12a, it can be seen that the description becomes very bad for $\log x_{I\!P}^{\mathrm{det}} > -1.1$. Unfortunately, it is not possible to reweight the MC model to improve the description. A reweight has to use a variable which is defined at the hadron (or

γp selection

cut	reason
$\lvert z_{\text{vtx}}\rvert < 35$ cm	veto beam/gas, beam/pipe bgr.
$E_{\text{PD}} < 0.5$ GeV	Bethe-Heitler processes
coherent noise veto	
cosmics veto	
$Q^2 < 0.01$ GeV^2	electron detector acceptance
$165 < W < 242$ GeV	
$\lvert X_{\text{el}}\rvert < 6.5$ cm	

Tab. 5.1. Summary of the selection of inclusive photoproduction events.

parton) level. For the non-diffractive Monte Carlo model, however, there is almost no correlation between $x_{I\!P}$ as reconstructed at the hadron and at the detector level. However, no migrations occur from $x_{I\!P}^{\text{had}} < 0.03$ (which defines the cross section) to $\log x_{I\!P}^{\text{det}} > -1.0$. Following the arguments in Sec. 4.7, it is concluded that the $\log x_{I\!P}^{\text{det}} > -1.0$ region is irrelevant for this analysis. A cut $x_{I\!P}^{\text{det}} < 0.1$ will be applied in the control plots of the 'inclusive' sample to reject this region.

5.3 Event selection

This section describes the selection criteria imposed to isolate the diffractive dijet events used for the cross section measurement. The selection of inclusive photoproduction events is summarised in Tab. 5.1.

5.3.1 Basic event selection

The analysis uses events for which the following detector components were in full operation: luminosity system, liquid argon calorimeter (LAr), central jet chambers (CJC) 1 and 2, forward muon detector, backward calorimeter (SPACAL), proton remnant tagger (PRT) and time of flight system (ToF).

5.3.2 Triggers and trigger efficiency

Photoproduction dijet events are triggered by requiring an electron in the small scattering angle detector (electron tagger), an event vertex, and large transverse momentum tracks in the central region of the detector.

Electron trigger

The electron is measured in the 33 m electron detector. The electron detector trigger requires energy above 7.5 GeV in 96 and above 9 GeV in 97. The electron detector

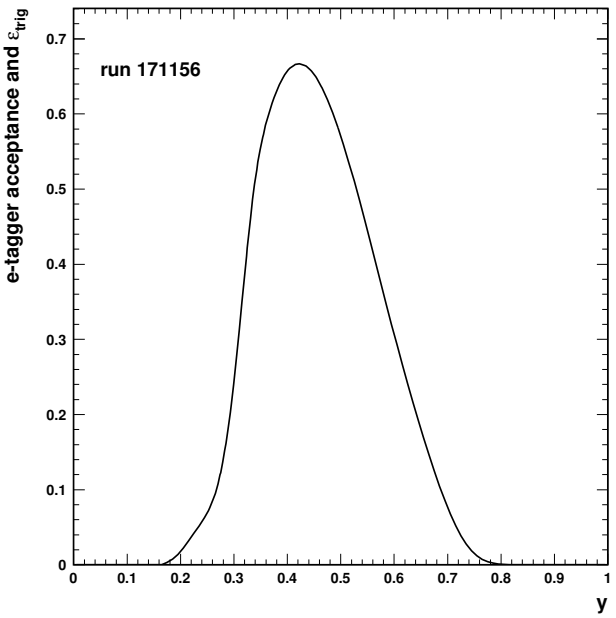

Fig. 5.6. Parameterisation of the electron detector acceptance and trigger efficiency. It is shown as a function of the generated inelasticity y for a run of the 97 running period.

acceptance and trigger efficiency depends critically on the electron beam optics. Because the optics change frequently these changes are not included in the H1 detector simulation. This makes it necessary to parameterise the acceptance and trigger efficiency by hand [34]. The parameterisation is done as a function of the generated inelasticity y which is related to the energy of the scattered electron. The parameterisation is shown in Fig. 5.6 for a typical run in 97. The Monte Carlo model is weighted according to this parameterisation. The electron detector inefficiency is therefore covered in the correction factor C_{det}. In all plots shown in this chapter, the weight is applied to the MC events. In the region $0.3 < y < 0.65$ the average weight is ≈ 0.50 for 96 and ≈ 0.43 for 97. The difference is due to the higher trigger threshold energy in 97 and different electron beam optics in 96 and 97.

Vertex and track triggers

To identify an event vertex, signals from two MWPC layers of the central tracker are used. Straight line tracks are formed by combining hit pairs in the different layers. The vertex trigger fires if several of these tracks come from the same region in z along the beam line. The track trigger is based on signals from the CJC and requires at least one track with transverse momentum larger than 800 MeV.

The efficiency for triggering a jet with the vertex and track triggers depends on the transverse momentum p_T and on the direction of the jet. Jets with larger p_T contain more tracks or tracks with larger p_T. Both properties increase the trigger efficiency. If only part of the jet goes through the tracking device (the rest being detected solely in the calorimeter) the trigger efficiency is decreased because less tracks are detected.

Backward activity veto

In 96, the trigger setup contained a veto on activity in the backward region. If there are signals in more than three sectors of the backward quarter of the CIP the event is rejected. The intention was to remove proton-gas and proton-beam wall background interactions which take place upstream the proton beam ($z < 0$). However, the veto can also be triggered by the photon remnant in resolved photoproduction events. This leads to a reduced efficiency for detecting these events. In 97, this veto was removed from the trigger.

Trigger efficiency

The trigger efficiency for the electron detector is included in the acceptance parameterisation (cf. Sec. 5.3.2). The efficiency of the other trigger requirements is determined using monitor triggers. A monitor trigger is independent of the analysis trigger and therefore provides a sample of unbiased events. The trigger efficiency is determined as the fraction of events in the monitor trigger sample for which the analysis trigger fires. The trigger efficiency is evaluated by multiplying the efficiencies of the individual trigger elements. Correlations between the trigger elements were examined with the trigger simulation and found to be negligible.

The trigger efficiency without the electron detector efficiency is shown in Fig. 5.7 for the combined 96 and 97 diffractive photoproduction dijet sample. The overall efficiency is 84% for 96 and 94% for 97. For 96 the trigger efficiency is reduced because of the backward veto. The backward veto trigger efficiency is parameterised linearly in x_γ and is applied only for 96. The tracking trigger efficiency is parameterised two-dimensionally as a function of the p_T of the leading jet and the average jet pseudorapidity. The vertex and tracking efficiency was extracted from the inclusive dijet data sample because very few monitor trigger events remain after diffractive cuts. The trigger efficiency exhibits a rise with x_γ which is due to the backward veto. The trigger efficiency decreases slightly when the jets are located in the forward region and their tracks are not fully detected within the CJC. This can be seen in the η_{jet} distribution. The tracking efficiency increases with the p_T of the jets because more particles are produced.

5.3.3 Raw event rate and integrated luminosity

Shown in Figs. 5.8a and b is the accumulated number of diffractive dijet events as a function of the integrated luminosity. The plots Figs. 5.8c and d show the number differentially per luminosity as a function of the integrated luminosity. The number of raw events found after all cuts is 537 for 96 and 828 for 97. The number of events shown in the figure is corrected for trigger inefficiencies and multiplied by the prescale factor of the trigger which is 1.026 on average for 96 and 1.008 for 97. The integrated luminosities for 96 and 97 are 7.02 pb^{-1} and 10.74 pb^{-1}, respectively. Within the statistical errors, the differential event rate is stable.

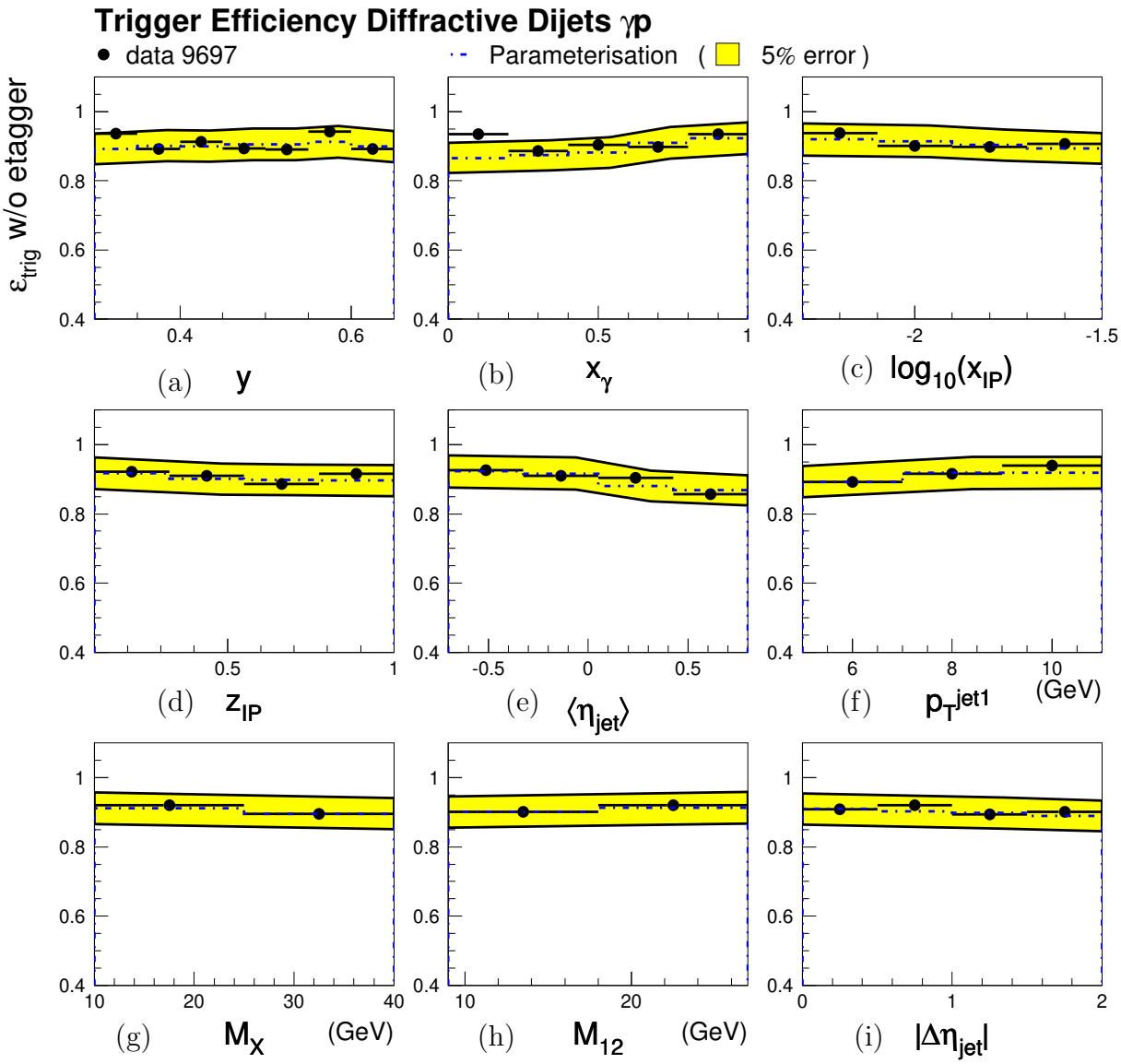

Fig. 5.7. Trigger efficiency for diffractive photoproduction dijets without the efficiency of the electron detector. Also shown as the dotted line is the parameterisation which is used for the correction of the data. A ±5% band around the parameterisation is indicated which is taken as the uncertainty of the trigger efficiency.

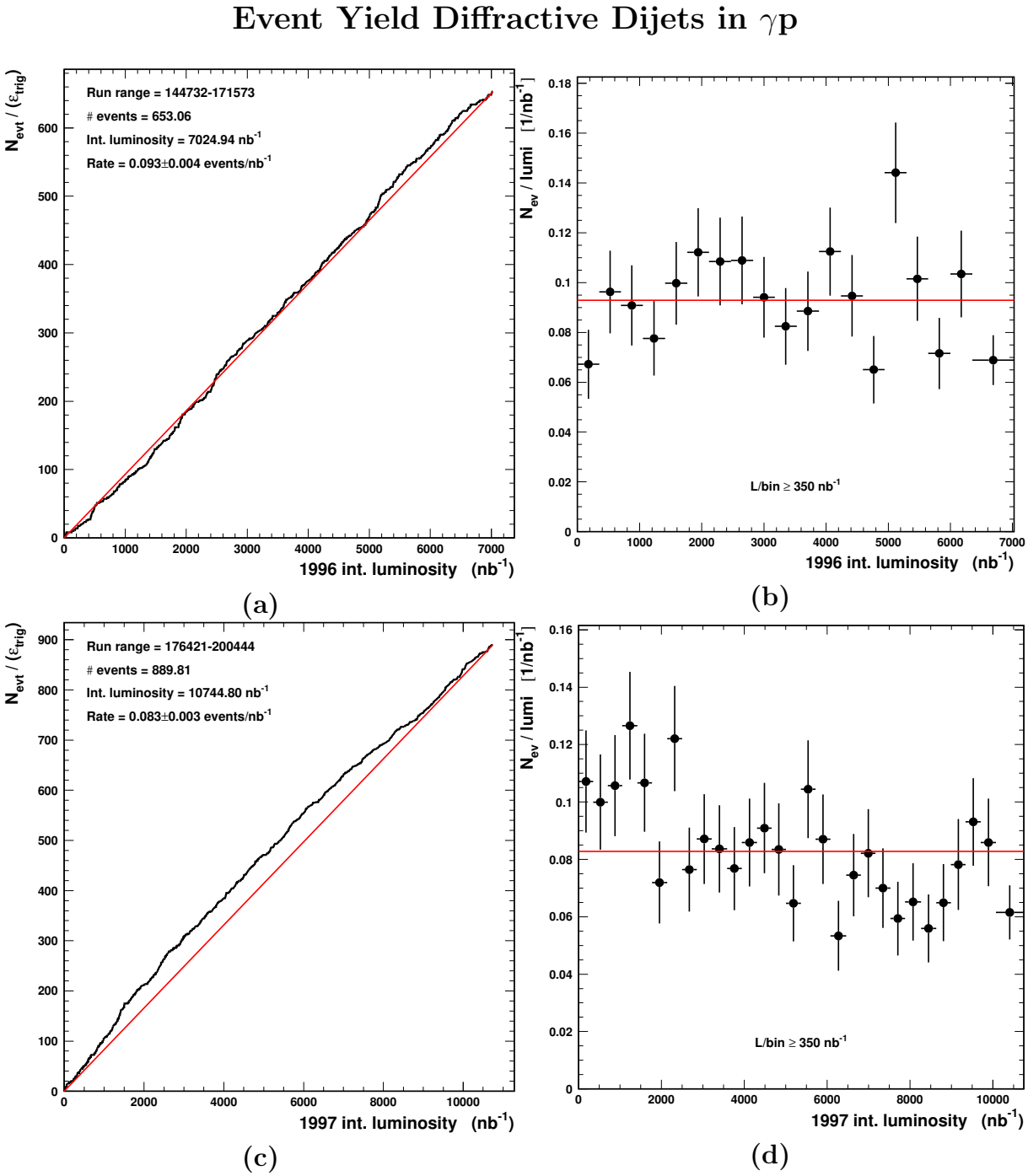

Fig. 5.8. Yield of diffractive photoproduction dijet events. Shown in (a) for 96 and (b) for 97 is the number of accumulated diffractive dijet events as a function of the integrated luminosity. The accumulated number of events is shown per luminosity in (b) for 96 and (d) for 97 as a function of the integrated luminosity. The number of events is corrected for the inefficiency of the trigger elements not related to the electron detector. The trigger inefficiency of the electron detector is not taken into account. The number of events is multiplied by the prescale factor of the trigger.

5.3.4 Electron detector cuts

The electron detector is placed at very small scattering angles. From the geometrical acceptance and the efficiency for detecting electrons result the analysis cuts

$$Q^2 < 0.01 \text{ GeV}^2, \quad 165 < W < 242 \text{ GeV}.$$

The range in W corresponds to the range $0.3 < y < 0.65$ in which the scattered electron has energies between 9.6 and 19.3 GeV. The y distribution is shown in Fig. 5.9a. The Monte Carlo has been reweighted to improve the description. The dotted histogram shows the original prediction before the reweighting. The MC includes the weight of the electron detector acceptance parameterisation.

The electromagnetic shower measured in the electron tagger must be fully contained within the detector. A cut on the position of the centre of the shower is therefore applied:

$$|X_{\text{el}}| < 6.5 \text{ cm}.$$

This cut is only applied to the data but is taken into account in the acceptance parameterisation.

5.3.5 Photon detector energy

A cut is applied on the photon detector energy E_{PD} as a veto against Bethe-Heitler processes:

$$E_{\text{PD}} < 0.5 \text{ GeV}.$$

The distribution is shown Fig. 5.9b. A small fraction of the events is lost due to Bremsstrahlung. The description by the model is not particularly good because the detector simulation does not take into account the various changes of the electron beam optics. The photon detector energy distribution is sensitive to these changes and is not reproduced correctly. However, because the correction is only small, no further measures were taken.

5.3.6 Event vertex requirement

An event vertex must have been found by the tracking system. The z component of the vertex is required to lie around the nominal interaction point at $z = 0$:

$$|z_{\text{vtx}}| < 35 \text{ cm}.$$

This cut rejects background events from beam-gas or beam-beampipe interactions. Fig. 5.9c shows the z_{vtx} distribution for the inclusive dijet sample for 97. The data are corrected for trigger inefficiencies (other than those related to the electron detector). The original distribution of the Monte Carlo events are shown as the dotted histogram. The z_{vtx} distribution is produced during the detector simulation (`H1SIM`). In the original generator output, the event vertex is located at the origin for every event. That the z_{vtx} distribution is not correctly described is a failure of the detector simulation and has nothing to do with the physics model implemented in the Monte Carlo generator. The description is

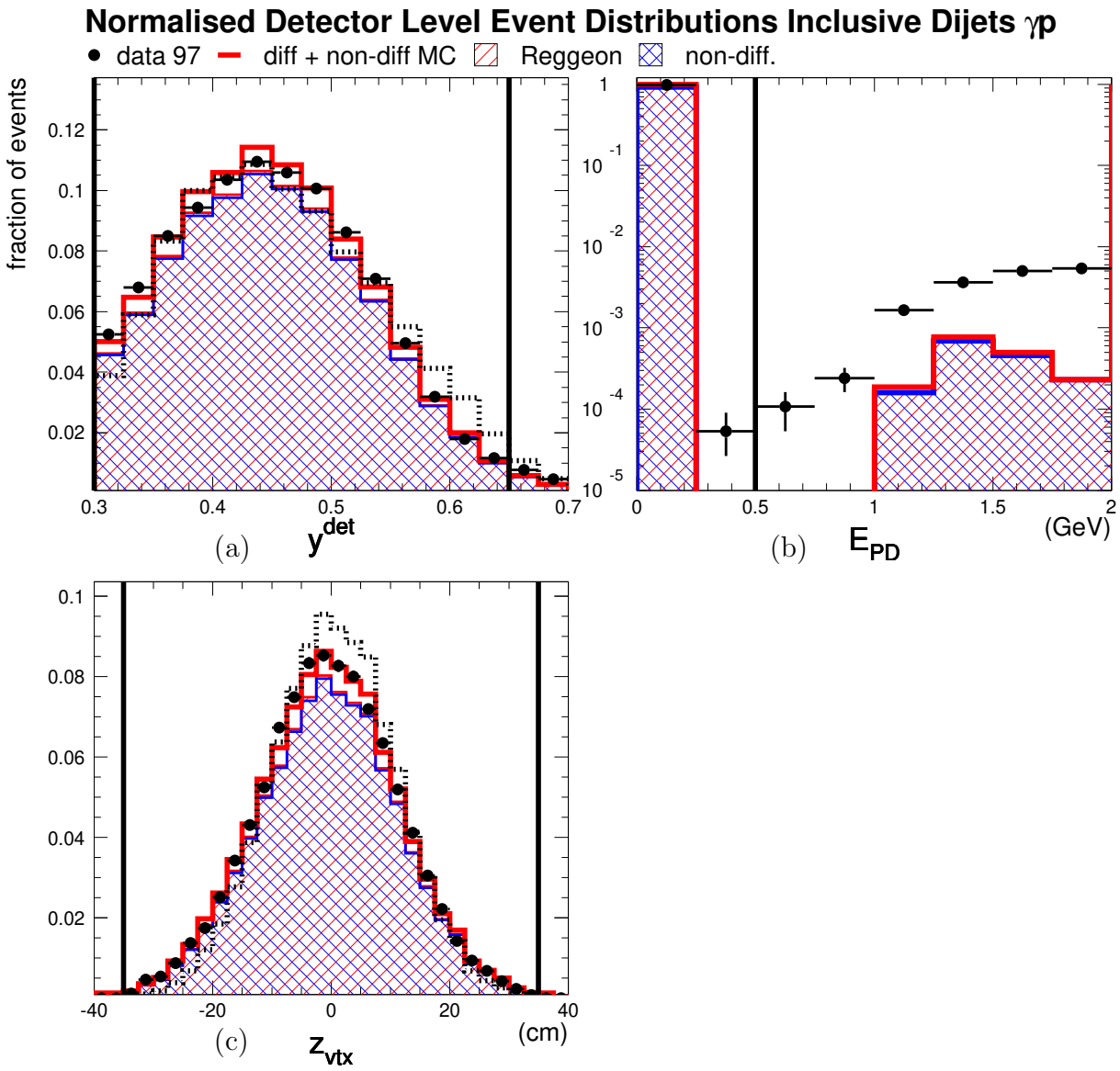

Fig. 5.9. Normalised distributions for the inclusive γp dijet sample of 97 with an additional cut $x_{I\!P} < 0.1$. (a) The y_{etag} distribution of the Monte Carlo has been reweighted. The original prediction is shown as the dotted histogram. (b) The energy in the photon detector. (c) The z component of the reconstructed vertex position. The z_{vtx} distribution of the MC has been reweighted. The original prediction is shown as the dotted histogram.

improved by reweighting the Monte Carlo events. The ratio of the z_{vtx} distributions of the data and the MC events was fitted by a polynomial. This function defines the weight which is applied to the MC as a function of the z component of the simulated vertex. A less significant reweighting was also done for 96. For the diffractive sample, the z_{vtx} distribution is described within the large statistical errors of the data.

5.3.7 Reconstruction of the hadronic final state

The final state hadrons are reconstructed making use of the complementary advantages of the calorimeter and the tracking detectors. High energy particles can be precisely measured in the calorimeter. However, low energetic particles cannot be detected efficiently because they give rise to signals which are similar to electronic noise clusters which have to be removed from the event. In addition, particles lose energy in the dead material in front of the calorimeter. The situation is different for the tracking system. The transverse momentum p_T is calculated from the curvature of the track derived from the signals created by a charged particle. For high p_T particles, the curvature is too small and the transverse momentum cannot be reconstructed with good precision.

An algorithm [35] is used which combines tracks and calorimeter clusters into so-called 'combined objects.' Tracks are used for $p_T < 2$ GeV. Double counting of energies is avoided in the following way. If a track points at a calorimeter cluster the energy of the track is removed from the cluster energy. The combined objects are used as input objects for the hadronic final state reconstruction.

5.3.8 Dijet selection

The inclusive k_T jet algorithm [36] with a distance parameter of unity is used to identify jets. Combined objects formed from both calorimeter clusters and tracks with $p_T < 2$ GeV are used as input to the jet algorithm (cf. Sec. 5.3.7). The transverse energy of the leading jet is required to be larger than 5 GeV. The transverse energy of the subleading jet must be larger than 4 GeV:

$$E_T^{\text{jet}(1)} > 5 \text{ GeV}, \quad E_T^{\text{jet}(2)} > 4 \text{ GeV}.$$

The asymmetric transverse energy cuts are applied to allow comparisons with NLO predictions. The jets are required to lie within the central acceptance region of the calorimeter:

$$-1 < \eta^{\text{lab}}_{\text{jet}(1,2)} < 2.$$

The dijet selection is summarised in Tab. 5.2.

Dijet distributions are shown in Fig. 5.10 for the inclusive photoproduction sample of 97. The transverse momentum of the leading jet (Fig. 5.10a) is steeper in the MC than in the data. However, because the number of non-diffractive background events after diffractive cuts is small, the non-diffractive MC is not reweighted. The description of the mean pseudorapidity of the two leading jets is good (Fig. 5.10b).

Dijet selection

inclusive k_T jet algorithm
distance parameter 1.0
$N_{\text{jet}} \geq 2$
$E_T^{\text{jet}(1)} > 5$ GeV
$E_T^{\text{jet}(2)} > 4$ GeV
$-1 < \eta_{\text{jet}(1,2)}^{\text{lab}} < 2$

Tab. 5.2. Summary of the dijet selection. For DIS, the jet transverse momentum cut is applied in the γp system.

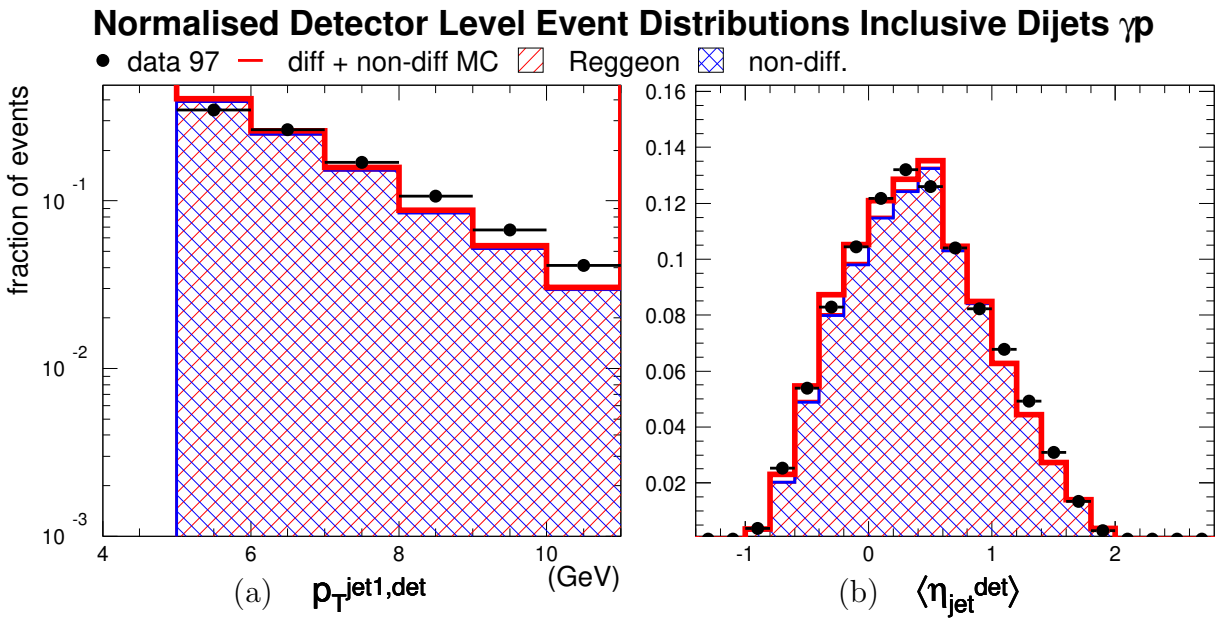

Fig. 5.10. Dijet distributions for the inclusive γp dijet sample of 97. (a) transverse momentum of the leading jet, (b) mean pseudorapidity of the two leading jets.

5.3.9 Selection of diffractive events in photoproduction

Diffractive events are selected by requiring the absence of activity in the detectors between the outgoing proton system Y and the centrally produced hadronic system X. The energy flow between the edge of the LAr calorimeter and the proton direction can only be measured very poorly with the FMD and the PRT. These detectors are used to reject non-diffractive and diffractive dissociation events. The cuts also reject genuine diffractive events in which the pomeron remnant deposits energy in the forward direction or diffractive events at large $|t|$ in which the proton is scattered into the PRT. At low $|t|$, the elastically scattered proton cannot be detected. Events in which the proton dissociates into a low mass excitation can also not be detected efficiently. The final cross section is therefore given for the range $M_Y < 1.6$ GeV and $-t < 1$ GeV^2. The diffractive selection is summarised in Tab. 5.3. After all cuts, the data sample consists of 537 events for 96 and 828 for 97. The contribution of events from $x_{I\!P}^{\mathrm{had}} > 0.05$ is 2% for 96 and 4% for 97.

5.3.9.1 Cut on $x_{I\!P}$

The variable $x_{I\!P}$ is reconstructed according to (5.2) and is sensitive to the energy in the forward region of the LAr calorimeter. Fig. 5.11a and Fig. 5.12a show the distribution of $x_{I\!P}$ for the inclusive photoproduction dijet sample of 96 and 97, respectively. Events at large $x_{I\!P}$ are mostly due to non-diffractive photoproduction. To reduce this background, the cut

$$x_{I\!P}^{\mathrm{det}} < 0.03 \tag{5.6}$$

is applied. For a discussion of the bad description at large $x_{I\!P}$ see Sec. 5.2.

5.3.9.2 Cut on most forward cluster in the LAr calorimeter

The variable η_{max} is defined as the pseudorapidity of the most forward LAr cluster with energy above 400 MeV. Clusters with smaller energy are considered as electronic noise. A small value of η_{max} implies a large rapidity gap in the event because it indicates that there is no activity in the LAr calorimeter between η_{max} and the forward edge of the calorimeter at $\eta_{\mathrm{max}}^{\mathrm{LAr}} \approx 3.6$.

Fig. 5.11b and Fig. 5.12b show the η_{max} distribution for the inclusive photoproduction dijet sample with an additional cut $x_{I\!P} < 0.1$ applied to reject the badly described region at large $x_{I\!P}$. The distribution is underestimates the production rate for $\eta_{\mathrm{max}} < 3.2$. This is related to the missing proton dissociation events in the MC which are treated separately. The diffraction model can describe the tail in the data distribution while the non-diffractive photoproduction model is exponentially suppressed with increasing rapidity gap size. A cut

$$\eta_{\mathrm{max}} < 3.2 \tag{5.7}$$

is applied to decrease the non-diffractive contributions. The η_{max} cut is applied only at the detector level, the hadron level definition of the diffractive cross section involves only $x_{I\!P}$, t and M_Y.

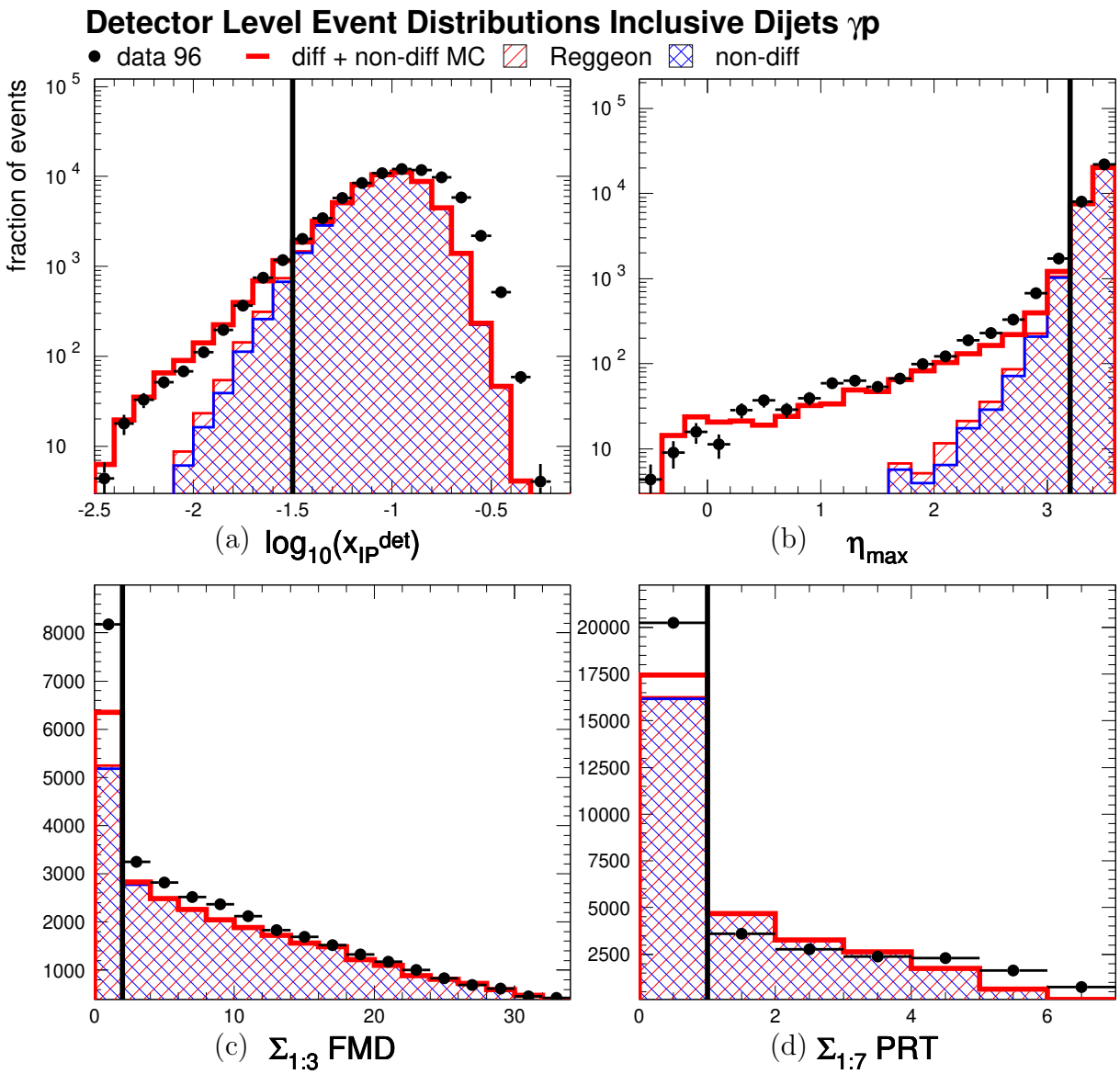

Fig. 5.11. Distributions of the inclusive γp dijet sample of 96. (a) $x_{I\!P}$, (b) $\eta_{\max}$, (c) FMD and (d) PRT. For (c), FMD noise has been added in the MC.

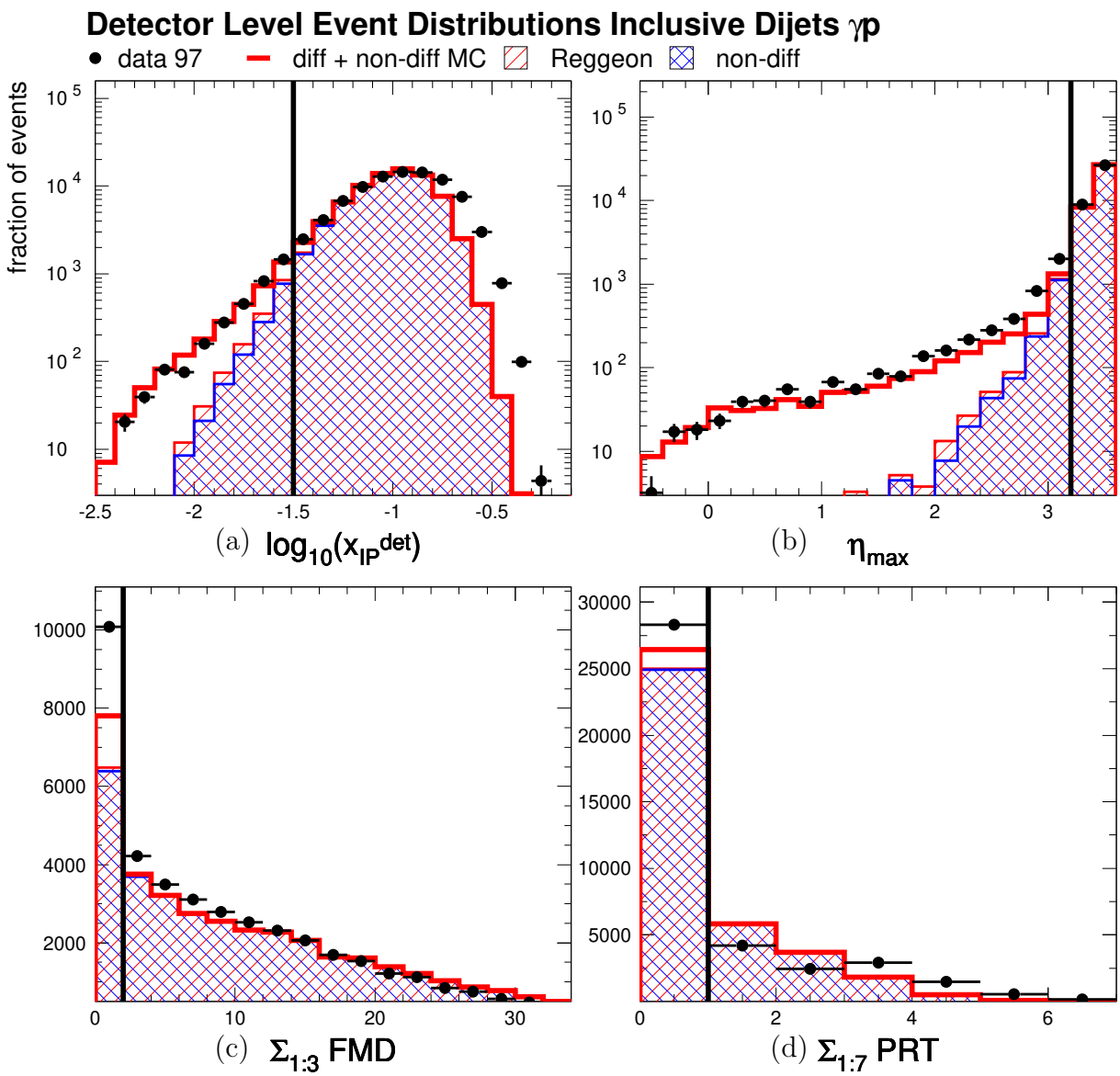

Fig. 5.12. Distributions of the inclusive γp dijet sample of 97. (a) $x_{I\!P}$, (b) $\eta_{\max}$, (c) FMD and (d) PRT. For (c), FMD noise has been added in the MC.

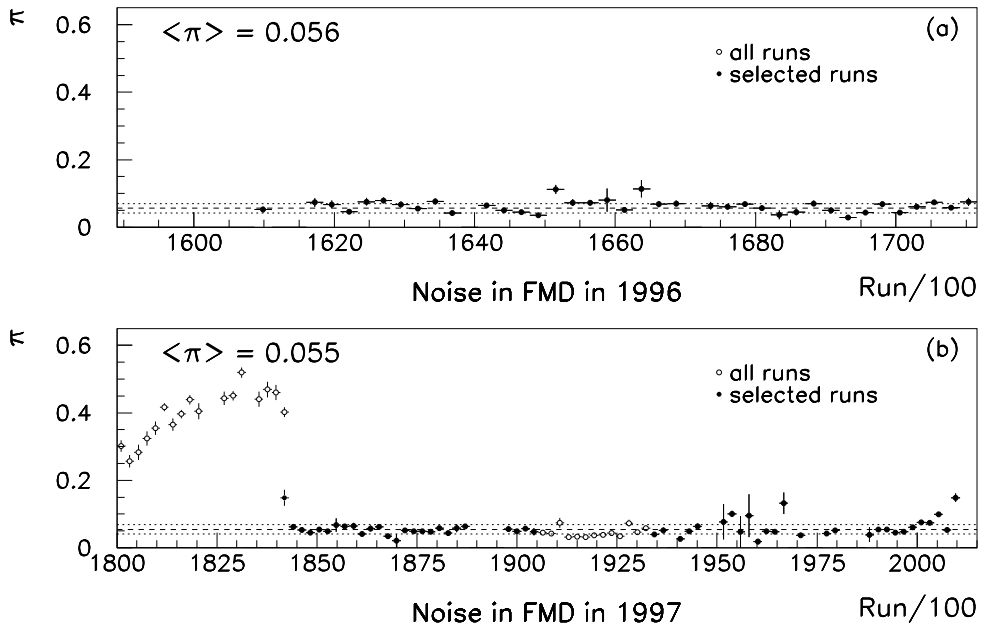

Fig. 5.13. Noise in the FMD for (a) 96 and (b) 97 as a function of the run number. Shown is the fraction π of random trigger events fulfilling the cuts $\sum_{1:3}$ FMD $> 1, \eta_{\max} < 3.2$. The region at the beginning of 97 is not included in the analysis (from [37]).

5.3.9.3 Activity in the FMD

For another veto against hadronic activity between X and the proton system Y, the forward muon detector is used. The number of hit pairs in the three pre-toroid drift chambers of the FMD must be smaller than 2:

$$\sum_{1:3} \text{FMD} \equiv \text{FMD hit pairs (pre} - \text{toroid)} < 2. \tag{5.8}$$

One hit pair is allowed as this occurs frequently due to noise fluctuations.

Noise in the FMD

Electronic noise had to be added to the hit distribution of the MC at the analysis level because it is not included in the H1 detector simulation. The noise has been determined from random trigger files in [37] for the same running period as under study in the present analysis. Therefore, the determined noise fraction can therefore also be used in the present analysis. The procedure is explained in the following. The fraction π of events fulfilling the cuts

$$\sum_{1:3} \text{FMD} > 1 \quad \text{AND} \quad \eta_{\max} < 3.2$$

is determined as a function of the run number. The $\eta_{\max}$ cut is applied to avoid double counting of noise in the LAr calorimeter which is already included in the detector simulation. The result is shown in Fig. 5.13. The noise is at a level of $(5.5 \pm 1.4)\%$ indicated

by the dashed line. The period with large noise fractions at the beginning of 97 is not used in the analysis. These apparent large noise fractions are not related to real noise in the muon chambers but are due to a failure in the data taking chain which lead to event mixing.

The distribution of FMD hit pairs multiplicity is shown in Fig. 5.11c and Fig. 5.12 with FMD noise included in the MC. The cut $x_{I\!P} < 0.1$ has been applied in these plots. The overall shape is described. However, the MC predicts too few events with less than 10 hit pairs. This is due to the fact that the DIFFVM model prediction is missing in the plot. The FMD noise is included in the MC only in these two figures. In all other comparisons the MC does not contain FMD noise. This is because the effect of the noise can be approximated by an overall normalisation factor, see Sec. 5.5.5.

5.3.9.4 Hits in the PRT

The proton remnant tagging detector is used to veto non-diffractive and proton dissociation events. It covers the region $6 < \eta < 7.5$. No hits in the 7 scintillators are allowed:

$$\sum_{1:7} \text{PRT} \equiv \text{sum of PRT hits} = 0.$$

Originally, the description of the PRT hit spectrum by the MC models was bad. In principle, this could be due to two reasons.

- The simulation (`H1SIM`) of the PRT and FMD, of the material surrounding either detector or the beam pipe, or the beam optics is inadequate.
- The physics model implemented in the Monte Carlo generator gives an incorrect prediction for the forward energy flow.

Both effects have been studied in [38] for D^* production in DIS. The efficiency of the PRT to detect events with forward activity was examined. These events were selected by requiring

$$\eta_{\max} > 3.3 \quad \text{AND} \quad \sum_{1:3} \text{FMD} > 1.$$

The efficiency was determined separately for each of the 7 scintillators and for each of the 95, 96 and 97 running periods. In the data, the scintillators showed reduced response due to aging. This behaviour is not reproduced by the detector simulation.

To study the influence of the physics model, two models were compared which differ in the modelling of higher order effects. The ARIADNE generator [39] was used as an implementation of the colour dipole approach. It is compared with the LEPTO generator [40] which uses parton shower cascades. Both models give almost the same description of the PRT efficiency. From that it was concluded that the effect is largely due to an inadequate simulation of the detector. The Monte Carlo efficiency of the PRT was then reweighted to that observed in the data. It is noted that the reweighting coefficients were obtained from non-diffractive events. Using these coefficients it was then found that the PRT hit distribution for diffractive events is improved significantly.

Diffractive selection

$x_{I\!P} < 0.03$
$\eta_{\max} < 3.2$
$\sum_{1:3}$ FMD < 2
$\sum_{1:7}$ PRT $= 0$

Tab. 5.3. Summary of the diffractive selection cuts.

The original description of the PRT hit multiplicity was also found to be bad in [37] for dijet production in DIS. In this analysis, the reweighting coefficients were determined from non-diffractive events selected with the cuts

$$\eta_{\max} > 3.2 \quad \text{AND} \quad \sum_{1:3} \text{FMD} > 1.$$

Using the same procedure as in [38], the Monte Carlo efficiency was reweighted to that observed in the data. Nearly the same coefficients were found in both analyses. The fact that the same reweight is necessary in two different kinematic ranges (D^* and dijet production) gives more confidence that the problem with the PRT description is due to the detector simulation. For the analysis presented here, the reweighting constants from [37] are used.

The distribution of PRT hits after the reweight is shown in Fig. 5.11d and Fig. 5.12d for diffractive dijet events. The description is good for both years.

5.4 Control plots for diffractive dijets in photoproduction

In this section, further control plots are presented which show that the Monte Carlo model describes the data distributions and can therefore be used for the correction.

5.4.1 Description of kinematic variables in photoproduction

Distributions for the cross section variables are shown in Fig. 5.14 and Fig. 5.15 for the diffractive dijet samples of 96 and 97, respectively. The relative normalisation of the two Monte Carlo components is different from the inclusive case. The normalisation of the non-diffractive MC has been obtained from a fit to the $x_{I\!P}$ distribution of the inclusive data sample and is left unchanged. The normalisation of the diffractive MC is reduced by approximately 45% such that the sum of the numbers of the diffractive and non-diffractive events are equal to the number of data events. This reduction is necessary because the inclusive sample from which the normalisation was originally obtained includes proton dissociation events which are not included in the Monte Carlo in the range $m_p < M_Y < 5$ GeV. This region is covered separately by the correction factor C_{M_Y} which is evaluated with the DIFFVM program. One could argue that the normalisation of the non-diffractive MC should also be reduced. This approach is not adopted because it is not clear where the proton dissociation events would contribute to the $x_{I\!P}$ distribution in diffractive dijet production. However, a 50% systematic uncertainty is assumed on the

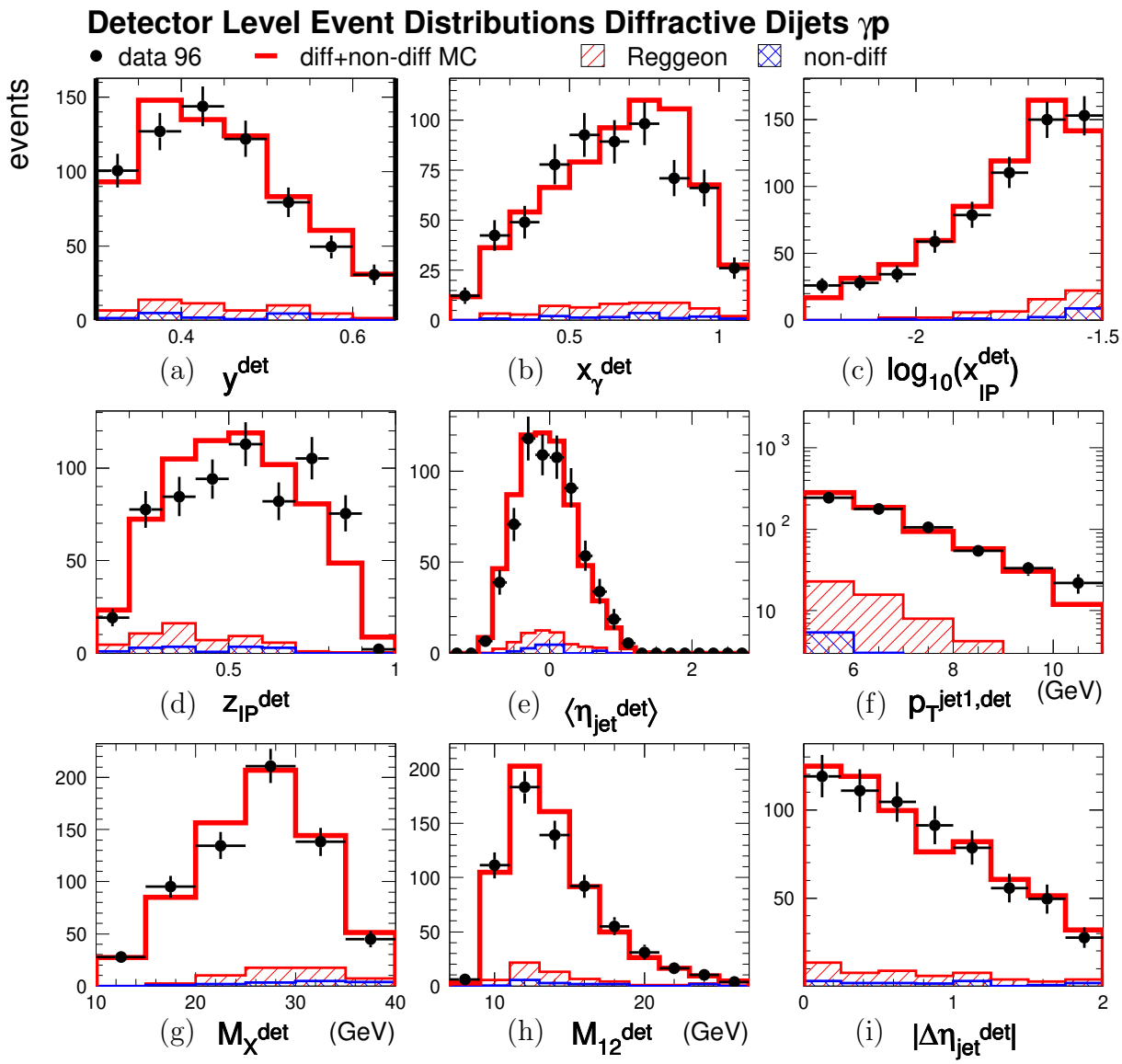

Fig. 5.14. Diffractive dijet photoproduction distributions for 96. The diffractive model is only reweighted in z_{vtx}. The number of MC events is normalised to the number of data events.

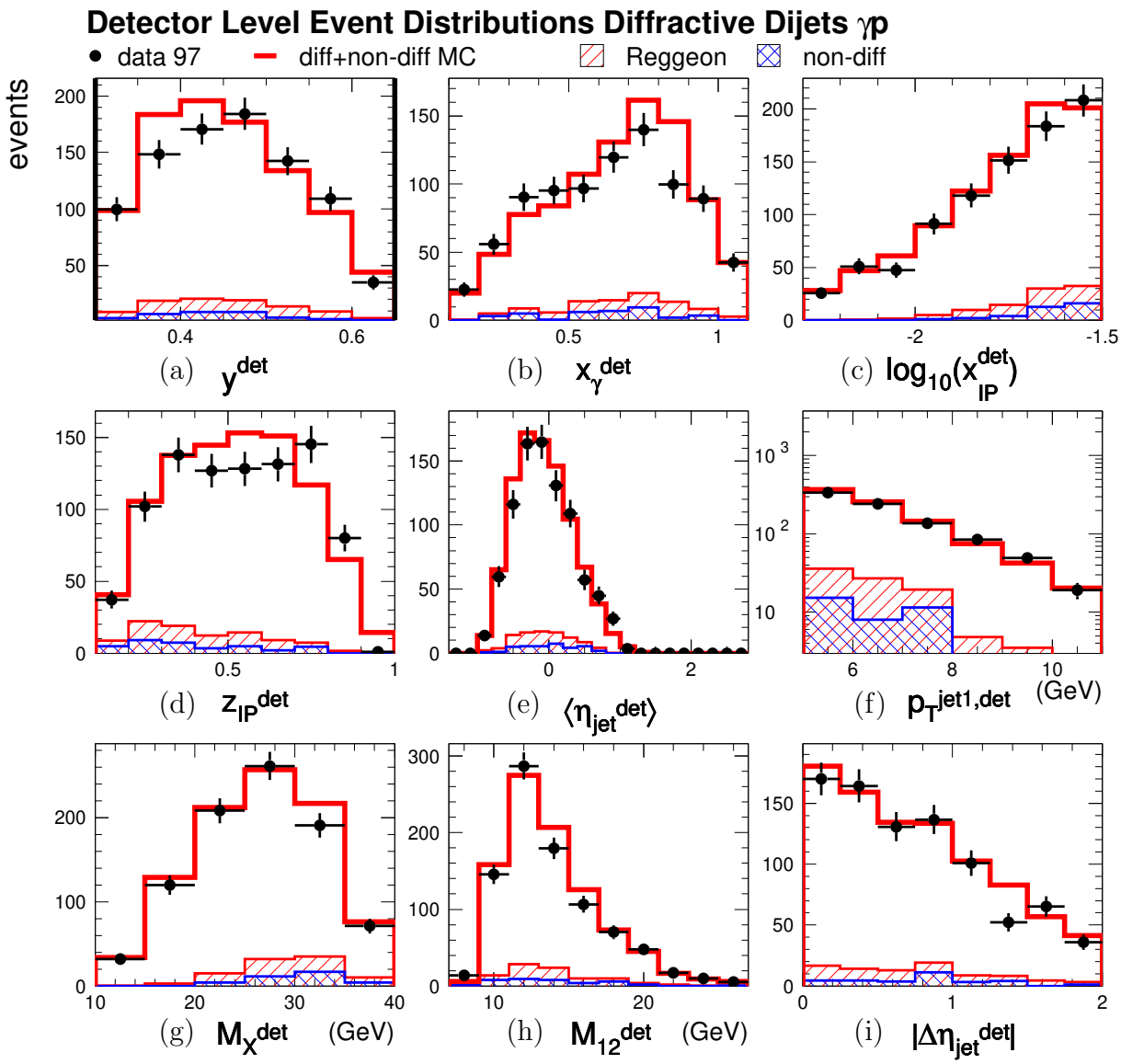

Fig. 5.15. Diffractive dijet photoproduction distributions for 97. The diffractive model is only reweighted in z_{vtx}. The number of MC events is normalised to the number of data events.

number of non-diffractive events in the final selection. The possible reduction factor is covered by this uncertainty. The diffractive model was reweighted in z_{vtx}. The distributions of all variables are reasonably well described. Remaining discrepancies are covered by the systematic error on the correction factor C_{det}. This is discussed in Sec. 5.6.2.

5.4.2 Energy flow in diffractive photoproduction dijet events

In order to use the Monte Carlo for the detector smearing correction the model must also describe the distributions of the basic calorimeter clusters and tracks.

Fig. 5.16 shows the mean energy flow in a diffractive dijet event as a function of the pseudorapidity calculated in the laboratory frame. Only events are considered in which the jet axes satisfy $\eta_{\mathrm{jet}} < 1$. With this cut it is ensured that the forward region which is critical for the diffractive selection is devoid of energy belonging to a jet. In Fig. 5.16a, the energy is reconstructed from the combined objects of calorimeter clusters and tracks. The energy obtained from actually matched clusters and tracks is shown in Fig. 5.16b whereas only clusters and only tracks are used for Fig. 5.16c and Fig. 5.16d, respectively. The average multiplicity of the objects is shown in Fig. 5.17. The description is not perfect in the central region $-2 < \eta < 1$ which is covered by the LAr calorimeter and where most of the energy is deposited. The description of the energy is equally mediocre for both tracks and clusters. The multiplicity of the tracks is well reproduced by the model. In the forward region, the model gives a good description of the particle flow. Energy and multiplicity of both tracks and calorimeter clusters are well described. This can also be seen in Fig. 5.18 which shows the average energy per event reconstructed from LAr calorimeter cells for dijet events fulfilling the diffractive cuts

$$x_{I\!P} < 0.03 \quad \text{AND} \quad \sum_{1:3} \mathrm{FMD} < 2.$$

Fig. 5.18a shows the energy as a function of the pseudorapidity in the laboratory frame. The model is in good agreement with the data for $\eta > 1.5$. Fig. 5.18b shows the cell energy in the forward part of the LAr calorimeter ($270 < z < 450$ cm) as a function of the radial distance R from the beam axis. The data are very well described by the model.

Fig. 5.19 shows jet profiles of the leading jet in the laboratory system. The mean transverse energy per event around the jet is shown as a function of the pseudorapidity in Fig. 5.19a. Only energy in the Φ hemisphere of the leading jet has been considered to eliminate contributions from the subleading jet which typically is aligned back-to-back with the leading jet. The distribution is well described by the model. The average transverse energy per event as a function of the azimuthal angle Φ is displayed in Fig. 5.19b. Only energy within a pseudorapidity band $\eta_{\mathrm{jet1}} \pm 1$ around the leading jet is considered. The description is fine. Some minor discrepancies are seen in (b) in the region where the subleading jet contributes. The energy between the jets is well described. In this respect it is noted that the diffractive RAPGAP model does not include any multiple interactions between the photon remnant and the other hadronic systems (the outgoing proton system or the pomeron remnant). This means that in diffraction the underlying event energy is small. This is in contrast to inclusive dijet photoproduction where the effect is significant.

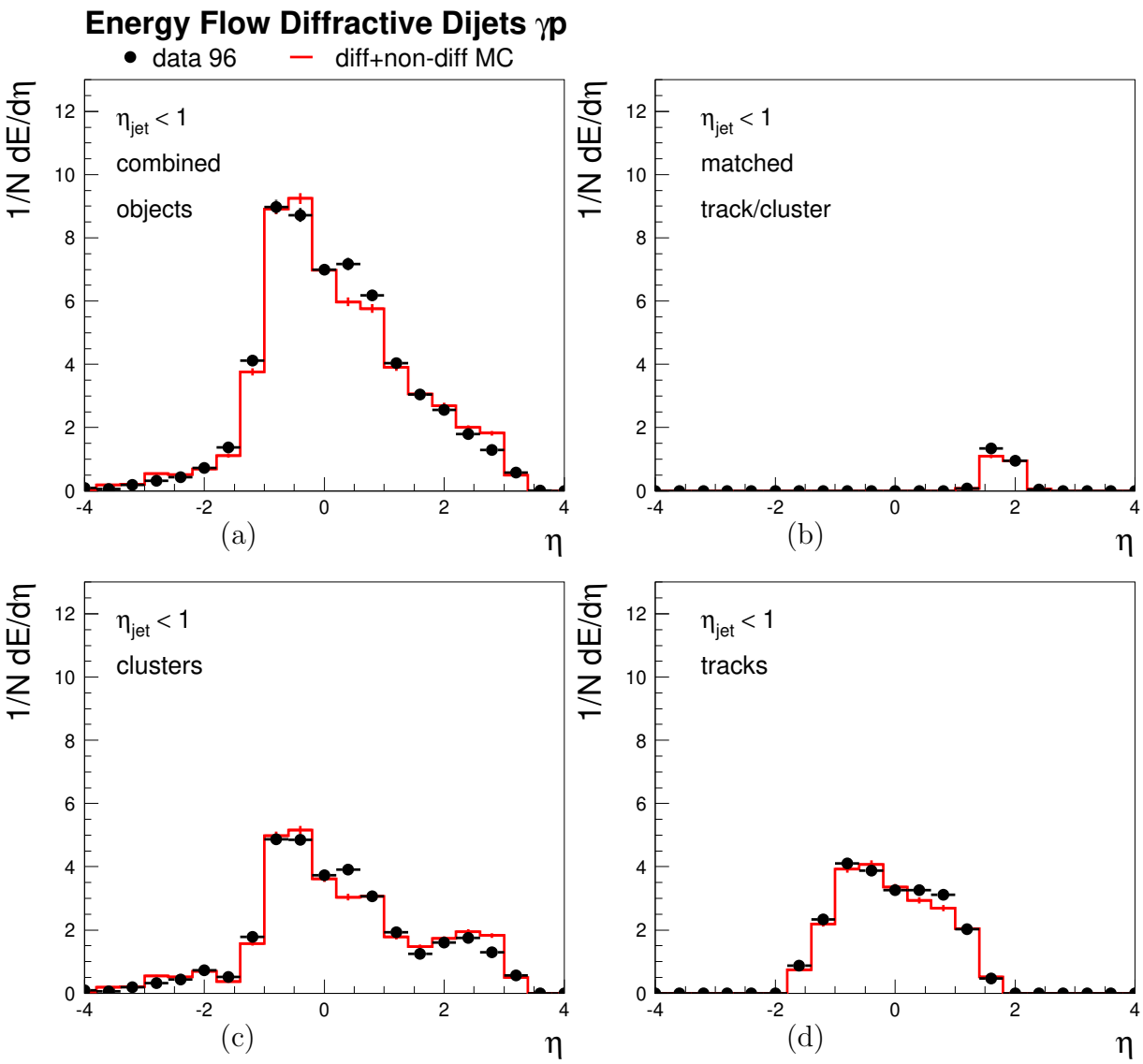

Fig. 5.16. Energy flow for the diffractive γp dijet sample in 96. Shown is the mean energy as a function of the pseudorapidity η in the laboratory frame. The energy is reconstructed from (a) combined track and calorimeter cluster information, (b) only matched tracks and clusters, (c) clusters, and (d) tracks. The jets are required to satisfy $\eta_{\text{jet}} < 1$.

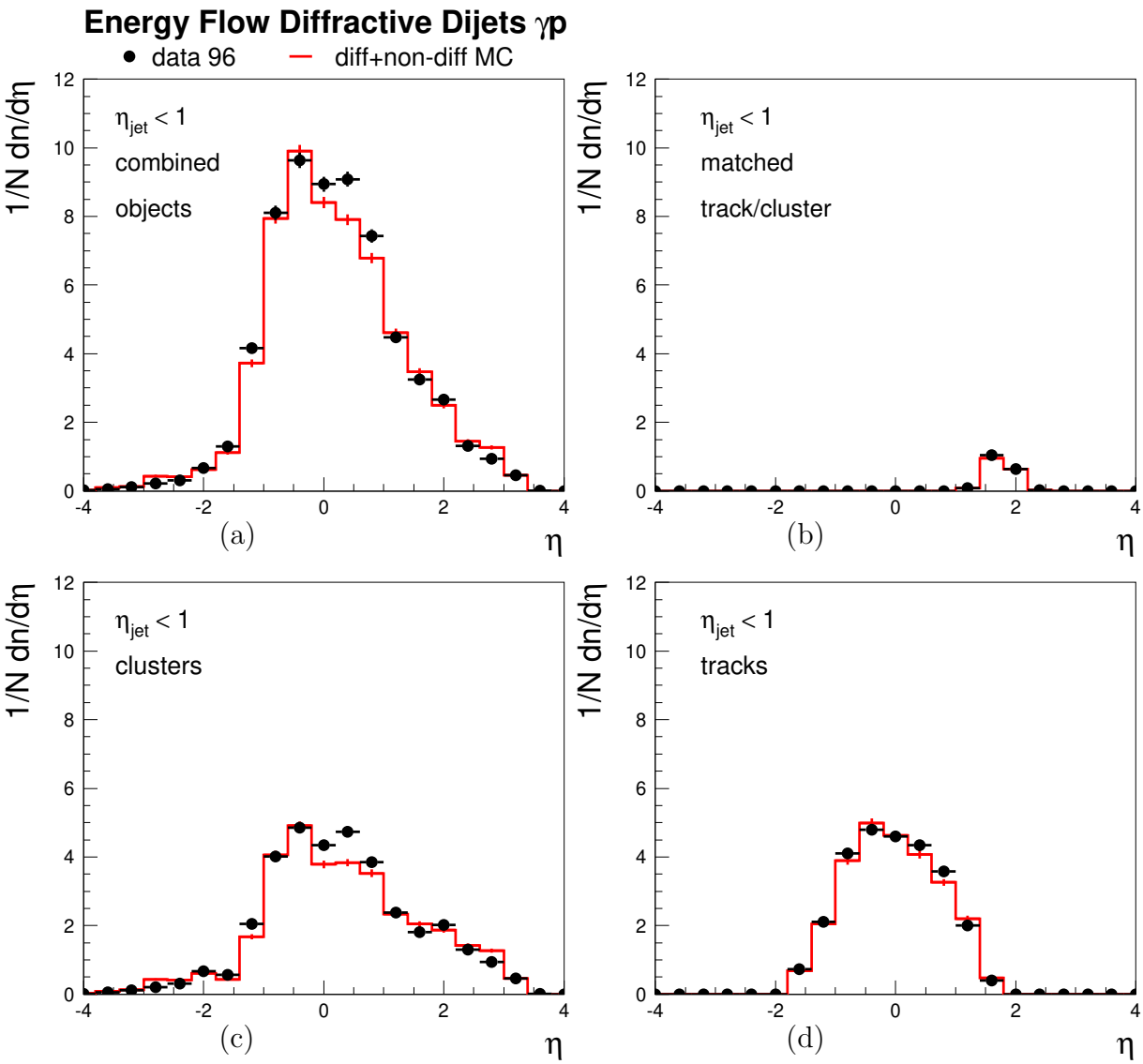

Fig. 5.17. Multiplicity for the diffractive γp dijet sample in 96. Shown are as a function of the pseudorapidity η in the laboratory frame the average numbers of (a) combined objects from tracks and calorimeter clusters, (b) matched tracks and clusters, (c) clusters, and (d) tracks. The jets are required to satisfy $\eta_{\text{jet}} < 1$.

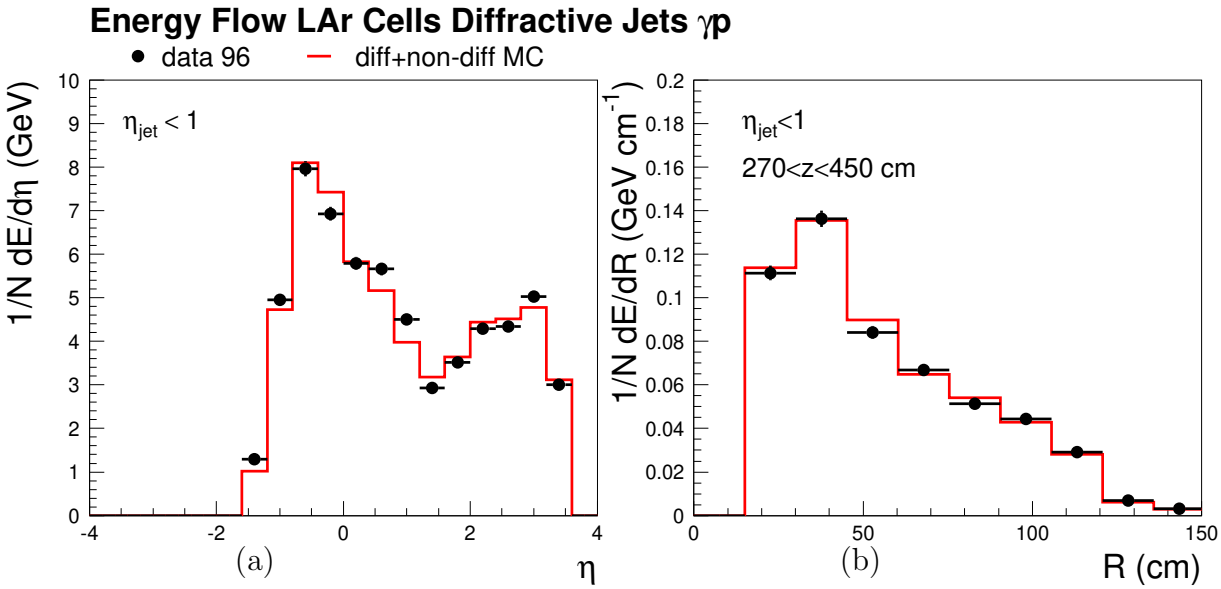

Fig. 5.18. Average LAr calorimeter cell energy in dijet events with $x_{I\!P} < 0.03$ and $\sum_{1:3}$ FMD < 2 for 96. The energy is shown as a function of (a) the pseudorapidity η in the laboratory frame, and (b) the radial distance R from the beam axis for the forward part of the LAr calorimeter ($270 < z < 450$ cm). The jets are required to satisfy $\eta_{\text{jet}} < 1$.

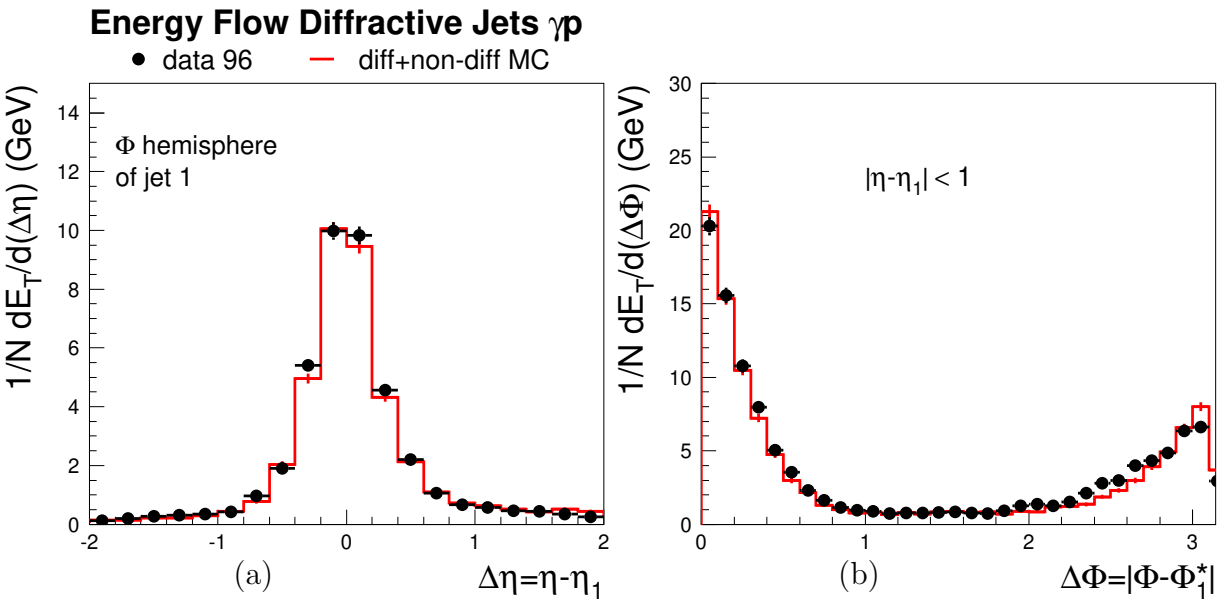

Fig. 5.19. Jet profiles for the diffractive dijet sample of 96 in the laboratory frame. Shown is the mean transverse energy per event around the leading jet as a function of (a) the pseudorapidity distance and (b) the distance in the azimuthal angle Φ with respect to the leading jet. For (a), only energy in the Φ hemisphere of the leading jet is taken into account. For (b), only energy within a pseudorapidity band $\eta \pm 1$ around the leading jet is considered.

5.5 Correction to the level of stable hadrons

This section describes the procedure of correcting the data for detector smearing.

5.5.1 Cross section formula

The cross section differential in the variable x is calculated according to

$$\frac{d\sigma}{dx} = \underbrace{\frac{N_{\text{data}}/\varepsilon_{\text{trig}} - N_{\text{non-diffr}}}{\varepsilon_{\text{etag}}\, C_{\text{det}}}\, C_{M_Y}}_{N_{\text{had}}}\; C_{\text{FMD}}\;\; \frac{1}{L\, dx} \tag{5.9}$$

with

N_{data} = number of data events,
$\varepsilon_{\text{trig}}$ = trigger efficiency,
$N_{\text{non-diffr}}$ = number of non-diffractive events,
$\varepsilon_{\text{etag}}$ = correction for electron detector inefficiency,
C_{det} = correction for detector effects,
C_{FMD} = correction for noise in the Forward Muon Detector,
C_{M_Y} = correction for migrations across $M_Y = 1.6$ GeV,
L = integrated luminosity,
dx = bin width.

The quantities C_{FMD}, C_{M_Y} and L are the same for every bin of the cross section. All other quantities are determined separately for every bin. The number N_{had} of corrected events at the hadron level is determined separately for 96 and 97. This procedure takes into account that the configuration of the detector can be different in both years. A combined cross section is then derived by adding the corrected event numbers and by dividing by the sum of the luminosities.

5.5.2 Correction factor, purity and stability

The data distributions are corrected for detector effects using a bin-to-bin correction method. The correction factor C_{det} is determined for every bin of the measured distributions using Monte Carlo events. The factor for bin i is given by the number of events in the detector level bin i divided by the number of events in the same bin at the hadron level.

For the bin-to-bin correction method to be applicable smearing across bin boundaries must not be too large. To quantify these migrations, the variables purity and stability are introduced. They should be as large as possible and are required to be at least 25%. It was shown in the previous section that the data distributions are well described by the Monte Carlo model. Remaining differences will be accounted for by assigning a systematic uncertainty to C_{det}. This is discussed in Sec. 5.6.

For the following definitions of the quantities purity and stability it is necessary to introduce some other quantities and nomenclature. Let sample `det` be the set of events

which fulfil all detector level cuts, and sample `had` be the set of events which fulfil the hadron level cuts defining the cross section (cf. Tab. 7.1). Sample `det`∩`had` is the intersection of both sets. Let $N^i_{\rm had}$(sample `had`) be the number of events in sample `had` for which the variable at the hadron level lies in bin i, and $N^i_{\rm det}$(sample `det`) be the number of events in sample `det` for which the variable is reconstructed in the detector level bin i. Finally, $N^i_{\rm det+had}$(sample `det`∩`had`) denotes the number of events which are in the same bin i at the hadron and the detector level for the events in the sample `det`∩`had`.

The correction factor $C^i_{\rm det}$ for bin i is given by the ratio of the numbers of events at the detector and the hadron level in that particular bin i:

$$C^i_{\rm det} = \frac{N^i_{\rm det}(\text{sample } \texttt{det})}{N^i_{\rm had}(\text{sample } \texttt{had})}$$

The correction factor is displayed in Fig. 5.20. This factor does not take into account the effect of the electron detector which is treated separately (factor $\varepsilon_{\rm etag}$ in (5.9)). The overall correction factor is around 0.75.

The variables purity and stability are defined to quantify the migrations.

$$\begin{aligned} \text{Purity } P_i &\equiv \text{fraction of detector level events} \\ &\quad \text{coming from the same hadron level bin} \\ &= \frac{N^i_{\rm det+had}(\text{sample } \texttt{det} \cap \texttt{had})}{N^i_{\rm det}(\text{sample } \texttt{det})} \end{aligned}$$

$$\begin{aligned} \text{Stability } S_i &\equiv \text{fraction of hadron level events} \\ &\quad \text{staying in the same bin when going to the detector level} \\ &= \frac{N^i_{\rm det+had}(\text{sample } \texttt{det} \cap \texttt{had})}{N^i_{\rm had}(\text{sample } \texttt{had})} \end{aligned}$$

The correction factor can be expressed as the ratio of stability and purity. The migrations into the detector level bin i are given by $1 - P_i$. The migrations out of the hadron level bin i are given by $1 - S_i$. Purity and stability are shown in Fig. 5.20 for the diffractive dijet sample of 97. The distributions for W are shown in Fig. 5.21. The bins have been chosen to ensure that both purity and stability are above 25%. The values for purity and stability (and therefore for the correction factor) are determined by the migrations due to detector smearing. The influence of the various cuts applied in the analysis is studied in detail in Sec. 5.5.3. The most important effect are the migrations across the jet p_T threshold.

5.5.3 Cut monitoring

The migrations across the various cut thresholds are studied with the diffractive Monte Carlo model. The diffractive MC consists of a pomeron and a reggeon component. Shown in Fig. 5.22 are the numbers for the pomeron component for 97. Starting with the full hadron sample (defined as sample `had` in Sec. 5.5.2), the cuts at the detector level are gradually switched on. This leads to event losses due to migrations out of the kinematic region of the cross section (cf. the filled area to the right of the cut line in Fig. 4.2).

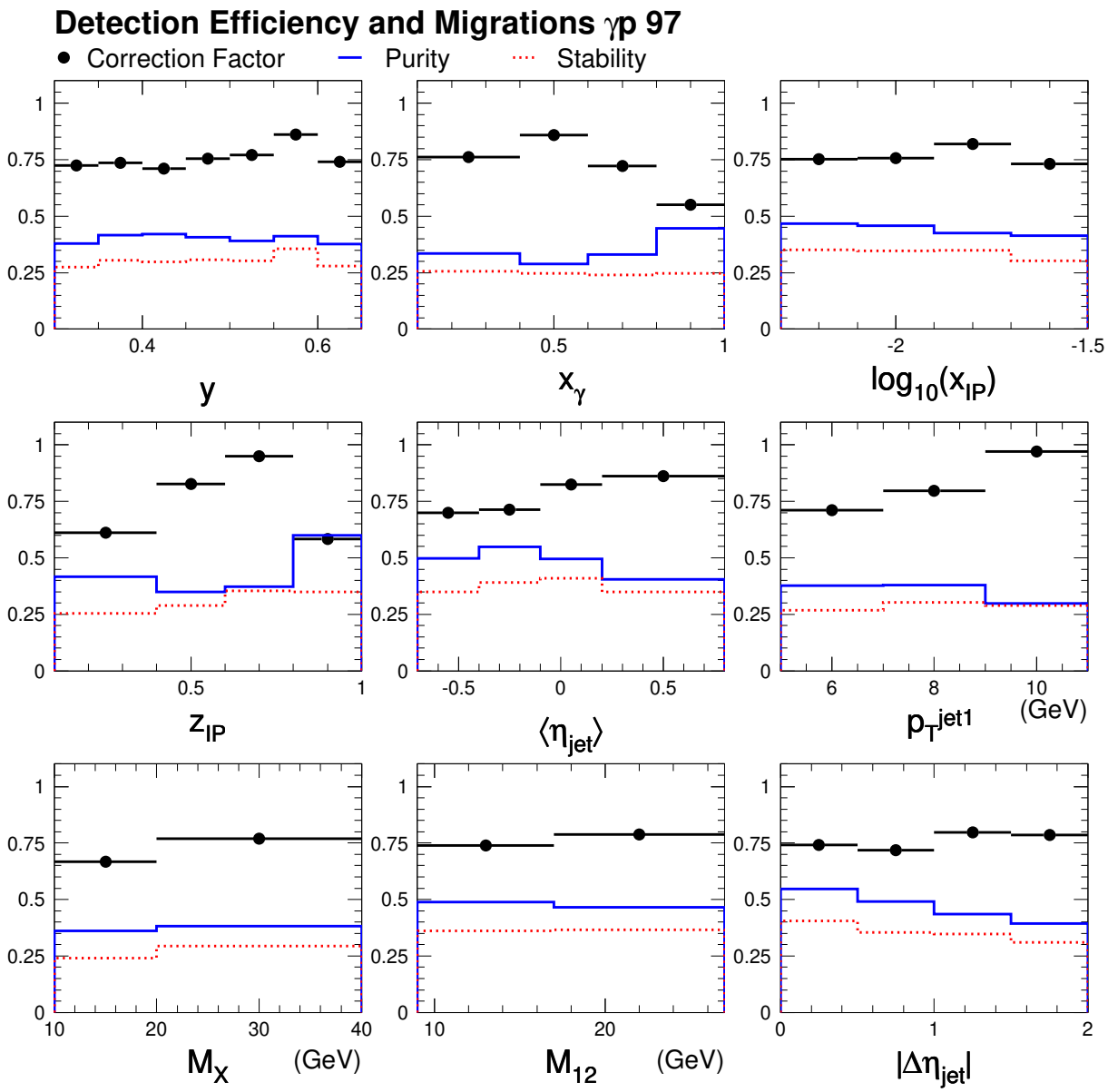

Fig. 5.20. Correction factor C_{det}, purity and stability evaluated with the diffractive photoproduction model for 97.

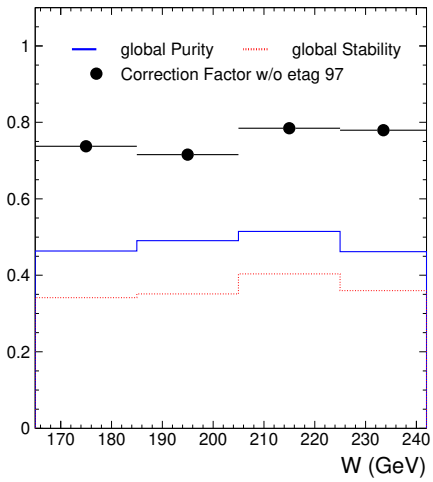

Fig. 5.21. Correction factor C_{det}, purity and stability for the spectrum of the variable W evaluated with the diffractive photoproduction model for 97.

When all detector cuts are applied, the cuts at the hadron level are gradually removed. This increases the number of events because of migrations into the detector sample from outside the cross section kinematic region (cf. the hatched area to the left of the cut line in Fig. 4.2). The mean efficiency of the electron detector as determined from the parameterisation is 42%. The average correction factor C_{det} is 0.75. This leads to an average combined correction factor of 0.32. Large amounts of migrations are seen across the p_T^{jet1} cuts that are applied at the detector and at the hadron level. They are due to the exponentially falling p_T dependence of the dijet cross section. For 42% of the events for which two jets have been identified at the hadron level according to the jet selection in Tab. 5.2 these dijet criteria are not met at the detector level. The same number is found for the migrations into the measurement region. For 42% of the events for which two jets have been measured in the detector, the corresponding jets at the hadron level do not fulfil the jet selection criteria. This implies that the overall purity and stability is limited to 58% by the migrations across the p_T threshold. The η_{max} spectrum is also exponentially falling in the region around the cut value 3.2 which results in the large amount of migrations due to finite detector resolution. The cuts on the forward activity reject approximately 17% of diffractive events. This inefficiency is discussed in Sec. 5.5.4.

Fig. 5.23 shows the numbers for the reggeon component. The contributions from reggeon exchange to the total sum of the diffractive events is 5% at the hadron level and 6.5% at the detector level. This indicates that the migrations into the measurement region are larger in the case of reggeon exchange. The main effect are the migrations across the $x_{I\!P}$ cut. This stems from the fact that $x_{I\!P}$ is reconstructed too small at the detector level for larger values of $x_{I\!P}$ (Fig. 5.1c). More losses are seen for the reggeon component due to the η_{max} cut because the hadronic system is located at larger rapidities than in processes mediated by pomeron exchange.

Cut monitoring pomeron 97

cut	N_event	reduction (%)
all hadron cuts	7107.7	---
+ electron in etagger	3052.0	57.1
+ pT_jet(1,2) > 5,4 GeV	1777.2	41.8
+ -1 < eta_jet(1,2) < 2	1719.3	3.3
+ cosmics	1678.4	2.4
+ primary vertex	1678.4	0.0
+ |zvtx|<35	1670.7	0.5
+ 165 < W < 242 GeV	1631.0	2.4
+ E_photon detector < 2 GeV	1615.7	0.9
+ x_pom < 0.03	1504.3	6.9
+ eta_max < 3.2	1360.4	9.6
+ FMD hit pairs < 2	1358.2	0.2
+ PRT hits = 0	1348.9	0.7

hadron cuts applied, detector cuts applied

cut	N_event	increase (%)
all hadron + detector cuts	1350.8	---
- -t < 1 GeV2	1351.5	0.0
- M_Y < 1.6 GeV	1351.8	0.0
- x_pom < 0.03	1514.5	12.0
- -3 < etaˆlab_jet < 0	1561.8	3.1
- pT*_jet(1,2) > 5,4 GeV	2215.2	41.8
- 165 < W < 242 GeV	2240.1	1.1
- 4 < Q2 < 80 GeV2	2240.1	0.0

Fig. 5.22. Cut monitoring for the diffractive Monte Carlo model in 97. The numbers refer to the pomeron component.

Cut monitoring reggeon 97

cut	N_event	reduction (%)
all hadron cuts	354.6	---
+ electron in etagger	151.0	57.4
+ pT_jet(1,2) > 5,4 GeV	86.0	43.1
+ -1 < eta_jet(1,2) < 2	85.7	0.3
+ cosmics	85.1	0.7
+ primary vertex	85.1	0.0
+ |zvtx|<35	85.1	0.0
+ 165 < W < 242 GeV	83.4	1.9
+ E_photon detector < 2 GeV	81.9	1.8
+ x_pom < 0.03	77.0	6.0
+ eta_max < 3.2	53.3	30.8
+ FMD hit pairs < 2	53.1	0.4
+ PRT hits = 0	52.7	0.6

hadron cuts applied, detector cuts applied

cut	N_event	increase (%)
all hadron + detector cuts	52.6	---
- -t < 1 GeV2	52.6	0.0
- M_Y < 1.6 GeV	56.1	6.7
- x_pom < 0.03	103.4	84.5
- -3 < eta^lab_jet < 0	106.9	3.4
- pT*_jet(1,2) > 5,4 GeV	155.9	45.8
- 165 < W < 242 GeV	156.6	0.4
- 4 < Q2 < 80 GeV2	156.6	0.0

Fig. 5.23. Cut monitoring for the diffractive Monte Carlo model in 97. The numbers refer to the reggeon component.

5.5.4 Inefficiency of the rapidity gap selection

It was shown in the cut monitoring tables, that the cuts which require a rapidity gap reject diffractive events. The cuts on $x_{I\!P}$, $\eta_{\max}$ and the forward muon and PRT detectors reject approximately 17% of the pomeron exchange events. These diffractive events have activity in the forward region. In the pomeron model used for the MC predictions this energy is due to the pomeron remnant and due to protons being scattered into the PRT at larger values of $|t|$. The inefficiency of the forward gap selection is covered in C_{det} and is corrected with the RAPGAP pomeron model. The energy flow in the forward direction of diffractive events has been studied in [41] with events for which an elastically scattered proton is detected in a dedicated forward proton detector. The requirement of an elastic proton efficiently rejects non-diffractive background. In this analysis, it was found that the distributions of the energy flow in the forward direction and also the hits in the FMD and the PRT for the elastic proton events are well described by the pomeron model. The event distributions were studied with and without gap selection cuts applied. From the comparison of the distributions before and after the application of the gap selection cuts, a correction factor for the gap selection can be evaluated. This was done for the distributions of the data and those of the Monte Carlo model for hard scattering events which are dominated by pomeron exchange. It was found that the correction factor of the data is described within 30% by the correction calculated from the Monte Carlo model, limited by the statistical accuracy of the data.

This 30% uncertainty is taken as the systematic error on the gap selection in the present analysis. This results in an additional systematic error of 5% on the cross section.

5.5.5 Correction for noise in the FMD

It was explained in Sec. 5.3.9.3 that FMD noise is not included in the simulation of the H1 detector and therefore not included in the diffractive MC model used for the calculation of C_{det}. To very good approximation, the effect of the noise is given by an overall normalisation factor C_{FMD} which increases the cross section (cf. (5.9)). The factor is given by unity plus the fraction π of noise as defined in Sec. 5.3.9.3:

$$C_{\mathrm{FMD}} = 1.055 \pm 0.014 \text{ (syst.)}.$$

5.5.6 Correction for proton dissociation

Due to the geometrical detector acceptance in the direction of the outgoing proton system it is not possible to efficiently detect a break-up of the proton into a low mass system Y. The detection efficiency was studied in [38]. The results obtained there are used for the present analysis and will be discussed in the following. The result is that the cross sections have to be corrected to the range $M_Y < 1.6$ GeV and $-t < 1$ GeV^2.

Fig. 5.24 shows the rejection efficiency of the diffractive cuts explained in Sec. 5.3.9. It is shown as a function of (a) M_Y and (b) t for proton dissociation events. From (a) it can be seen that the rejective power is bad for small masses M_Y. For $M_Y = 1.6$ GeV the efficiency reaches $\approx 60\%$. The cross section will be corrected to $M_Y < 1.6$ GeV.

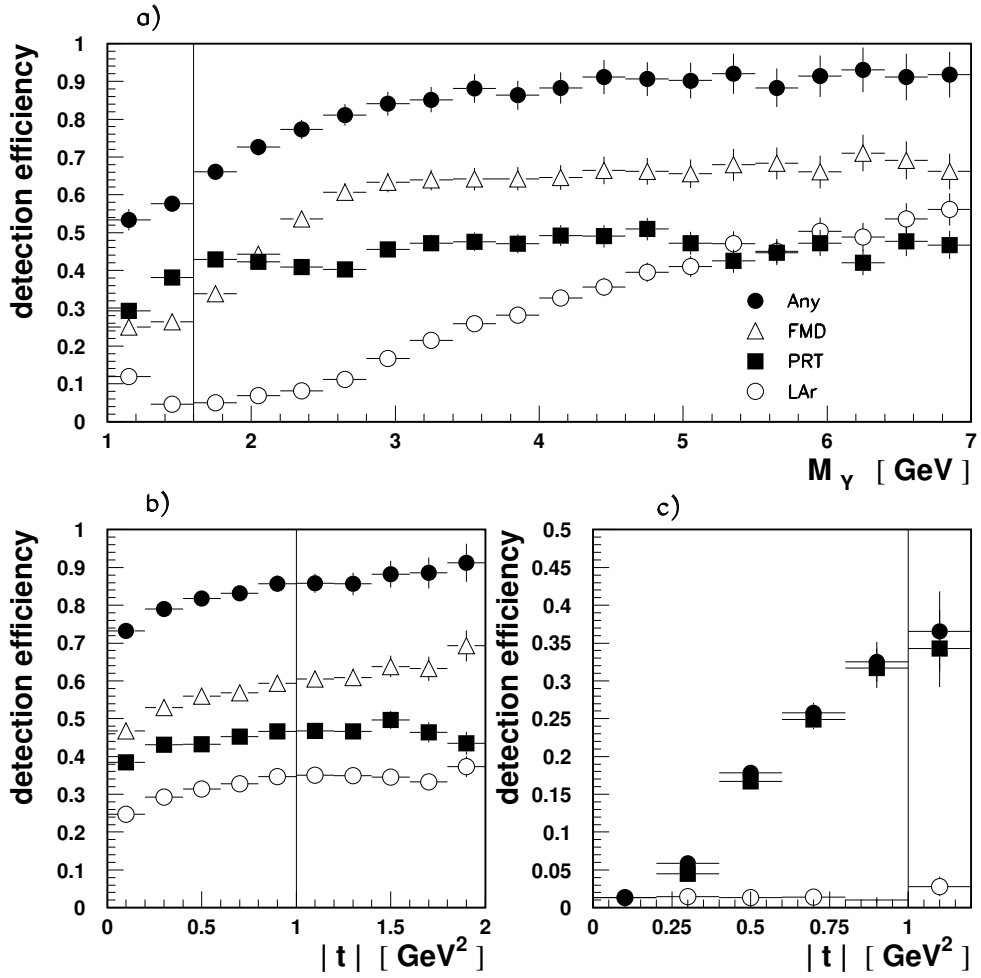

Fig. 5.24. The efficiency of the diffractive cuts explained in Sec. 5.3.9 for rejecting proton dissociation events as function of (a) M_Y and (b) $|t|$, and (c) for rejecting elastically scattered protons as a function of $|t|$. The figure is taken from [38].

The efficiency is displayed in (b) as a function of $|t|$. It rises with $|t|$ and has reached a plateau for $|t| = 1.0$ GeV^2 which is the limit for the cross sections presented here. At this value, the efficiency for rejecting elastically scattered protons has exceeded 30% as can be seen from (c). These protons get scattered into the PRT. It is not possible to detect elastic protons efficiently at lower values of $|t|$. Therefore, the cross sections presented in this analysis are integrated over $0 < -t < 1$ GeV^2.

In the diffractive RAPGAP model, which is used to determine C_{det}, the proton is always scattered elastically. Proton dissociation is not included. The migrations across $M_Y = 1.6$ GeV have been evaluated with the Monte Carlo program DIFFVM and are taken into account by an extra factor C_{M_Y} in the cross section formula (5.9). The factor itself was not calculated in the present analysis but is taken from [38]. It is defined as the ratio of proton elastic and dissociative events generated inside the kinematic range ($M_Y < 1.6$ GeV, $|t| < 1.0$ GeV^2) to the net number of migrations out of this region.[1] The values obtained are

$$C_{M_Y} = 0.96 \pm 0.04 \text{ (syst.)} \quad \text{for 96;} \quad C_{M_Y} = 0.924 \pm 0.05 \text{ (syst.)} \quad \text{for 97.}$$

The difference between the year 96 and 97 is due to the degrading performance of the PRT. The systematic uncertainty of the factor is determined by varying

- the ratio of proton elastic to dissociative cross sections,
- the shape of the generated M_Y distribution,
- the shape of the generated t spectrum,
- the efficiency of the forward detectors.

Details can be found in [38]. The correction for smearing over $-t = 1.0$ GeV^2 for elastic protons is covered by C_{det}.

5.6 Systematic uncertainties

The extracted cross section depends on various parameters. They can be divided into two categories. The first is related to the insufficient understanding of the detector parameters, such as the energy scale of the calorimeter. The uncertainties in the second category arise from the imperfect modelling of the data distribution by the Monte Carlo events which are used to correct detector smearing.

To evaluate the cross section uncertainty related to a certain parameter, the parameter is varied within its uncertainty. The resulting change in the cross section is then taken as the associated systematic uncertainty of the cross section.

1. Net number of migrations out = migrations out - migrations in.

5.6.1 Incomplete understanding of detector parameters

The following sources of systematic uncertainties related to incomplete detector understanding are considered.

- **Hadronic LAr energy scale**
  The energy scale of the hadronic part of the LAr calorimeter has been varied by ±4%. This leads to changes of the total cross section of 8%.

- **Hadronic SPACAL energy scale**
  The energy scale of the hadronic part of the SPACAL is known within 7%. This gives rise to a variation of the cross section below one percent.

- **Track momenta in combined objects**
  A 3% uncertainty of the contribution of track momenta to the combined objects results in cross section errors of approximately 4%.

- **Electron detector efficiency**
  The electron detector acceptance and efficiency parameterisation is known within 1.5%. This leads to uncertainties in the cross section of below one percent.

- **Luminosity measurement**
  The luminosity measurement is accurate within 2%. This translates directly into an error on the cross section of 2%.

- **Trigger efficiency parameterisation**
  As was shown in Sec. 5.3.2, the parameterisation of the trigger efficiency can describe the efficiency within 5%. This gives rise to an uncertainty of the cross section of 5 to 6%.

The errors on the energy scale, the track momenta and electron detector are evaluated with the diffractive Monte Carlo model. They affect the calculation of the correction factor C_{det}. The error of C_{det} translates directly into an error of the cross section (cf. (5.9)).

5.6.2 Imperfect description of data distributions

The following uncertainties result from the imperfect Monte Carlo modelling of the data distributions.

- **Inefficiency of the rapidity gap selection**
  A 30% uncertainty is assumed for the RAPGAP correction of the rapidity gap inefficiency. This value translates into a 5% systematic uncertainty on the cross section.

- **Number of migrations from $\mathbf{x_{I\!P}^{had} > 0.05}$**
  The amount of migrations from large $x_{I\!P}$ is determined by the normalisation of the non-diffractive Monte Carlo model as explained in detail in Sec. 5.2. The normalisation of the model is varied by ±50% leading to cross section changes of 2%. The

largest influence (3%) is seen in the highest $x_{I\!P}$ bin where the non-diffractive model contributes most.

- **Shapes of Monte Carlo spectra**
  Any difference between the data and Monte Carlo event variable spectra at the detector level implies that the correction factor C_{det}, which is determined from the model, does not correctly describe the migrations. To evaluate the uncertainty of C_{det}, the shapes of the following Monte Carlo distributions are varied within the statistical errors of the data distributions:
  - $z_{I\!P}$ by ${z_{I\!P}}^{\pm 0.3}$ and $(1 - z_{I\!P})^{\pm 0.3}$
  - $\hat{p}_T$ by $\hat{p}_T^{\pm 0.5}$
  - $x_{I\!P}$ by ${x_{I\!P}}^{\pm 0.2}$
  - t by $e^{\pm 2t}$
  - x_γ by ${x_\gamma}^{\pm 0.3}$ and $(1 - x_\gamma)^{\pm 0.3}$
  - y by $y^{\pm 0.5}$ and $(1 - y)^{\pm 0.5}$

  This reweighting gives rise to cross section errors in the range of a few percent. The largest deviation (4%) is due to the $\hat{p}_T$ reweight. This reweight is applied because of the large number of migrations across the jet p_T threshold. The imperfect knowledge of the p_T spectrum only affects the measurement at the level of 4% despite the large amount of migrations. The influence of the $\hat{p}_T$ reweighting on the various variables is shown in Fig. 5.25. The reweighting in ${z_{I\!P}}^{\pm 0.3}$ is shown in Fig. 5.26. It can be seen that $z_{I\!P}$ is correlated with $x_{I\!P}$ (according to (2.7)). The other variables are almost unaffected by the reweight in $z_{I\!P}$.

- **Migrations across $\mathbf{M_Y = 1.6}$ GeV**
  The 7% uncertainty of the correction factor C_{M_Y} translates directly into a 7% systematic error for the cross section.

- **FMD noise correction**
  The uncertainty in the determination of the noise fraction π for the FMD (25%) translates into a 1.3% error for C_{FMD} which is also the uncertainty for the cross section.

The dominant uncertainty on the cross section results from the uncertainty in the calibration of the LAr hadronic energy and the correction for migrations across $M_Y = 1.6$ GeV. The precision of the measurement is systematically limited. The total systematic uncertainty is approximately 14%. The statistical uncertainty of the measurement is $\approx 5\%$.

5.7 Summary

In this chapter, the analysis of dijet events in diffractive photoproduction was presented. It was shown that the rate at which these events are measured is stable over the run periods considered in the analysis when the trigger inefficiency is taken into account.

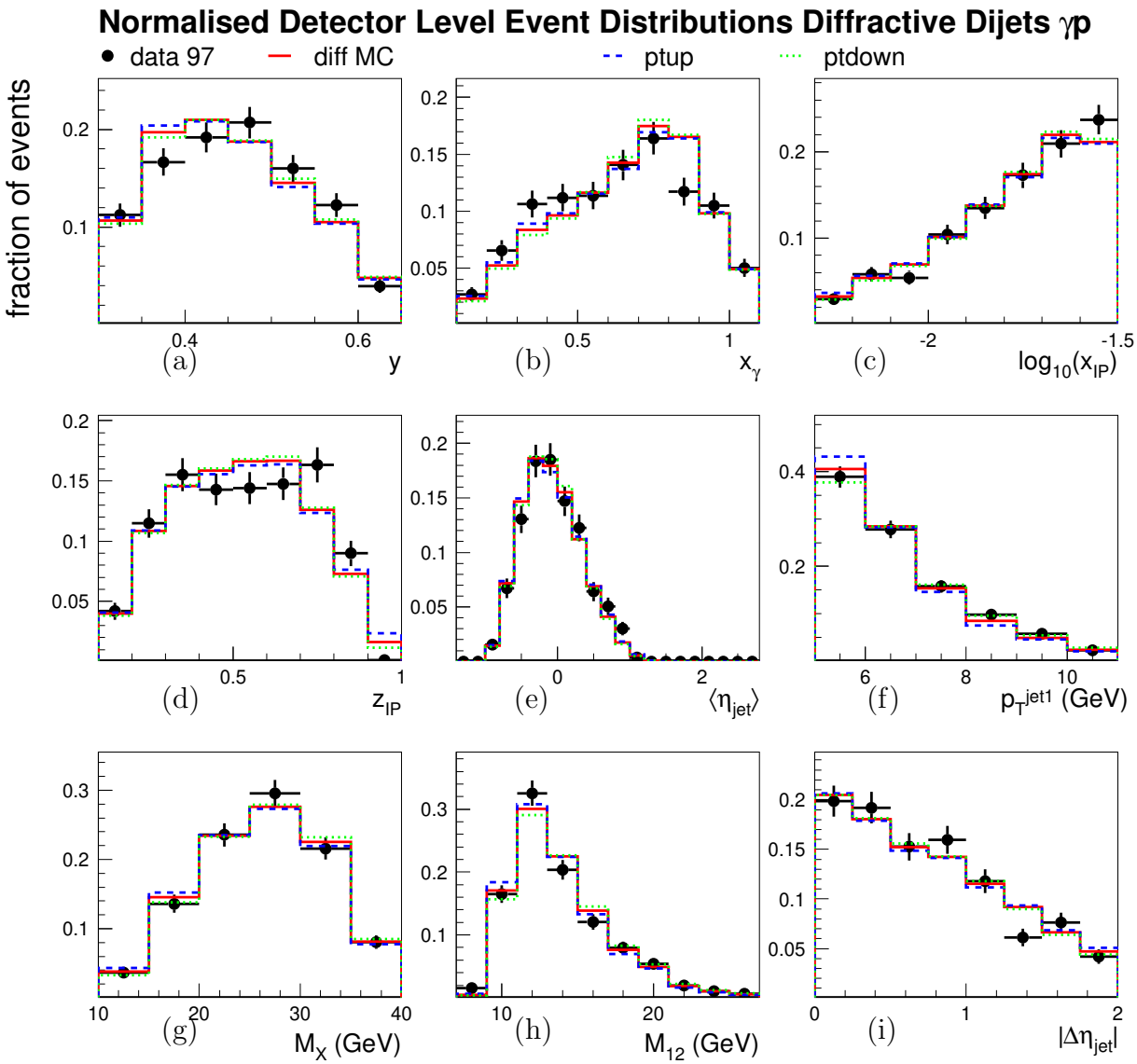

Fig. 5.25. Normalised diffractive dijet distributions in photoproduction for 97. The diffractive Monte Carlo model is also shown reweighted by $\hat{p}_T^{-0.5}$ (labelled 'ptup') and $\hat{p}_T^{0.5}$ ('ptdown').

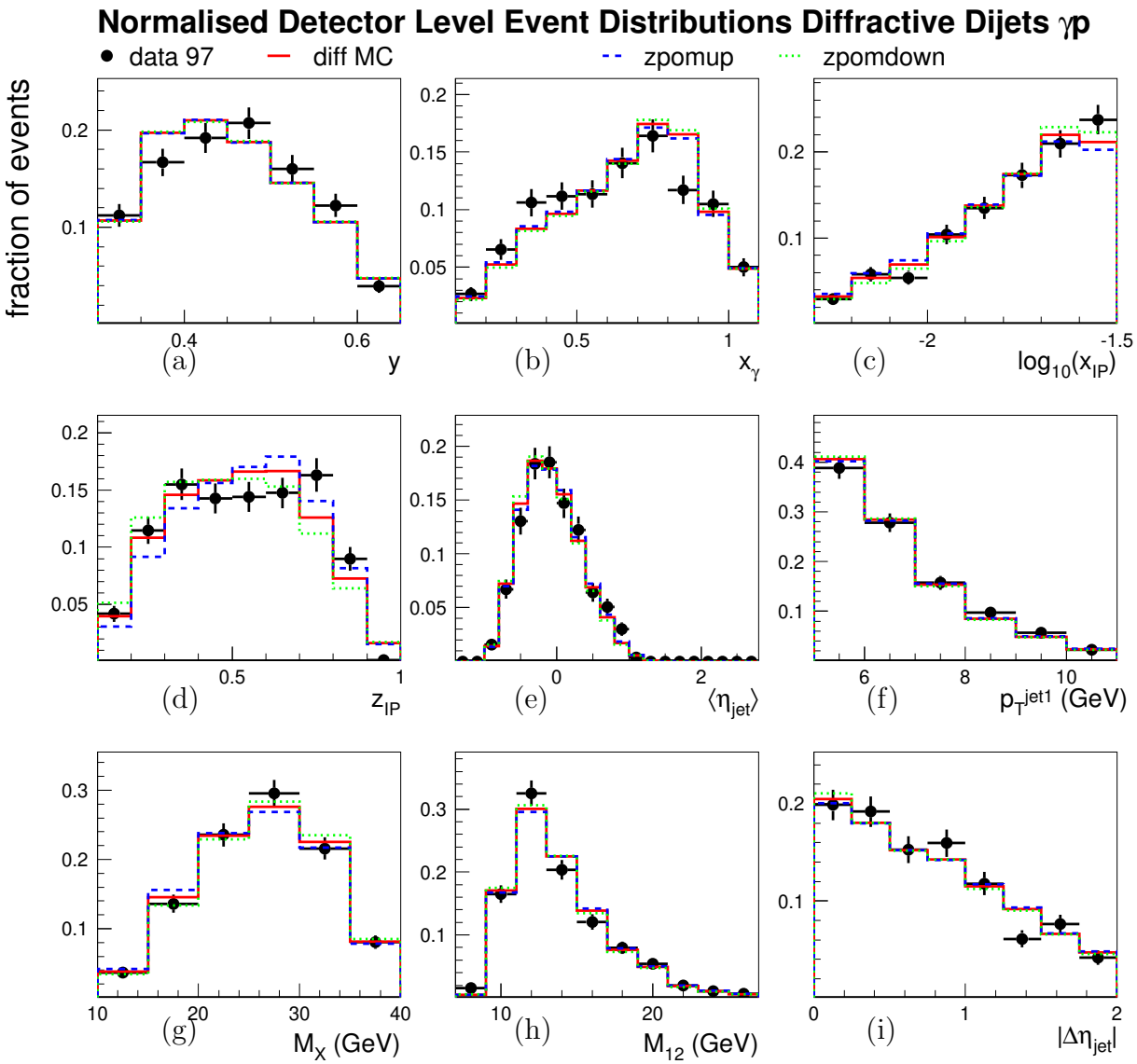

Fig. 5.26. Normalised diffractive dijet distributions in photoproduction for 97. The diffractive Monte Carlo model is also shown reweighted by $z_{I\!P}{}^{0.3}$ (labelled 'zpomup') and $z_{I\!P}{}^{-0.3}$ ('zpomdown').

Quantity	**96**	**97**	$\frac{97-96}{97}$	**Comment**
L (pb^{-1})	7.02	10.74		
N_{raw}	537	828		
L1 prescale	1.03	1.01		
$N_{\mathrm{data}} \equiv N_{\mathrm{raw}} \times$L1 prescale	551	835		
$\varepsilon_{\mathrm{trig}}$	0.84	0.94	0.101	
$N_{\mathrm{non-diffr}}$	14.28	36.39		
$\frac{N_{\mathrm{non-diffr}}}{N_{\mathrm{data}}/\varepsilon_{\mathrm{trig}}}$	0.022	0.041		
$\varepsilon_{\mathrm{etag}}$	0.50	0.43	-0.157	higher trigger threshold in 97, different e beam optics
C_{det}	0.75	0.75	-0.001	
C_{M_Y}	0.96	0.924	-0.039	degrading PRT efficiency
C_{FMD}	1.055	1.055		
N_{data}/L (pb)	78.49	77.75	-0.010	
$N_{\mathrm{data}}/(\varepsilon_{\mathrm{trig}}\, L)$ (pb)	93.03	82.85	-0.123	
$\frac{N_{\mathrm{data}}/\varepsilon_{\mathrm{trig}} - N_{\mathrm{non-diffr}}}{L}$ (pb)	90.99	79.46	-0.145	
$\frac{N_{\mathrm{data}}/\varepsilon_{\mathrm{trig}} - N_{\mathrm{non-diffr}}}{\varepsilon_{\mathrm{etag}}\, L}$ (pb)	183.59	185.45	0.010	
$\frac{N_{\mathrm{data}}/\varepsilon_{\mathrm{trig}} - N_{\mathrm{non-diffr}}}{\varepsilon_{\mathrm{etag}}\, C_{\mathrm{det}}\, L}$ (pb)	244.67	247.41	0.011	
$\frac{N_{\mathrm{data}}/\varepsilon_{\mathrm{trig}} - N_{\mathrm{non-diffr}}}{\varepsilon_{\mathrm{etag}}\, C_{\mathrm{det}}\, L}\, C_{M_Y}$ (pb)	234.88	228.61	-0.027	
$\frac{N_{\mathrm{data}}/\varepsilon_{\mathrm{trig}} - N_{\mathrm{non-diffr}}}{\varepsilon_{\mathrm{etag}}\, C_{\mathrm{det}}\, L}\, C_{M_Y}\, C_{\mathrm{FMD}}$ (pb)	247.80	241.18	-0.027	

Tab. 5.4. Average event numbers and correction factors for the photoproduction analysis. The numbers in the last line correspond to the total diffractive dijet cross section.

It was shown that the shapes of the event variable distributions can be described by LO Monte Carlo events which are based on diffractive parton densities as obtained in inclusive diffractive DIS. The energy flow per event is well described by the Monte Carlo model. A correction factor to the level of stable hadrons has been determined from the Monte Carlo event distributions. The largest migrations were seen to be due to the jet threshold p_T cut. The resulting cross sections are shown in Chap. 7 where they are compared with model predictions. The average event numbers and correction factors are listed in Tab. 5.4. The analysis was performed separately for 96 and 97 to check the consistency between the results obtained in the different years. The total cross sections for 96 and 97 agree within 3% which is smaller than the statistical and systematic uncertainties of the measurements.

Chapter 6

Analysis of dijets in diffractive DIS

This chapter describes the measurement of dijet cross sections in diffractive DIS. The aim is to obtain a measurement in the same kinematic region (apart from Q^2) and with the same jet algorithm as in photoproduction. Several detector related aspects, such as the treatment of noise in the FMD or the correction for smearing across $M_Y = 1.6$ GeV, are the same in both analyses. In such cases, cross references will be given to the related section in the previous chapter.

The text is organised as follows. A sample of dijet events in standard DIS is selected. The data are modelled using a combination of diffractive and non-diffractive DIS Monte Carlo events. Non-diffractive events which have migrated into the selected region of the phase space due to detector smearing are statistically subtracted. The inclusive dijet sample is used to study the diffractive cut variables. It is shown that the diffractive dijet data distributions are described by the Monte Carlo events. A correction factor is calculated from the Monte Carlo events to correct the distributions of the data for detector smearing. Systematic uncertainties of the cross section extraction are discussed. The results are presented and discussed in Chap. 7.

6.1 Reconstruction of kinematic variables

This section discusses the reconstruction of the kinematic variables at the detector and the hadron level. The correlations between the quantities as defined at the different levels (parton, hadron, and detector) are examined using the diffractive Monte Carlo model introduced in Sec. 6.2. Fig. 6.1 shows the correlations between the kinematic variables as reconstructed at the hadron and the detector level. The difference between the variable at the hadron and at the detector level is shown in Fig. 6.2. This difference is effectively the projection along the diagonals indicated in Fig. 6.1. Fig. 6.3 shows the correlations

between the variables at the parton level and reconstructed at the hadron level. The difference between the parton and the hadron level variables is shown in Fig. 6.4.

The scattered electron is measured in the SPACAL calorimeter. From the polar electron scattering angle θ_e and the measured electron energy E'_e, the kinematic variables y is reconstructed according to

$$y = 1 - \frac{E'_e}{E_e} \sin^2(\frac{\theta_e}{2}),$$

in which E_e is the energy of the incoming electron. This energy can be different from the electron beam energy in the case of initial state photon radiation. The true parton level variable is also used at the hadron level. Shown in Fig. 6.2a is the difference between y at the detector level and the hadron level y. The variables are well correlated with a resolution of 0.016.

The photon virtuality Q^2 is reconstructed at the detector level as

$$Q^2 = 4\, E'_e\, E_e\, \cos^2(\frac{\theta_e}{2}).$$

The parton level Q^2 is also used at the hadron level. The resolution at the detector level is 0.3 GeV^2 (Fig. 6.2b).

The photon-proton centre-of-mass energy W is reconstructed according to

$$W^2 = y\, s - Q^2.$$

The parton level W is used at the hadron level. The resolution at the detector level is 3.4 GeV (Fig. 6.5a).

The hadronic system X, containing the jets, is measured in the LAr and the SPACAL calorimeter and the central tracking system. Calorimeter cluster energies and track momenta are combined as explained in Sec. 5.3.7. The invariant mass of the hadronic system M_X is reconstructed according to

$$M_X^{\mathrm{had}} = \sqrt{p_X^2} \tag{6.1}$$

at both the hadron and the detector level. The difference between the variable reconstructed at these levels is displayed in Fig. 6.2g where only the range $10 < M_X < 40$ GeV is taken into account. It is described by a Gaussian distribution of width 3.0 GeV and is centred at -0.3 GeV. No diffractive cuts are applied in Fig. 5.1g to extend the range to larger masses. It can be seen that the reconstructed mass is too small for $M_X > 35$ GeV because the hadronic system is no longer fully contained within the LAr calorimeter for these large masses. This affects mainly the migrations observed in reggeon exchange processes. A different reconstruction method was tried by shifting the detector level M_X onto the diagonal. However, the resolution became very coarse. The reconstruction was therefore not changed although the contribution of reggeon processes is approximately 10% at the detector level, At the parton level, M_X is given by (2.1.1). The hadron level quantity is very well correlated with this value. The resolution at the hadron level is 0.03 GeV (Fig. 6.4g).

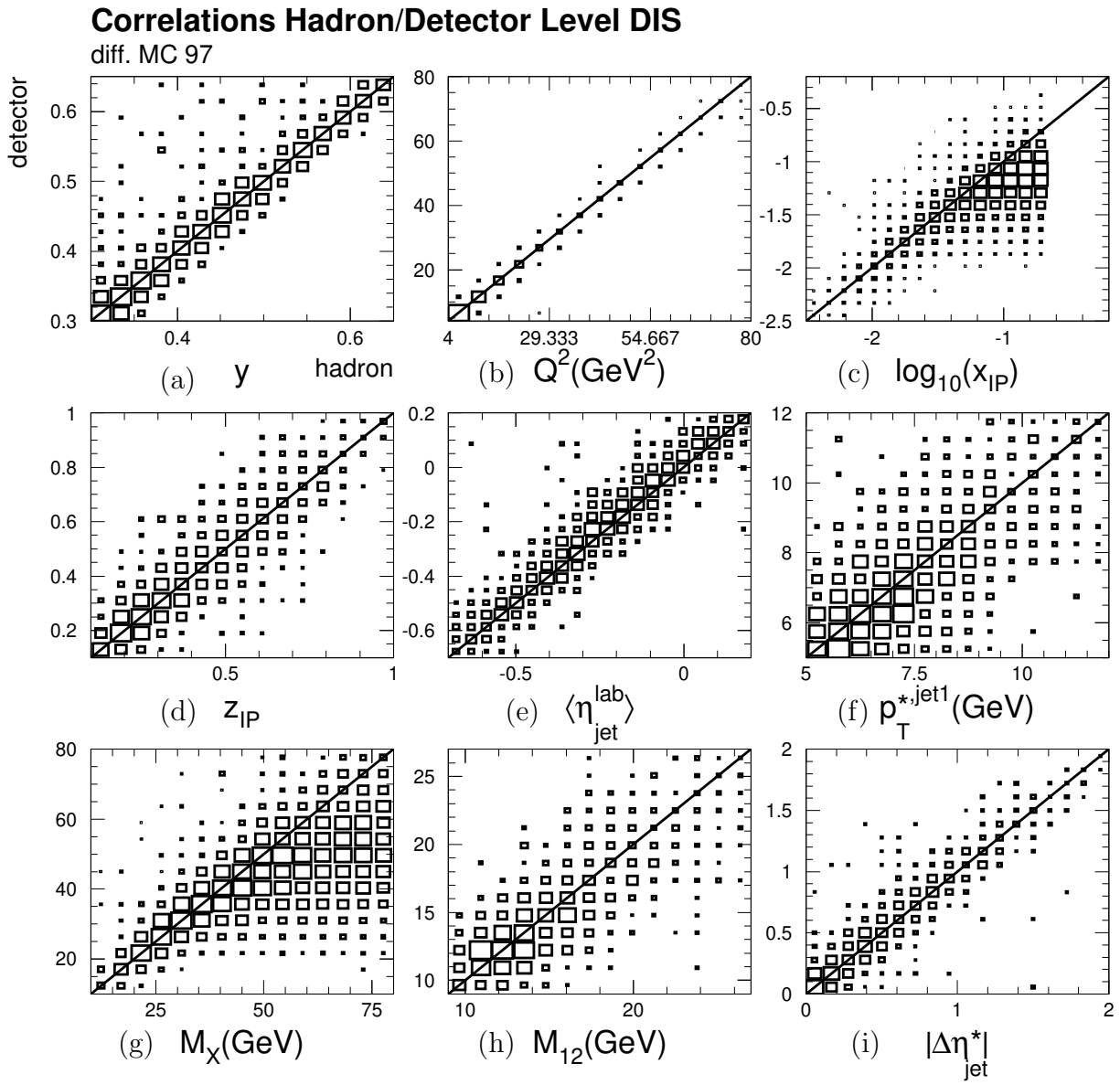

Fig. 6.1. Correlations between the variable reconstructed at the hadron level (horizontal axis) and the detector level (vertical axis). The correlations are evaluated with the diffractive MC for 97. All final selection cuts are applied at the detector level and the hadron level except for the distributions of $\log x_{I\!P}$ and M_X for which no diffractive cuts are applied to extend the populated range.

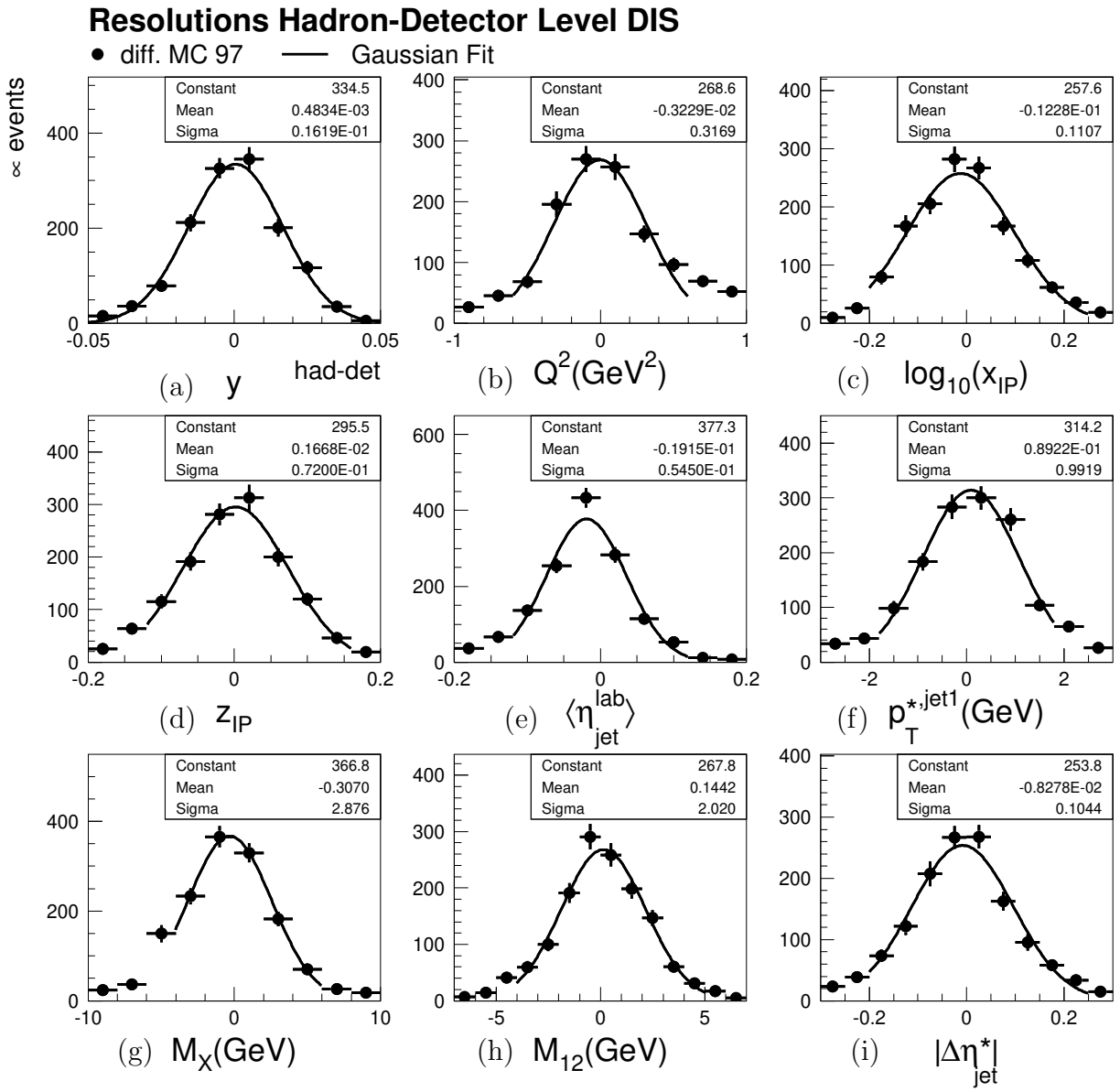

Fig. 6.2. Resolutions for reconstructing the hadron level quantity at the detector level. Shown is the difference between the variable reconstructed at the hadron level and at the detector level. The resolutions are evaluated with the diffractive MC for 97.

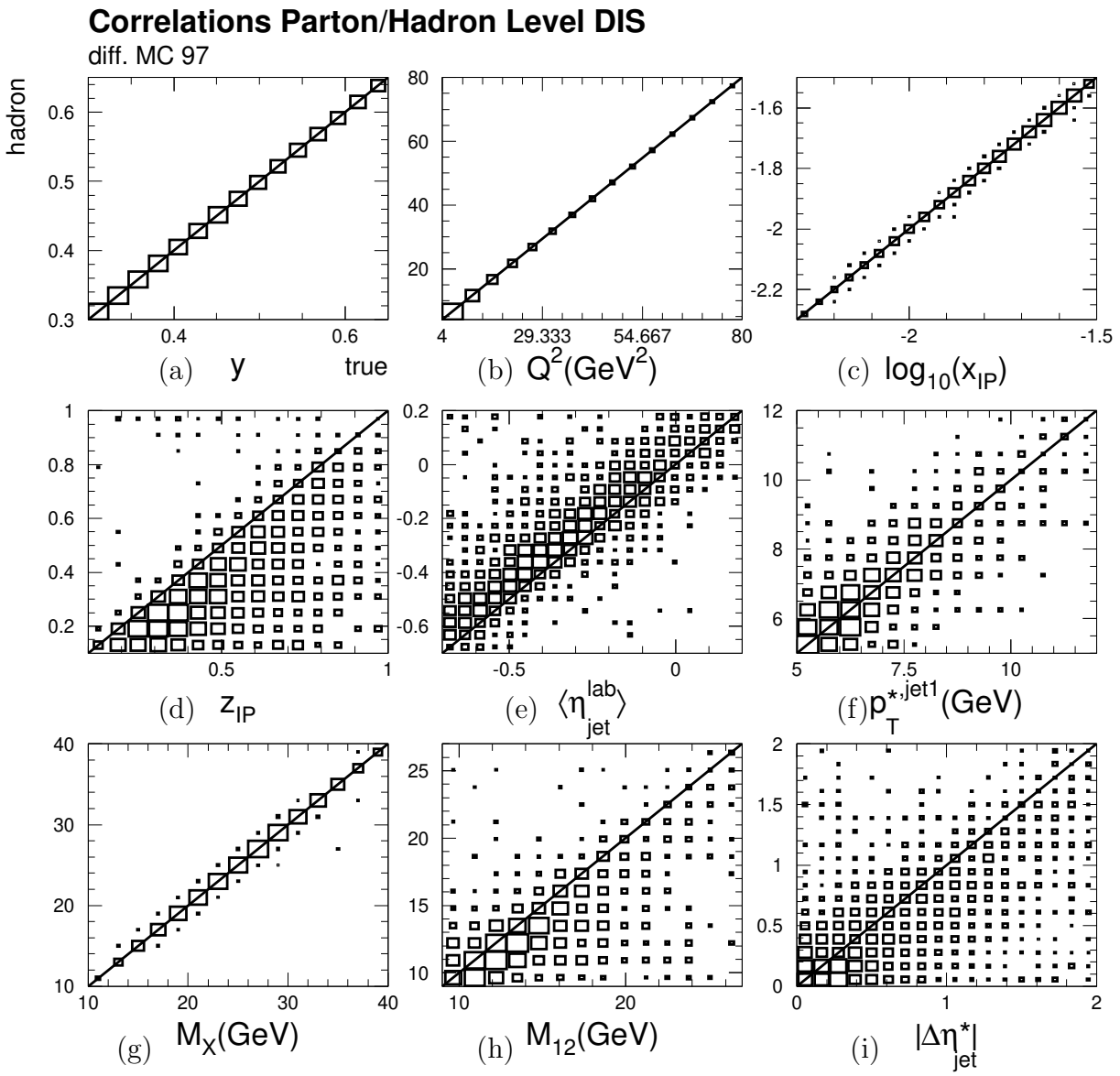

Fig. 6.3. Correlations between the variable at the parton level (horizontal axis) and reconstructed at the hadron level (vertical axis). The correlations are evaluated with the diffractive MC for 97.

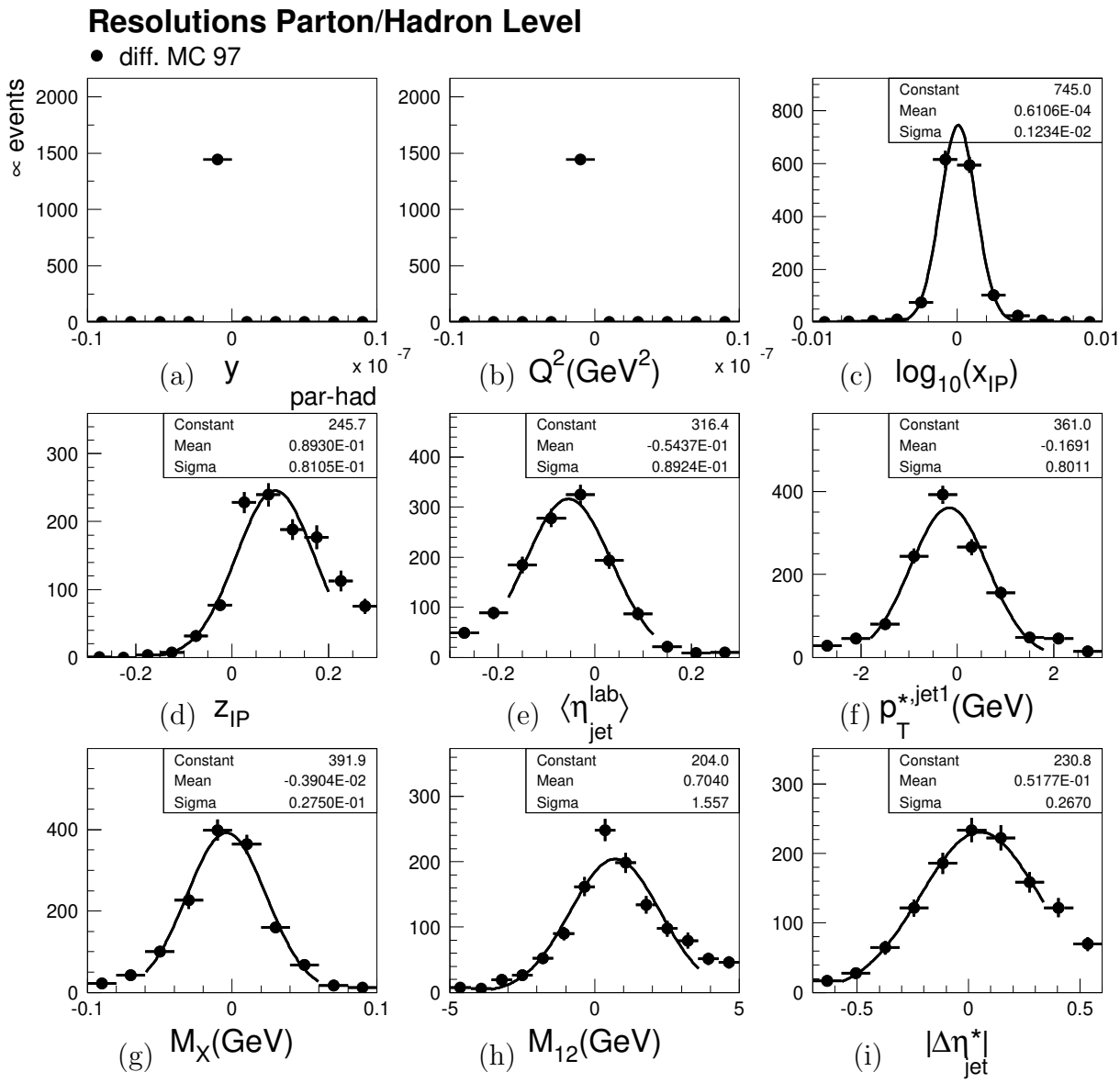

Fig. 6.4. Resolutions for reconstructing the parton level quantity at the hadron level. Shown is the difference between the variable as defined at the parton level and the variable reconstructed at the hadron level. The resolutions are evaluated with the diffractive MC for 97.

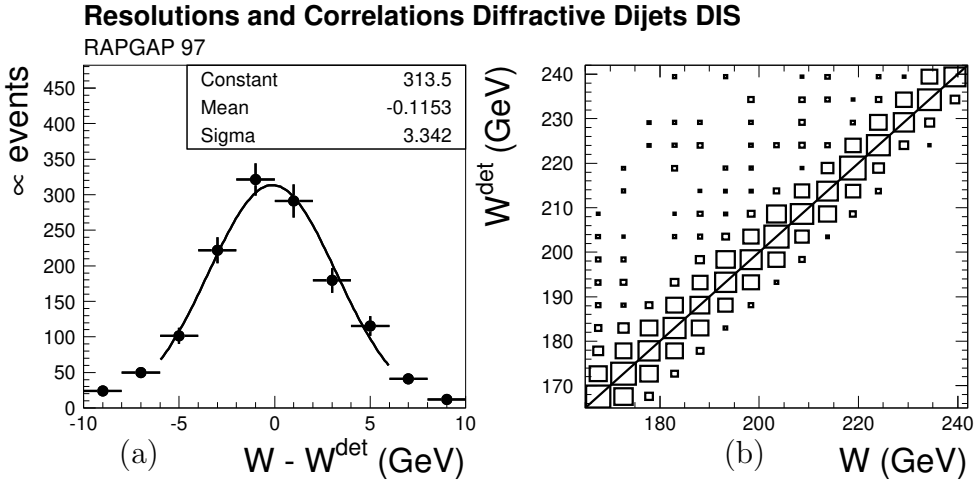

Fig. 6.5. Correlations for W evaluated with the diffractive model for 97. (a) The difference between the value reconstructed at the hadron level and the detector level. (b) The correlation between the hadron level W (horizontal axis) and the detector level W (vertical axis).

The fractional proton momentum $x_{I\!P}$ transferred to the system X is reconstructed according to

$$x_{I\!P} = \frac{Q^2 + M_X^2}{Q^2 + W^2}, \tag{6.2}$$

at both the hadron and the detector level. The variable M_X is the invariant mass of the hadronic system X which is defined at the hadron level as explained in Sec. 5.2. Fig. 6.2c shows the difference between the logarithms of $x_{I\!P}$ reconstructed at the hadron and the detector level. The resolution is 0.11. For the evaluation of this resolution, only the range $-2.3 < \log x_{I\!P} < -1.5$ is considered. No diffractive cuts are applied in Fig. 6.1c to extend the range to larger values. From the diagram it can be seen that $x_{I\!P}$ is measured too small in the detector for $\log x_{I\!P} > -1.4$ because M_X is reconstructed too small for $M_X > 35$ GeV. The hadron level value for $\log x_{I\!P}$ is very well correlated with the true value. This is shown in Fig. 6.4c. The resolution at the hadron level is 0.001.

The invariant mass of the dijet system is given by (5.3) at both the hadron and the detector level. The difference between M_{12} at those levels is displayed in Fig. 6.2h. The resolution is 2 GeV. The corresponding quantity at the parton level is $\sqrt{\hat{s}}$. The variable M_{12} tends to be reconstructed too small by 0.6 GeV compared to $\sqrt{\hat{s}}$ as can be seen from Fig. 6.4h. The resolution at the hadron level with respect to the true value is 1.5 GeV.

The estimator x_γ^{jets} on the fractional momentum of the parton from the photon entering

the hard subprocess is reconstructed according to

$$x_\gamma^{\text{jets}} = \frac{\sum_{\text{jets}} (E - p_z)^*}{\sum_X (E - p_z)^*} \tag{6.3}$$

at both the hadron and the detector level. The energy and the z component of the momentum are evaluated in the $\gamma^* p$ system (indicated by the superscript '$*$'). The difference between x_γ as reconstructed at both levels is shown in Fig. 6.6a. The resolution is 0.05. Compared to the true x_γ, the quantity at the hadron level is on average reconstructed too low by 0.12 (Fig. 6.6c) with a resolution of 0.07.

The estimator $z_{I\!P}^{\text{jets}}$ on the fractional momentum of the pomeron parton undergoing the hard scatter is calculated from

$$z_{I\!P}^{\text{jets}} = \frac{Q^2 + M_{12}^2}{Q^2 + M_X^2}$$

at both the hadron and the detector level. The resolution at the detector level with respect to the hadron level is 0.08 (Fig. 6.2d). Compared to the true value of $z_{I\!P}$, the quantity at the hadron level is smaller by 0.08 (Fig. 6.4d). The resolution is 0.08.

Cross sections are also measured differentially in the transverse momentum of the leading jet p_T^{jet1}. The difference in the quantity reconstructed at the hadron and the detector level is shown in Fig. 6.2f. The distribution has a Gaussian form, is centred at 0.15 GeV and has a width $\sigma = 1.0$ GeV. The hadron level p_T^{jet1} is well correlated with $\hat{p}_T$, the p_T of the hard scattered partons. The difference is shown in Fig. 6.4f. It is described by a Gaussian distribution of width 0.7 GeV and is centred at -0.2 GeV.

The mean pseudorapidity $\langle \eta_{\text{jet}}^{\text{lab}} \rangle$ of the leading and sub-leading jet is given by (2.14). The difference between $\langle \eta_{\text{jet}}^{\text{lab}} \rangle$ reconstructed at the hadron and detector levels is displayed in Fig. 6.2e. The jets are in average reconstructed too far forward by 0.02. The resolution is 0.05. Compared to the mean pseudorapidity of the two outgoing hard partons, the hadron level $\langle \eta_{\text{jet}}^{\text{lab}} \rangle$ is larger by 0.06 (Fig. 6.4e). The resolution is 0.08.

The jet separation $\left|\Delta\eta_{\text{jet}}^*\right|$ is defined in the $\gamma^* p$ system according to (2.9) at both the detector and the hadron level. The resolution at the detector level is 0.1 (Fig. 6.2i). The quantity at the hadron level is correlated with the corresponding parton level $\left|\Delta\eta_{\text{jet}}^*\right|$. The resolution is 0.26 (Fig. 5.4i).

All variables are well correlated between the hadron and the detector level. The kinematic region of the cross section is defined in terms of variables reconstructed at the hadron level. The correlation with the true parton level is not perfect. This stems mainly from the fact that the jets and the partons from the hard subprocess are not perfectly correlated.

6.2 Monte Carlo modelling of the data

A combination of diffractive and standard DIS Monte Carlo events is used to correct the event variable distributions of the data for detector smearing. To avoid double counting, the different processes are used in distinct regions of the phase space. RAPGAP in the diffractive mode (cf. Sec. 2.3.1) is used for the region

$$x_{I\!P}^{\text{had}} < 0.2 \quad \text{AND} \quad M_Y = m_p,$$

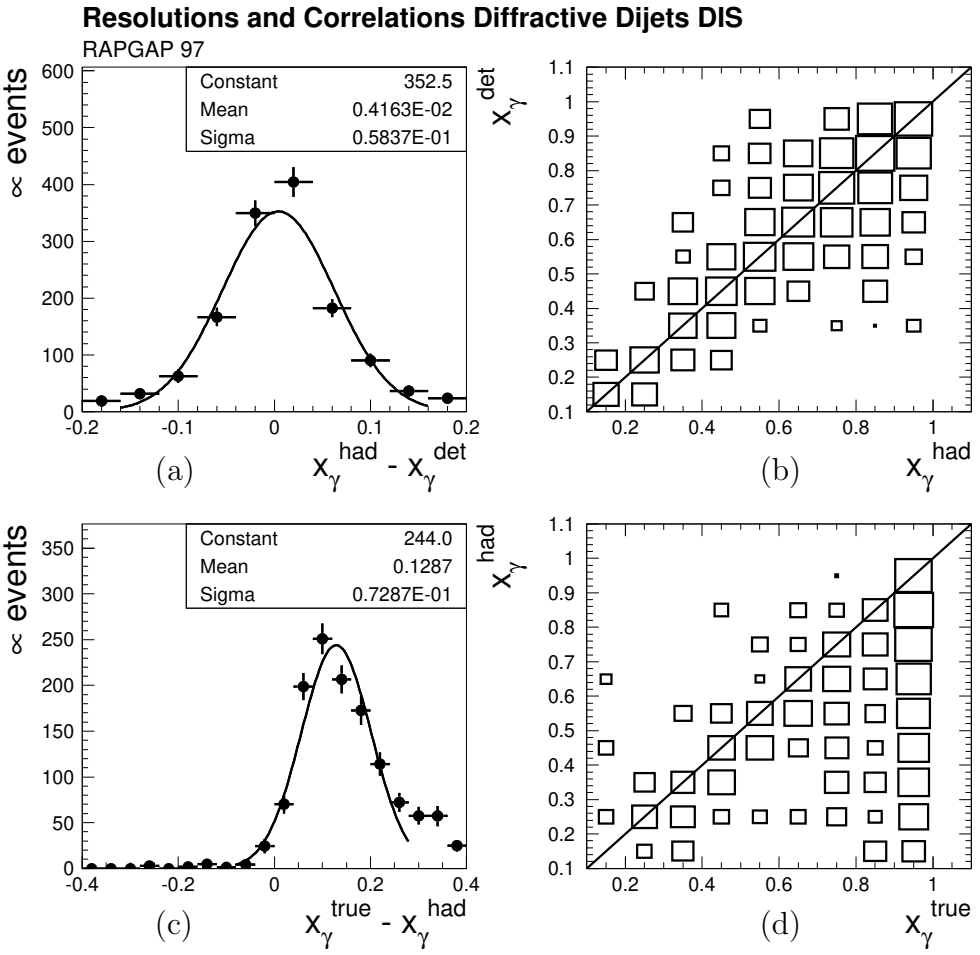

Fig. 6.6. Correlations for x_γ evaluated with the diffractive MC model for 97. (a) The difference between the value reconstructed at the hadron level and the detector level. (b) The correlation of the hadron level x_γ (horizontal axis) and the detector level x_γ (vertical axis). (c) The difference between the true (parton level) x_γ and x_γ as reconstructed at the hadron level. (d) Correlation between the true x_γ (horizontal axis) and x_γ as reconstructed at the hadron level (vertical axis).

whereas RAPGAP in the inclusive DIS mode (cf. Sec. 2.3.2) is used for the region

$$x_{I\!P}^{\mathrm{had}} > 0.2 \quad \text{OR} \quad M_Y > 5 \text{ GeV}. \tag{6.4}$$

For $m_p < M_Y < 5$ GeV, the DIFFVM program is used. In the following, the event sample of the standard DIS model is referred to as 'non-diffractive' because of the anti-diffractive cuts (6.4). In the non-diffractive model prediction, the contribution from resolved virtual photon processes is missing. This leads to discrepancies in the description of quantities reconstructed from the electron, such as Q^2. However, the non-diffractive background is small in the final sample of diffractive events and the contribution of the missing processes is covered by the systematic error assigned to the non-diffractive background.

As in the photoproduction analysis, the normalisation of the two Monte Carlo samples is obtained from the $x_{I\!P}$ distribution shown in Fig. 6.14a and Fig. 6.15a for 96 and 97, respectively. The description at large $x_{I\!P}$ is bad also in DIS. Therefore, a large systematic uncertainty of 50% is assumed for the number of migrations from large $x_{I\!P}$. The bad description and the consequences for the analysis are discussed in detail in Sec. 5.2.

6.3 Event selection

This section describes the selection criteria imposed to isolate the diffractive dijet events used in the cross section measurement. The inclusive DIS selection is summarised in Tab. 6.1.

6.3.1 Basic event selection

For every event it is checked that for all required detector components the high voltage is at the operating level and that the system is included in the read-out chain. The same detector components are required as in the photoproduction analysis (Sec. 5.3.1). The same data sets and reconstruction software versions that were used in the photoproduction analysis are also used for the DIS measurement.

6.3.2 Triggers and trigger efficiency

Low Q^2 DIS dijet events are triggered by requiring a cluster in the electromagnetic part of the SPACAL, an event vertex and large transverse momentum tracks in the central region of the detector.

The electron trigger requires energy above some threshold in the electromagnetic part of the SPACAL. For 96 and 97 these thresholds were 2 GeV and 6.5 GeV, respectively. In this analysis, only electron candidates with energy larger than 8 GeV are considered. For this energy, the resolution of the SPACAL is 0.2 GeV. Therefore, the efficiency for triggering the electron in the geometrical acceptance region of the SPACAL is close to 100%. The same track trigger requirement is used as in the photoproduction analysis (cf. Sec. 5.3.2).

Trigger efficiency

The trigger efficiency is derived from the data using monitor triggers. The trigger efficiency is shown in Figs. 6.7 and 6.8 as a function of the cross section variables for the combined

inclusive DIS dijet sample of 96 and 97. The trigger efficiency is parameterised two-dimensionally as a function of the average jet p_T and the average jet pseudorapidity. The parameterisation is shown in the figure and describes the efficiency within 5%. The parameterisation is obtained from the inclusive dijet data sample without any diffractive cut because the statistics are very low for diffractive dijet events when a monitor trigger signal is required. The efficiency in diffractive dijet events is not expected to be different from the inclusive case except that the jets might be located more backward in diffraction because the forward region is required to be devoid of activity. This possible effect is taken into account by the η dependent parameterisation. The overall trigger efficiency is around 90%. This parameterisation is used to correct the data and the 5% uncertainty translates into a 6% systematic error for the cross sections.

6.3.3 Raw event rate and integrated luminosity

Shown in Figs. 6.9a and b is the accumulated number of diffractive dijet events as a function of the integrated luminosity. The plots Figs. 6.9c and d show the number differentially per luminosity as a function of the integrated luminosity. The number of events is corrected for trigger inefficiencies. From the differential plots it can be seen that the rate is stable within the statistical errors. The integrated luminosities for 96 and 97 are 5.4 pb^{-1} and 10.1 pb^{-1}, respectively. In 96, the luminosity is lower than in the photoproduction analysis. This is due to the fact the DIS analysis originally required an additional detector component to be in operation. This detector is not used for the final analysis.

6.3.4 Cuts on the electron candidate

The scattered electron is detected in the SPACAL calorimeter. Some fiducial cuts had to been applied to reject areas of the SPACAL where this detector was not fully operational because of problems with the high voltage. More SPACAL cells had to be excluded in 96 compared to 97. Therefore, the efficiency for the electron reconstruction is reduced in 96 compared to 97. See [37] for details. The electromagnetic cluster measured in the SPACAL with the largest energy is considered the electron candidate. The energy E'_{e} of the electron candidate cluster is required to be larger than 8 GeV:

$$E'_{\text{e}} > 8 \text{ GeV}.$$

This cut reduces photoproduction background with a fake electron which typically has a smaller energy. The distribution of E_{e} is shown in Fig. 6.10a. The missing resolved virtual photon processes in the MC lead to a discrepancy at large energies. This discrepancy is not seen if an additional cut $Q^2 > 12$ GeV^2 is applied which suppresses resolved photon contributions.

The geometrical acceptance of the SPACAL calorimeter is reflected in the cut on the polar angle θ_e of the electron cluster:

$$156^{\text{o}} < \theta_e < 176^{\text{o}}.$$

The distribution of θ_e is displayed in Fig. 6.10b. Again, a discrepancy is seen at large angles (small Q^2) due to the missing resolved photon processes.

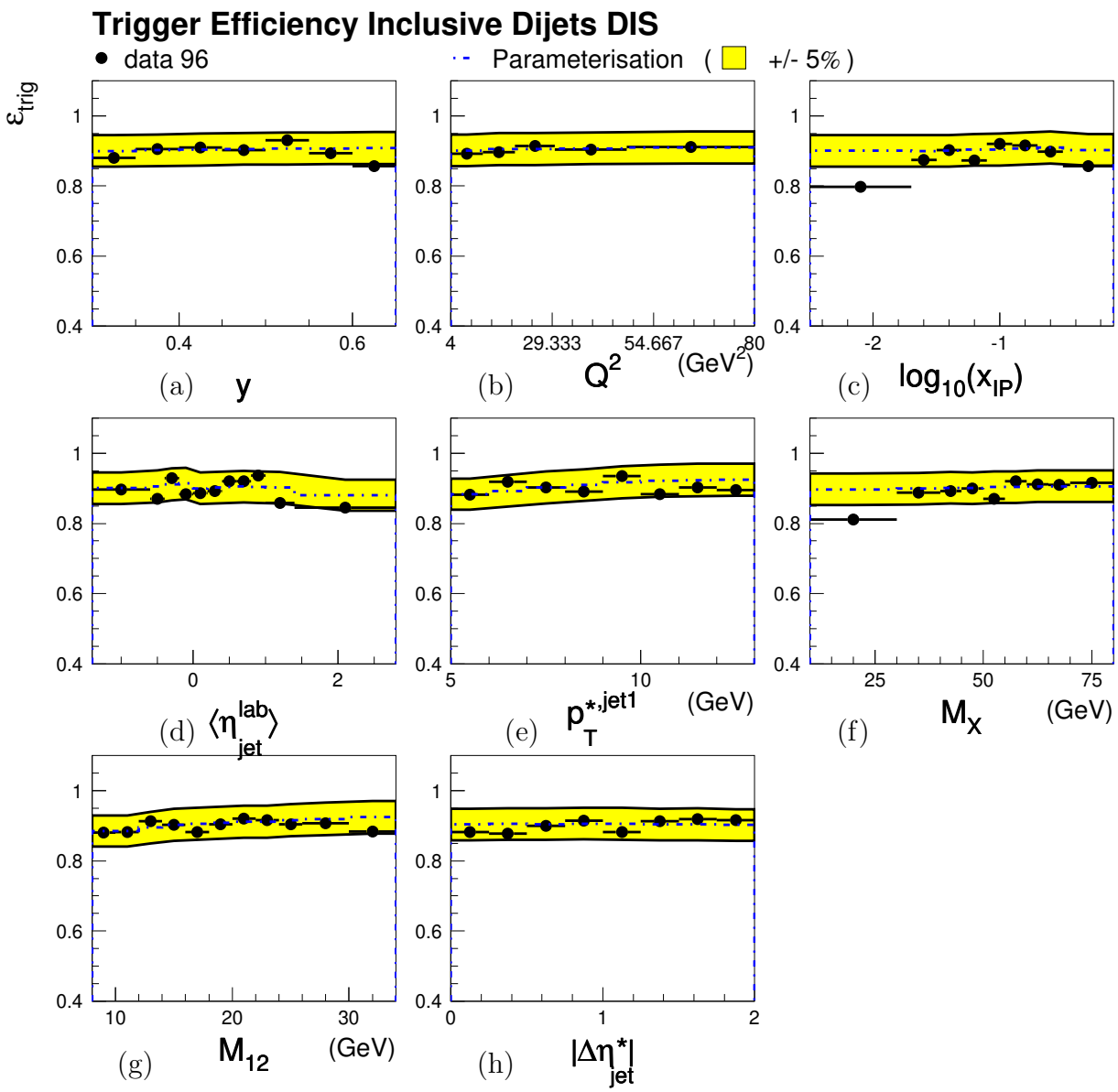

Fig. 6.7. Trigger efficiency for inclusive DIS dijets in 96. Also shown as the dotted line is the parameterisation which is used for the correction of the data. A ±5% band around the parameterisation is indicated which is taken as the uncertainty of the trigger efficiency.

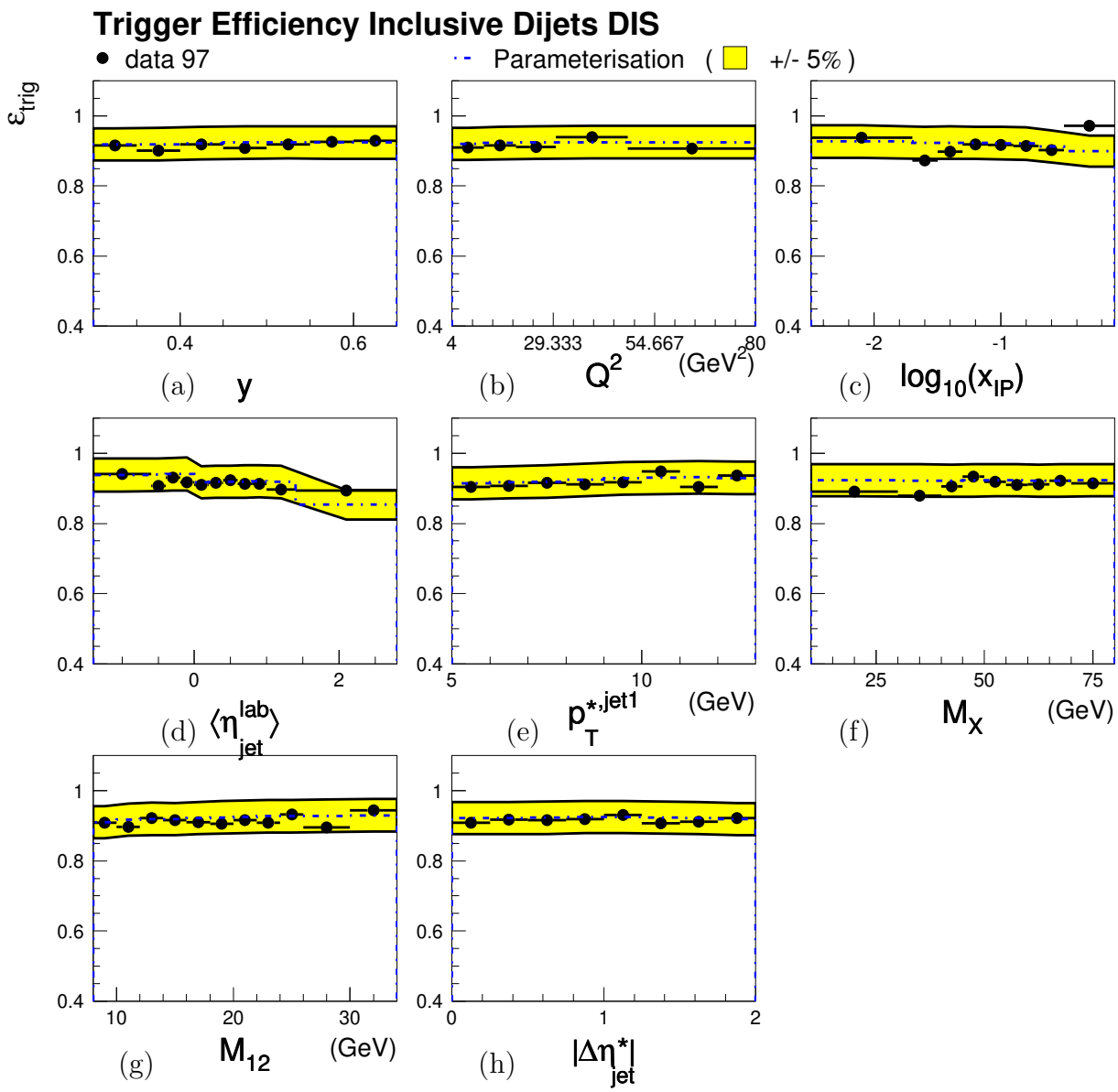

Fig. 6.8. Trigger efficiency for inclusive DIS dijets in 97. Also shown as the dotted line is the parameterisation which is used for the correction of the data. A ±5% band around the parameterisation is indicated which is taken as the uncertainty of the trigger efficiency.

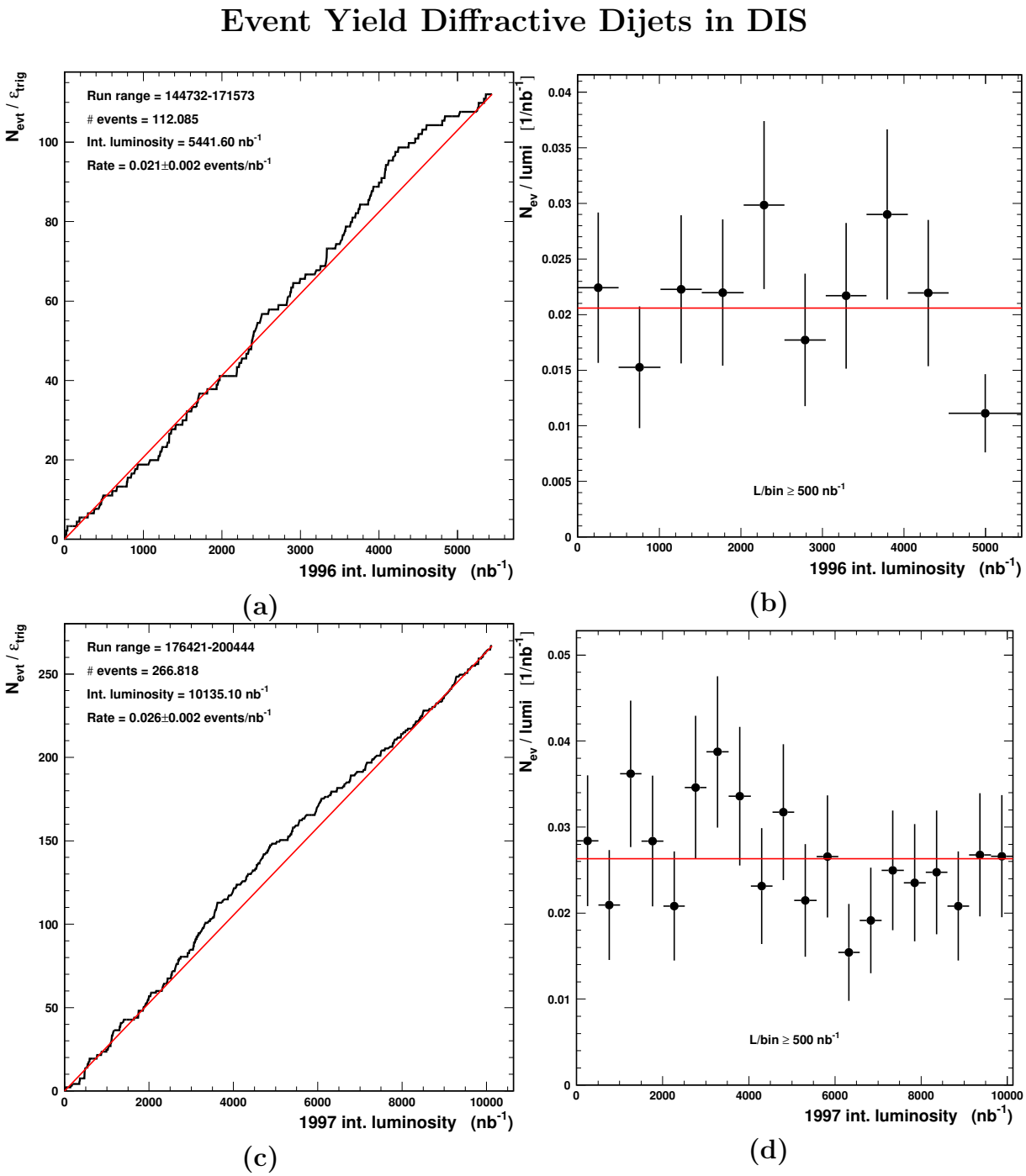

Fig. 6.9. Yield of diffractive DIS dijet events. Shown in (a) for 96 and (b) for 97 is the number of accumulated diffractive dijet events as a function of the integrated luminosity. The accumulated number of events is shown per luminosity in (b) for 96 and (d) for 97 as a function of the integrated luminosity. The number of events is corrected for the trigger inefficiency and is multiplied by the trigger prescale factor.

The cuts on the energy and the polar angle of the electron cluster limit the kinematically allowed phase space in Q^2. The virtuality Q^2 is explicitly restricted to the range

$$4 < Q^2 < 80 \text{ GeV}^2.$$

Fig. 6.10c shows the Q^2 distribution for the inclusive DIS dijet sample. The model describes the overall shape. The discrepancy at small Q^2 results from the missing resolved photon processes.

To restrict the measurement to the same centre-of-mass energy in the photon-proton system as in the photoproduction analysis, the following cuts on W are applied:

$$165 < W < 242 \text{ GeV}.$$

The W distribution is shown in Fig. 6.10d and is described by the model.

The following cuts ensure a good measurement of the electron cluster. The part of the SPACAL directly next to the beam pipe suffers from high backgrounds. This region is avoided by requiring the distance between the cluster and the beam pipe to be larger than 9 cm:

$$d_{\text{cluster}-\text{beam}} > 9 \text{ cm}.$$

The distribution of $d_{\text{cluster}-\text{beam}}$ is shown in Fig. 6.11a. Most of the clusters are located at 20 cm. The description is not particularly good at this value. However, the cut does not reject any events because the region at small distances is already depopulated by the cut $Q^2 > 4$ GeV^2. The decrease at larger distances is a reflection of the Q^2 dependence of the cross section.

To ensure a correct energy measurement, the electron cluster must be fully contained within the SPACAL. Therefore, the energy E_{veto} in the veto layer of the SPACAL next to the beam pipe is required to be less than 1 GeV:

$$E_{\text{veto}} < 1 \text{ GeV}.$$

The distribution of E_{veto} is shown in Fig. 6.11b. It is described by the model.

The following cuts are applied to veto background processes where a hadron is misidentified as an electron. The electromagnetic part of the SPACAL amounts to 28 radiation lengths. Any electromagnetic particle shower should therefore be fully contained within this section. Activity in the hadronic SPACAL behind the electromagnetic section indicates that the electron candidate signal is produced by a hadron. To reject these fake electrons, the energy E_{had} in the hadronic part behind the electron candidate is required to be less than 0.5 GeV:

$$E_{\text{had}} < 0.5 \text{ GeV}.$$

A cone around the electron direction with opening angle 4^{o} defines the region where the hadronic energy is summed up. The distribution of this energy is shown in Fig. 6.11c. The number of rejected events is only at the per mill level. The description is not perfect.

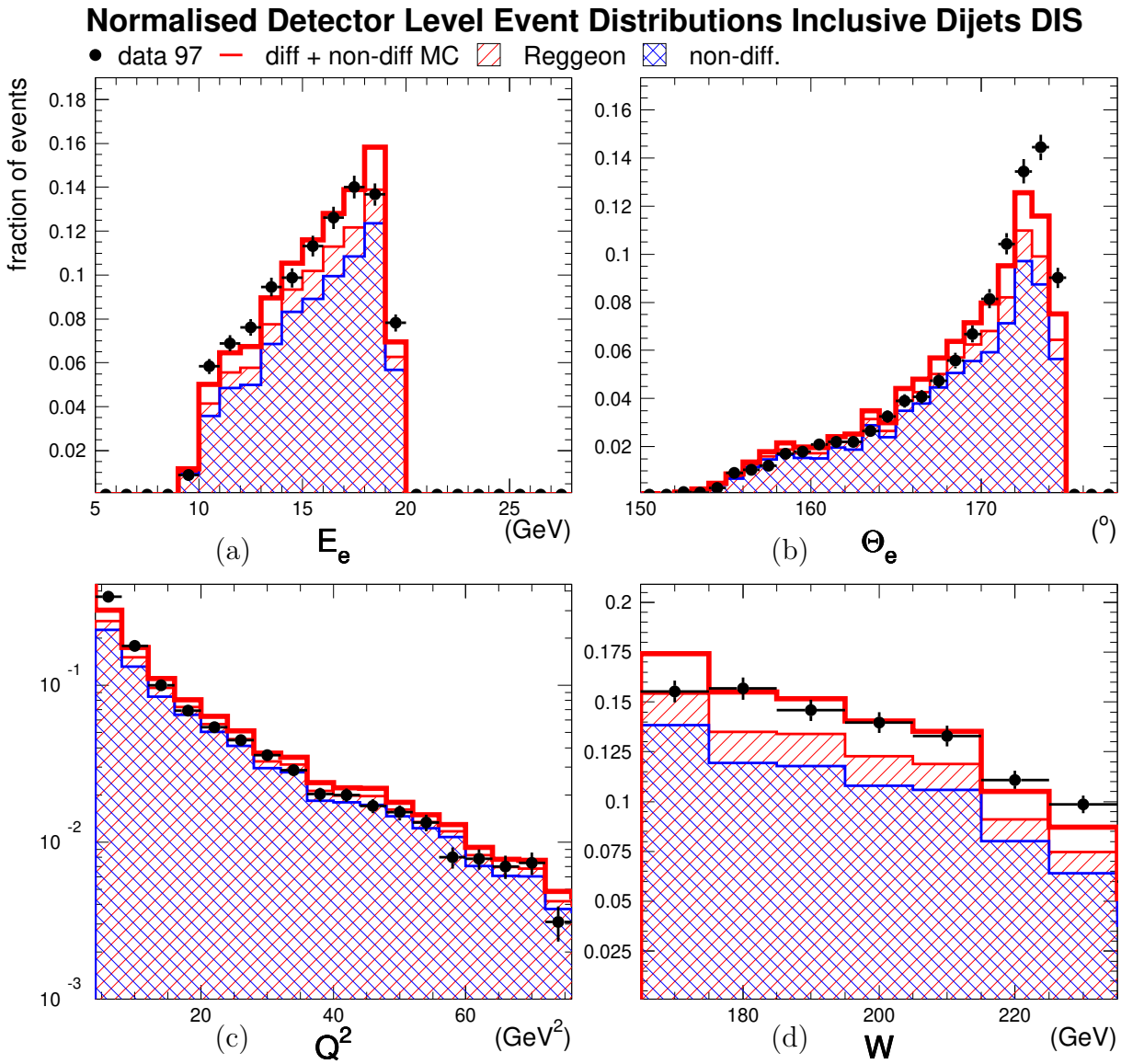

Fig. 6.10. Normalised distributions for the inclusive DIS dijet sample for 97. (a) energy E'_e of the scattered electron, (b) electron polar scattering angle θ_e, (c) Q^2 and (d) W. The model does not include processes with a resolved virtual photon.

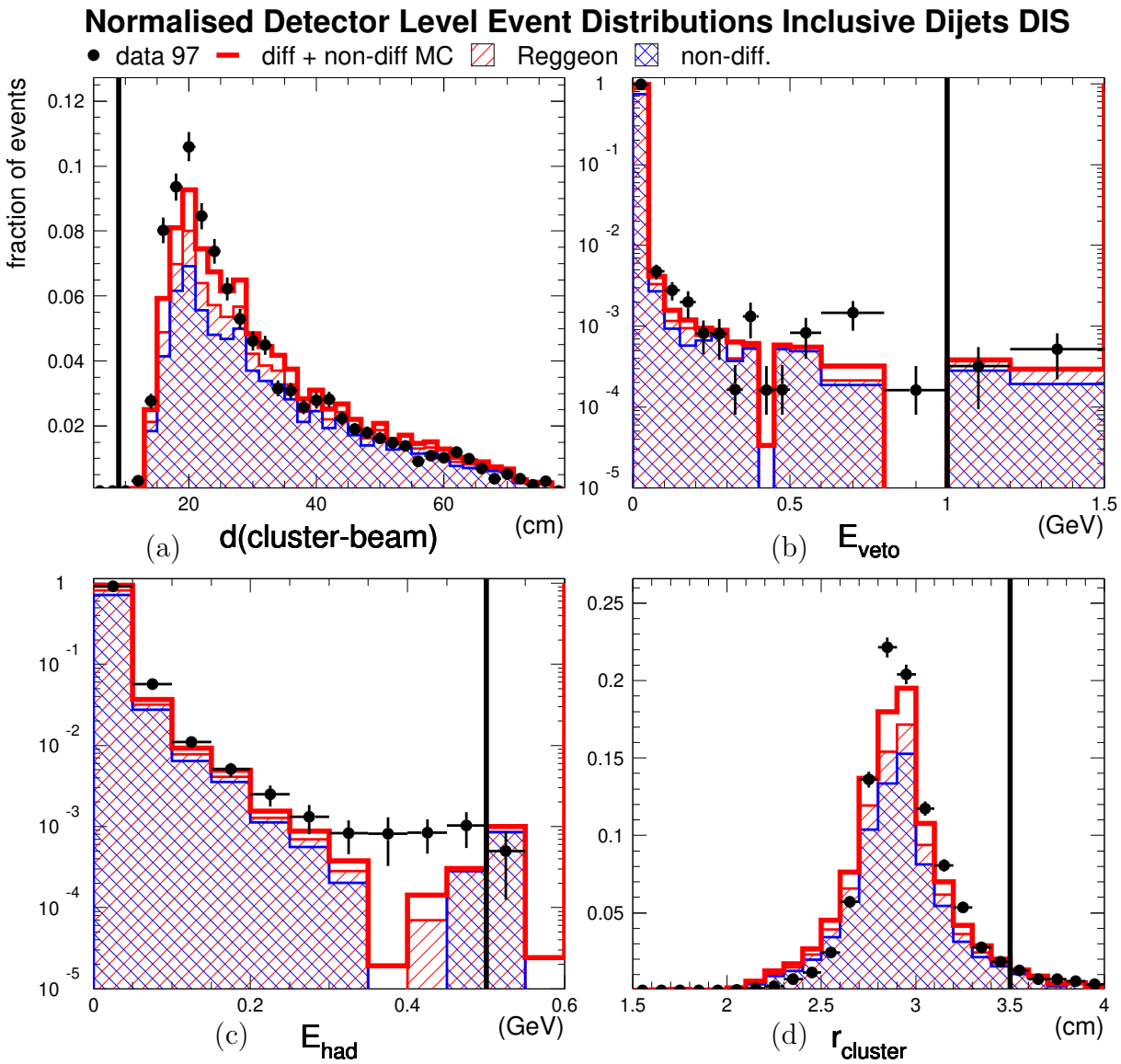

Fig. 6.11. Normalised distributions for the inclusive DIS dijet sample. (a) Distance between the electron cluster and the beam pipe, (b) energy in the SPACAL veto layer, (c) hadronic energy behind the electron cluster, (d) radius of the cluster.

The distribution of the radius R_{clus} of the electron cluster is shown in Fig. 6.11d. The radius is required to be less than 3.5 cm:

$$R_{\text{clus}} < 3.5 \text{ cm}.$$

A hadronic particle generally produces broader showers in the calorimeter than a purely electromagnetically interacting particle. For the model description, the radius had to be enlarged by 5% because the simulation underestimated the shower width. The description is reasonable at the cut value.

As a further veto against background processes which result in a fake electron cluster in the SPACAL, tracking information from the BDC is used. It is required that the distance between the cluster and the closest track in the BDC is less than 3 cm:

$$d_{\text{BDC}} < 3 \text{ cm}.$$

An uncharged hadron like the π^0 will not produce a track in the BDC and such events are therefore rejected. The distribution of d_{BDC} is shown in Fig. 6.12a. The number of events lost due to this cut is approximately 1%. The description is good.

6.3.5 Event vertex requirement

An event vertex must have been found by the tracking system. The z component of the vertex position must lie around the nominal interaction point at $z = 0$:

$$|z_{\text{vtx}}| < 35 \text{ cm}.$$

This cut rejects background from beam-gas or beam-beampipe interactions. Shown in Fig. 6.12b is the z_{vtx} distribution for the inclusive DIS dijet sample for 97. The data are corrected for trigger inefficiencies. The model predictions have been improved by reweighting the MC in the z component of the simulated vertex. The original prediction is shown as the dotted histogram. No reweighting had to be applied for 96. For the diffractive sample, the model describes the data within the large statistical errors of the data.

6.3.6 Containment of the event

The quantity $\sum_i E_i - p_{z,i}$ can be calculated for every event. The sum is over all objects in the event and considers also the scattered electron. This quantity must be conserved in the interaction. In the initial state, before the collision, it is given by twice the electron beam energy. Fig. 6.12c shows the distribution for the inclusive dijet DIS sample. It is indeed peaked at 55 GeV. The description by the model is fine. A cut

$$E - p_z > 35 \text{ GeV}$$

is applied to reject photoproduction background. In these photoproduction background events, the electron is scattered by a small angle and escapes through the beam pipe. For these events, $E - p_z$ is reconstructed significantly below 55 GeV because the contribution from the scattered electron is missing in the sum. In addition to rejecting photoproduction

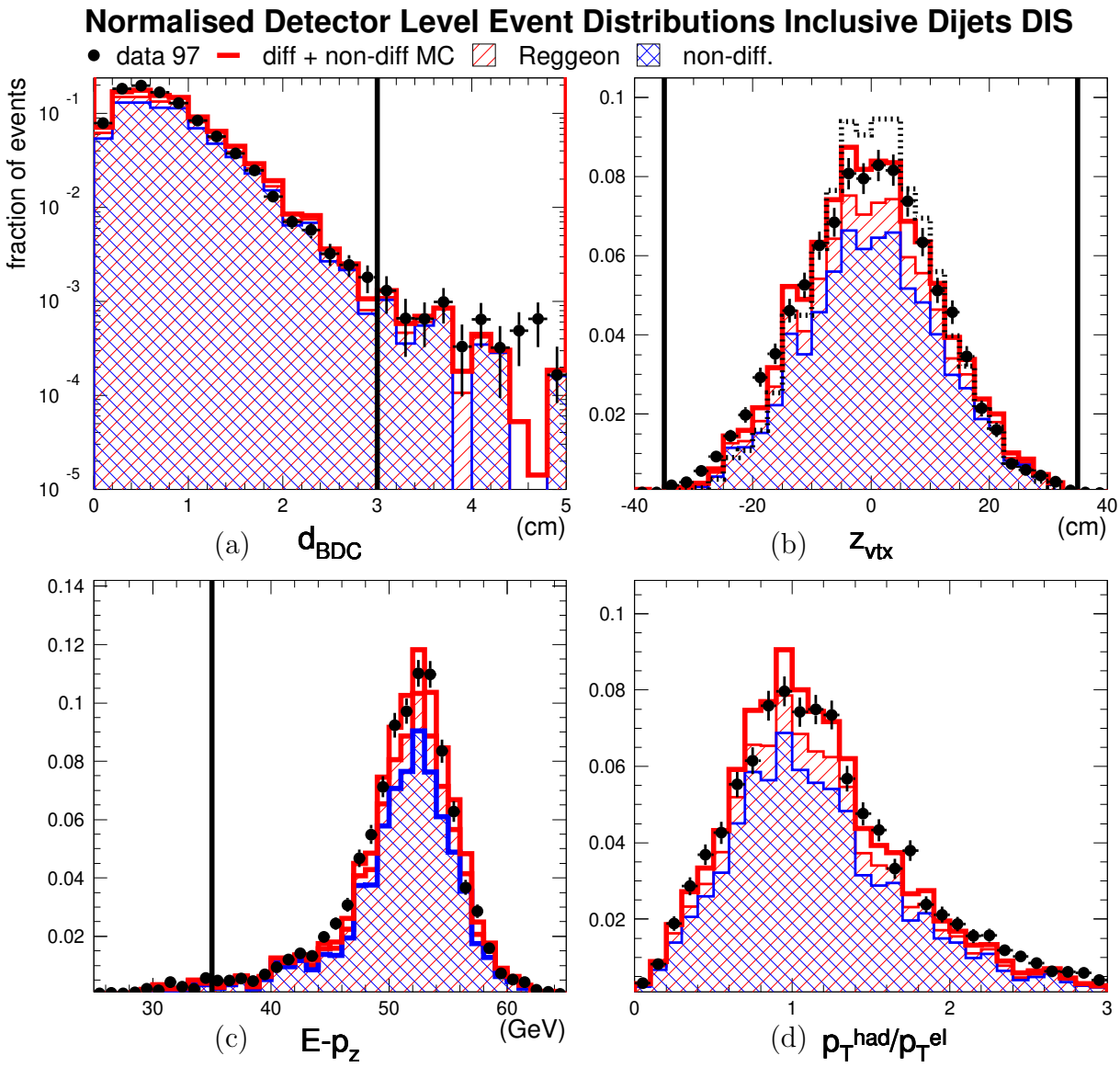

Fig. 6.12. Normalised distributions for the inclusive DIS dijet sample. (a) Distance between the electron cluster and the nearest track in the BDC. (b) The z_{vtx} distribution of the Monte Carlo has been reweighted. The original prediction is shown as the dotted histogram. (c) The quantity $E - p_z$. (d) The ratio of the transverse momenta of the electron and the hadronic system.

DIS Selection

Cut	*Reason*
$\lvert z_{\text{vtx}}\rvert < 35$ cm	veto beam/gas, beam/pipe bgr.
$E - p_z > 35$ GeV	γp and ISR bgr. processes
electron energy > 8.0 GeV	γp bgr.
$4 < Q^2 < 80$ GeV^2, $156^\text{o} < \theta_\text{e} < 176^\text{o}$	SPACAL acceptance
distance cluster–beam pipe > 9 cm	high bgr. in inner SPACAL region
$165 < W < 242$ GeV	comparison with γp measurement
electron cluster radius < 3.5 cm, distance to closest BDC hit < 3.0 cm, had. energy behind electron < 0.5 GeV	veto against fake electrons
energy in SPACAL veto layer < 1.0 GeV	avoid leakage out of SPACAL

Tab. 6.1. Summary of the inclusive DIS selection.

events, the cut on $E - p_z$ also suppresses initial state QED radiative events in which the incoming beam electron has emitted a real photon before interacting with the proton and therefore has lost part of its energy.

6.3.7 Transverse momentum balance

In a DIS event, the transverse momenta of the scattered electron and the hadronic final state should be equal. In Fig. 6.12d, the ratio of the transverse momenta is shown. It is peaked at unity and the description by the model is fine.

6.3.8 Dijet selection

As in the photoproduction analysis, the inclusive k_T jet algorithm with a distance parameter of unity is used to identify jets. The combined objects from calorimeter and track information (cf. Sec. 2.3.4.1) are Lorentz-boosted into the photon-proton frame before they are subjected to the jet algorithm. For the leading jet, the transverse energy E_T^* in the $\gamma^* p$ frame is required to be larger than 5 GeV. For the subleading jet, $E_T^* > 4$ GeV is required. The jets are demanded to lie within the acceptance region of the central detector. A cut is applied on the pseudorapidity of the jets in the laboratory frame as in photoproduction. The dijet selection is summarised in Tab. 5.2. Fig. 6.13 shows dijet distributions for the inclusive DIS dijet sample. The p_T of the leading jet is well described (Fig. 6.13a). The mean pseudorapidity of the jets in the laboratory frame is shown in Fig. 6.13b. In the MC, the distribution is shifted backwards by ≈ 0.1. Figs. 6.13c and d show the pseudorapidities in the laboratory frame of the leading and the subleading jet,

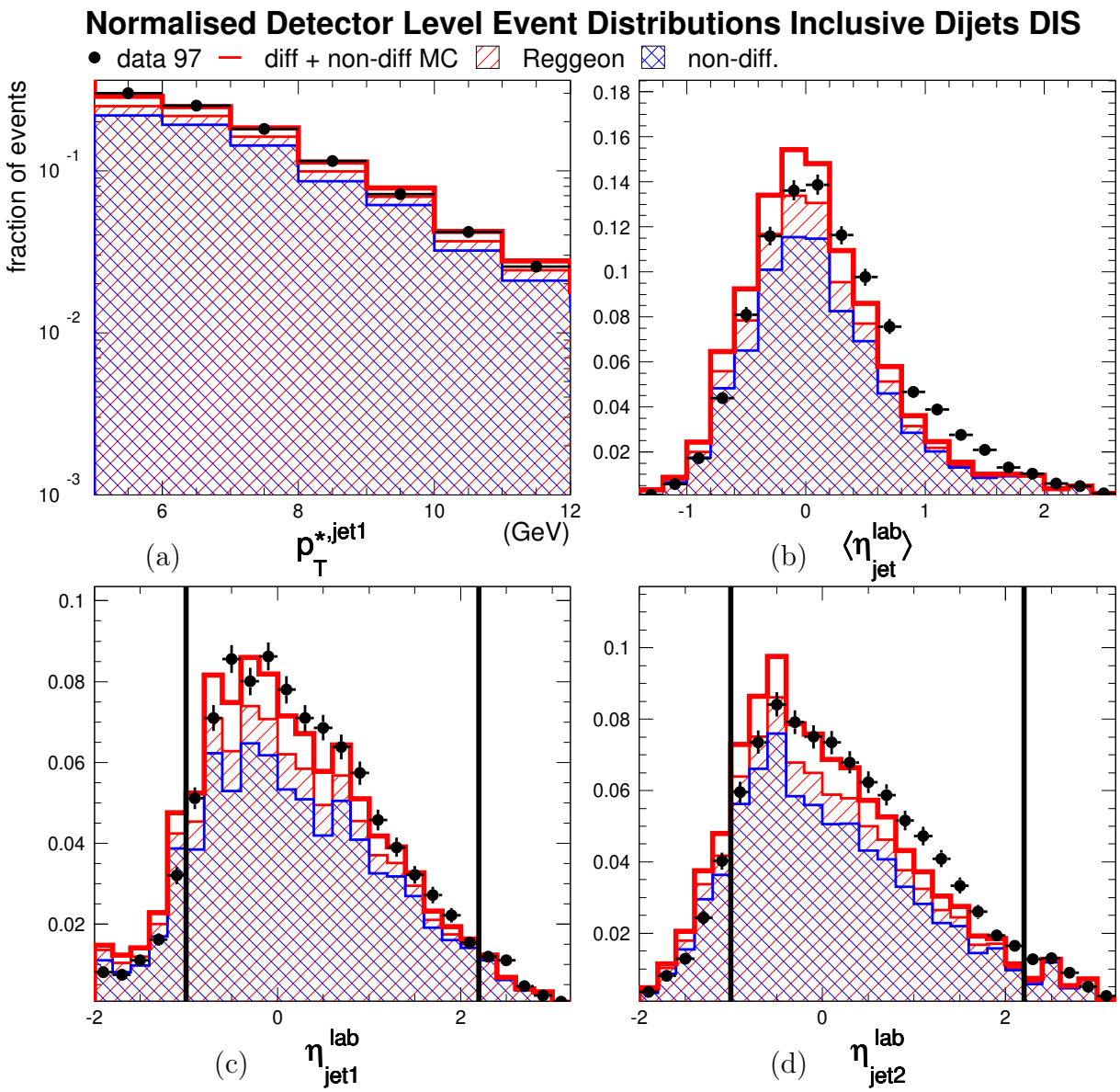

Fig. 6.13. Normalised distributions for the inclusive DIS dijet sample. (a) Transverse momentum of leading jet in $\gamma^* p$ system. (b) Mean pseudorapidity of the two leading jets, (c) pseudorapidity of the leading jet (d) pseudorapidity of the subleading jet. (b-d): pseudorapidities in the laboratory frame.

respectively. For the leading jet, the agreement is good in the central and the forward part. In the backward region, the model overestimates the jet rate. For the subleading jet, the description is worse. However, the contribution of non-diffractive events to the final diffractive selection is very small and in addition, an uncertainty of 50% is assumed for this number. Therefore, the agreement is found to be good enough.

6.3.9 Selection of diffractive events in DIS

Rapidity gap events are selected in the same way as in the photoproduction analysis (cf. Sec. 5.3.9). Cuts on the activity in the forward region of the detector select events with a rapidity gap between $3.2 < \eta < 7.5$ and ensure that $M_Y < 1.6$ GeV and $-t < 1$ GeV^2. The diffractive selection is summarised in Tab. 5.3. After all cuts, 101 diffractive dijet events are selected for 96 and 248 for 97. The contribution of non-diffractive events is 4% for 96 and 6% for 97.

6.3.9.1 Cut on $x_{I\!P}$

The $x_{I\!P}$ distribution is shown in Fig. 6.14a and Fig. 6.15a for 96 and 97, respectively. The normalisation of the Monte Carlos has been obtained from this spectrum. The description is good in the region relevant for the analysis. For a discussion of the bad description at large $x_{I\!P}$ see Sec. 5.2. To reject non-diffractive processes, the same cut (5.6) is applied as in photoproduction.

6.3.9.2 Cut on most forward cluster in the LAr calorimeter

Fig. 6.14b and Fig. 6.15b show the $\eta_{\max}$ distribution for the inclusive DIS dijet sample with an additional cut $x_{I\!P} < 0.1$ applied to reject the badly described region at large $x_{I\!P}$. The MC underestimates the rate for $\eta_{\max} < 3.2$. This is due to the missing proton dissociation events in the MC. The cut (5.7) is applied to decrease contributions from non-diffractive processes.

6.3.9.3 Activity in the FMD

The FMD hit pairs distribution is shown in Fig. 6.14c and Fig. 6.15c. The cut (5.8) is applied. For the model, noise had to be added because it is not covered by the H1 detector simulation. See Sec. 5.3.9.3 for the discussion on the determination of the noise frequency. The DIS analysis uses the same run ranges and diffractive cuts as the photoproduction analysis. Therefore, the same noise correction is applied in both analyses.

6.3.9.4 Hits in the PRT

The distribution of hits in the PRT is shown in Fig. 5.11d and Fig. 5.12d. The model has been reweighted according to the procedure described in Sec. 5.3.9.4. The description is not perfect in both years.

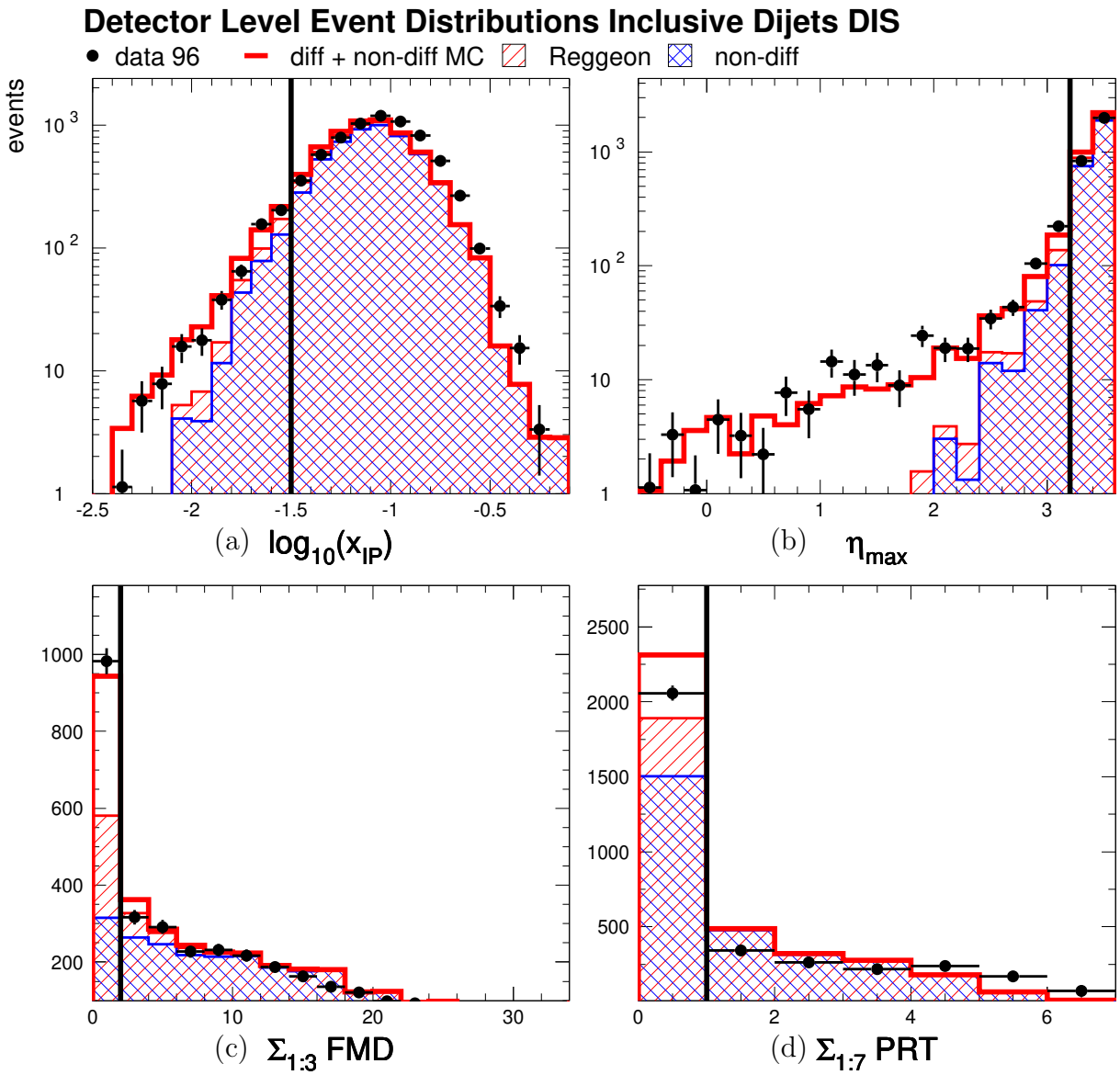

Fig. 6.14. Distributions of the diffractive cut variables for the events of the inclusive DIS dijet sample of 96. (a) $x_{I\!P}$, (b) $\eta_{\max}$, (c) FMD and (d) PRT. For (c), FMD noise has been added in the MC.

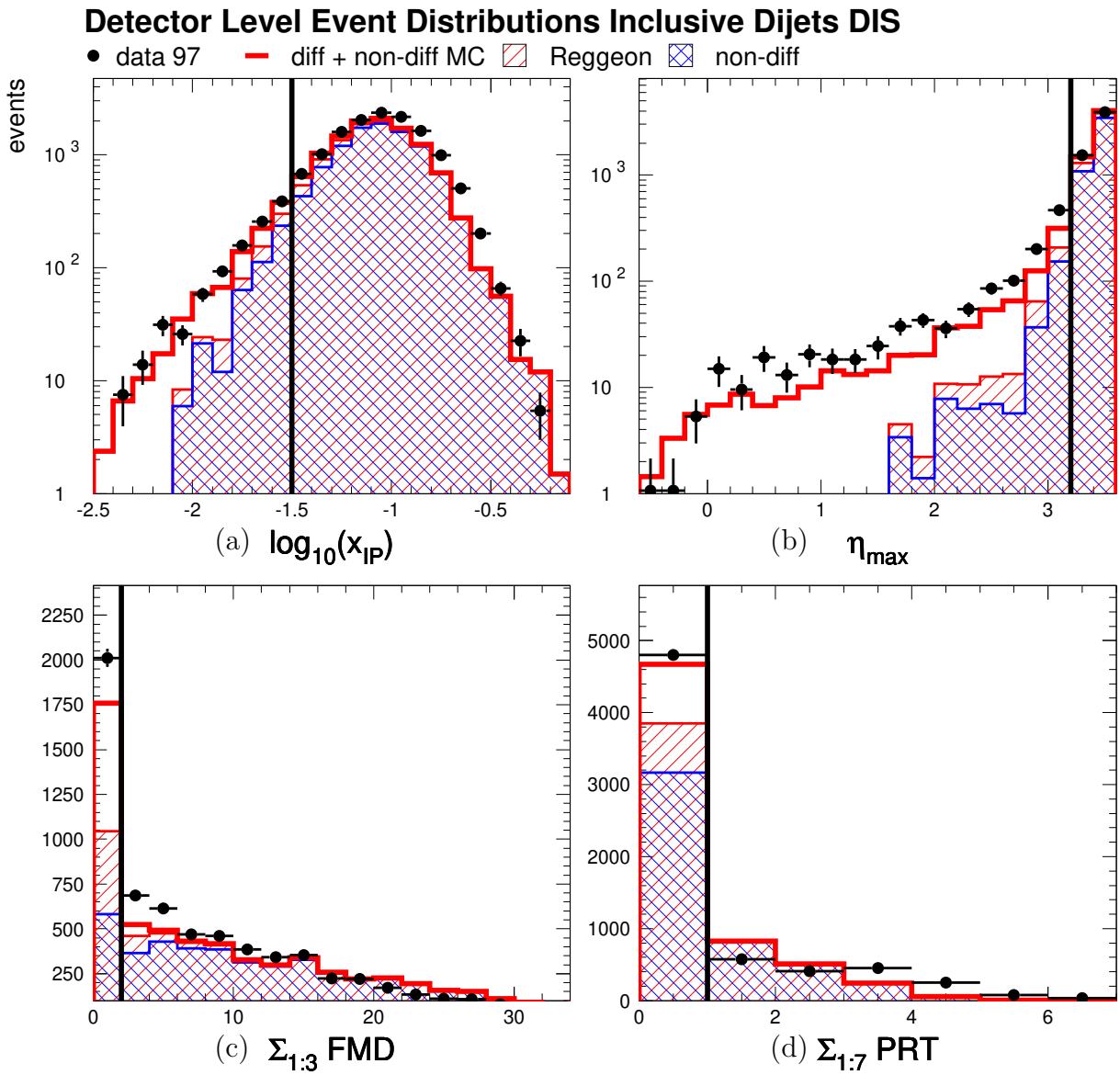

Fig. 6.15. Distributions of the diffractive cut variables for the events of the inclusive DIS dijet sample of 97. (a) $x_{I\!P}$, (b) $\eta_{\max}$, (c) FMD and (d) PRT. For (c), FMD noise has been added in the MC.

6.4 Control plots for diffractive dijets in DIS

In this section, further control plots are presented which show that the Monte Carlo model describes the data and can therefore be used for the correction.

6.4.1 Description of kinematic variables in DIS

Distributions for the cross section variables at the detector level are shown in Fig. 6.16 and Fig. 6.17 for the diffractive dijet samples of 96 and 97, respectively. The normalisation of the non-diffractive MC has been obtained from the $x_{I\!P}$ distribution of the inclusive sample. It is left unchanged after the diffractive cuts have been applied. The normalisation of the diffractive MC is scaled such that the sum of the diffractive and the non-diffractive MC is equal to the number of data events. The diffractive model is reweighted in z_{vtx} and x_γ. Fig. 6.18 shows the x_γ distribution. The parton densities in the photon have been reweighted by a cubic function in x_γ. The prediction without the reweight is indicated by the dotted histogram. All distributions are described within the statistical errors of the data.

6.4.2 Energy flow in diffractive DIS dijet events

In order to use the Monte Carlo events for the detector smearing correction the model must also describe the distributions of the basic calorimeter clusters and tracks.

Fig. 6.19 shows the mean energy flow in a diffractive dijet event as a function of the pseudorapidity calculated in the laboratory frame. Only events are considered in which the jet axes satisfy $\eta_{\mathrm{jet}} < 1$. In Fig. 6.19a, the energy is reconstructed from the combined objects of calorimeter clusters and tracks. The energy obtained from actually matched clusters and tracks is shown in Fig. 6.19b whereas only clusters and only tracks are used for Fig. 6.19c and Fig. 6.19d, respectively. The average multiplicity of the objects is shown in Fig. 6.20. The track energy and multiplicity is very well reproduced by the model. The description of the multiplicity of the calorimeter clusters is good in the backward and in the central area. In the forward region, the model seems to overestimates the particle multiplicity. However, when the forward region is studied more closely, it can be seen that the prediction describes the data distribution within the uncertainties of the data. This can be seen in Fig. 6.21 which shows the average energy per event reconstructed from LAr calorimeter cells for dijet events fulfilling the diffractive cuts

$$x_{I\!P} < 0.03 \quad \text{AND} \quad \sum_{1:3} \mathrm{FMD} < 2.$$

Fig. 6.21a shows the energy as a function of the pseudorapidity in the laboratory frame. Fig. 6.21b shows the cell energy in the forward part of the LAr calorimeter ($270 < z < 450$ cm) as a function of the radial distance R from the beam axis. The cell energies are well described.

Fig. 6.22 shows jet profiles of the leading jet in the $\gamma^* p$ centre-of-mass system. The mean transverse energy per event around the jets is shown as a function of the pseudorapidity in Fig. 6.22a. Only energy in the Φ^* hemisphere of the leading jet has been

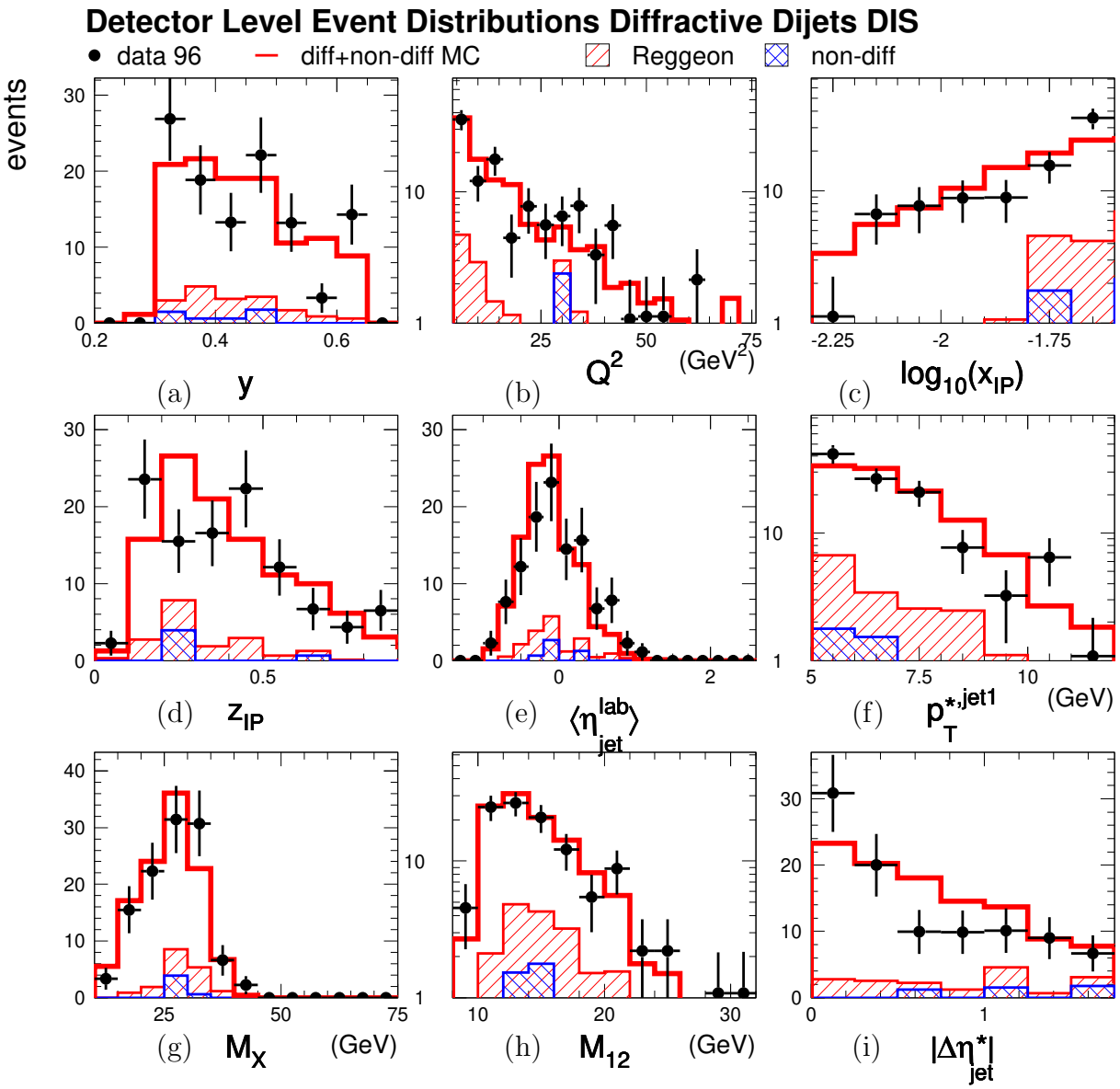

Fig. 6.16. Diffractive DIS dijet distributions for 96. (a) y, (b) Q^2, (c) $\log_{10}(x_{I\!P})$, (d) $z_{I\!P}$, (e) $\langle\eta^{\rm lab}_{\rm jet}\rangle$, (f) $p_T^{\rm jet1}$, (g) M_X, (h) M_{12} and (i) $|\Delta\eta_{\rm jet}|$

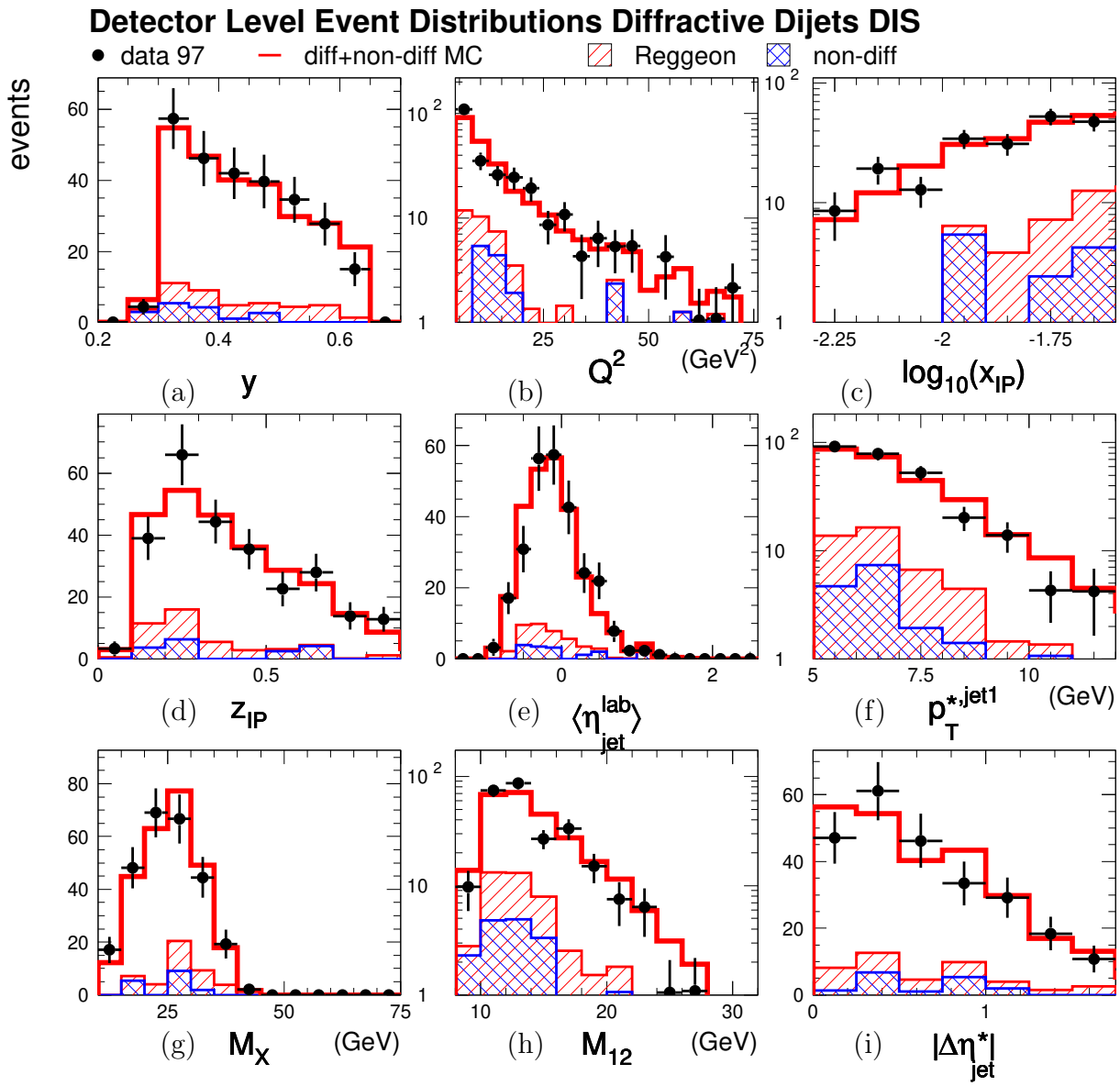

Fig. 6.17. Diffractive DIS dijet distributions for 97. (a) y, (b) Q^2, (c) $\log_{10}(x_{I\!P})$, (d) $z_{I\!P}$, (e) $\langle\eta^{\rm lab}_{\rm jet}\rangle$, (f) $p_T^{\rm jet1}$, (g) M_X, (h) M_{12} and (i) $|\Delta\eta_{\rm jet}|$

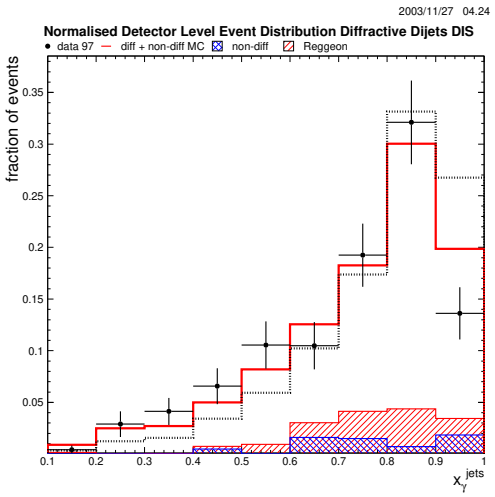

Fig. 6.18. The distribution of x_γ for the diffractive DIS dijet sample of 97. The model is reweighted in x_γ. The prediction without the reweight is shown as the dotted histogram.

considered to eliminate contributions from the subleading jet which typically is aligned back-to-back with the leading jet. The distribution is described by the model within the statistical uncertainties of the data. The average transverse energy per event as a function of the azimuthal angle Φ^* is displayed in Fig. 6.22b. Only energy within a pseudorapidity band $\eta^*_{\text{jet1}} \pm 1$ around the leading jet is considered. The model describes the jet profile nicely.

6.5 Correction to the level of stable hadrons

This section describes the procedure of correcting the data for detector smearing.

6.5.1 Cross section formula

The differential cross section in the variable x is calculated according to

$$\frac{d\sigma}{dx} = \underbrace{\frac{N_{\text{data}}/\varepsilon_{\text{trig}} - N_{\text{non-diffr}}}{C_{\text{det}}}\, C_{M_Y}}_{N_{\text{had}}}\; C_{\text{FMD}}\; C_{\text{QED}}\; \frac{1}{L\, dx}. \tag{6.5}$$

Compared to the corresponding formula in photoproduction (5.9), a new factor C_{QED} is applied. This factor corrects the data for radiative QED effects and is discussed in Sec. 6.5.6. The number N_{had} of events at the hadron level is determined separately for 96 and 97. This procedure takes into account that the configuration of the detector can be different in both years. A combined cross section is derived by adding the corrected event numbers and by dividing by the sum of the luminosities.

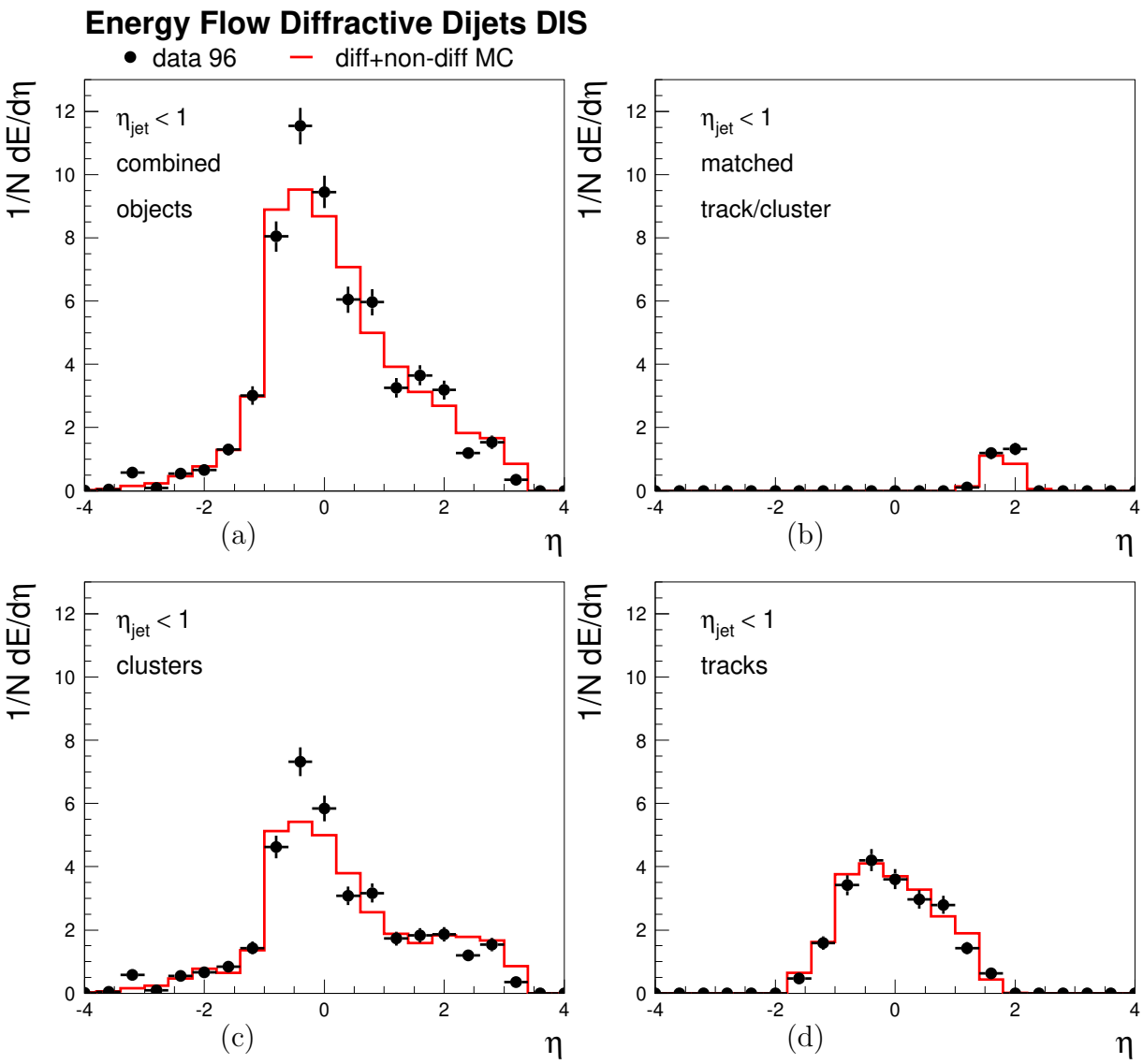

Fig. 6.19. Energy flow for the diffractive DIS dijet sample in 96. Shown is the mean energy as a function of the pseudorapidity η in the laboratory frame. The energy is reconstructed from (a) combined track and calorimeter cluster information, (b) only matched tracks and clusters, (c) clusters, and (d) tracks. The jets are required to satisfy $\eta_{\text{jet}} < 1$.

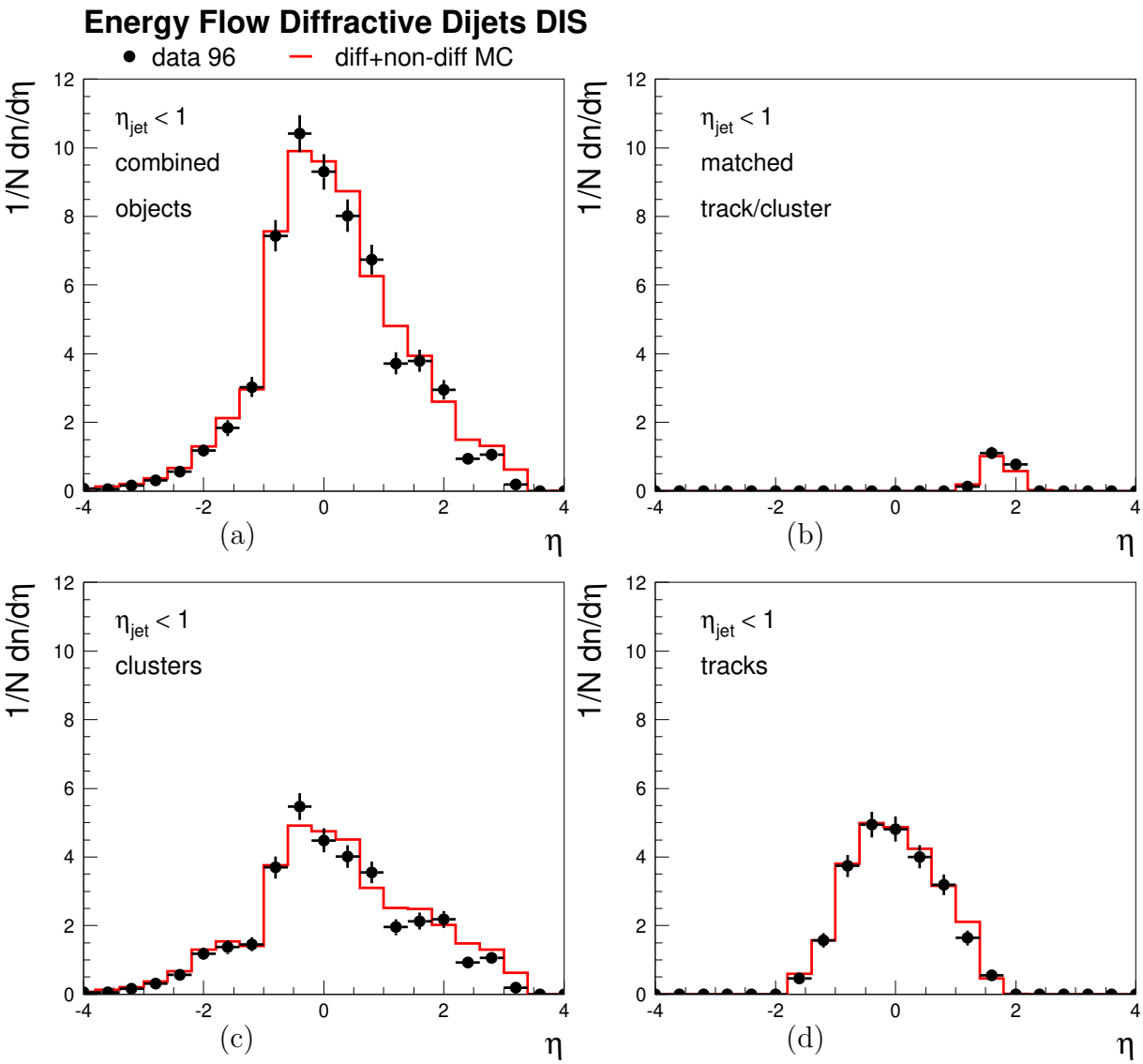

Fig. 6.20. Multiplicity for the diffractive DIS dijet sample in 96. Shown is as a function of the pseudorapidity η in the laboratory frame the average number of (a) combined objects from tracks and calorimeter clusters, (b) matched tracks and clusters, (c) clusters, and (d) tracks. The jets are required to satisfy $\eta_{\text{jet}} < 1$.

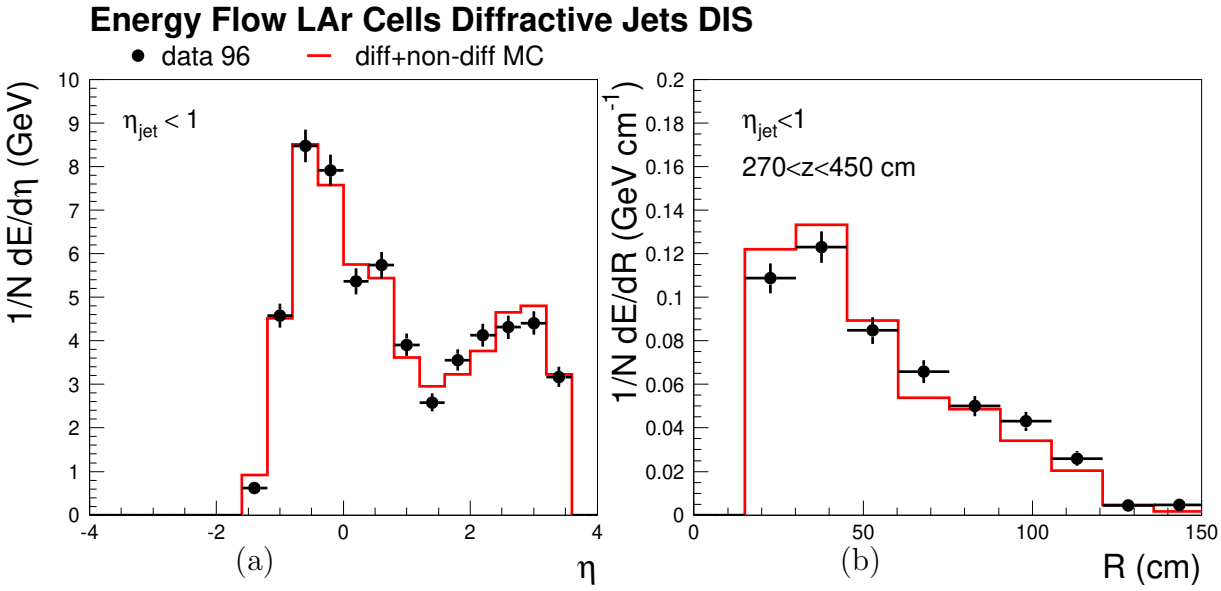

Fig. 6.21. Average LAr calorimeter cell energy per diffractive dijet event in 96 in the laboratory frame as a function of (a) the pseudorapidity η, and (b) the radial distance R from the beam axis for the forward part of the LAr calorimeter ($270 < z < 450$ cm). The jets are required to satisfy $\eta_{\text{jet}} < 1$.

6.5.2 Correction factor, purity and stability

The correction factor C_{det} is defined as in photoproduction (cf.Sec. 5.5.2). It is shown in Fig. 6.23 for 97 together with the quantities purity and stability. The distributions for x_γ are shown in Fig. 6.24. The bins have been chosen to ensure that both purity and stability are above 25%. The values for purity and stability (and therefore for the correction factor) are determined by the migrations due to detector effects. The influence of the various cuts applied in the analysis is studied in detail in Sec. 6.5.3. The most important effect are the migrations across the jet p_T threshold.

6.5.3 Cut monitoring

The cuts applied to isolate the diffractive dijet events are studied with the diffractive model. Shown in Fig. 6.25 are the numbers for the pomeron component of the diffractive Monte Carlo for 97. The largest migrations are seen across the p_T^{jet1} and $x_{I\!P}$ cuts. Concerning the jet p_T, the situation is similar to the photoproduction case. For 37% of the events in which a dijet system according to the criteria in Tab. 5.2 is identified at the hadron level, the jet requirements are not met at the detector level. Less migrations are seen in the opposite direction. For 22% of the events for which a dijet system was found at the detector level, no corresponding jets are seen at the hadron level. The inefficiency of the gap selection is 19%. As in photoproduction, a 30% uncertainty is assumed on this value. See Sec. 5.5.4 for a discussion. The most inefficient forward cut is $x_{I\!P} < 0.03$

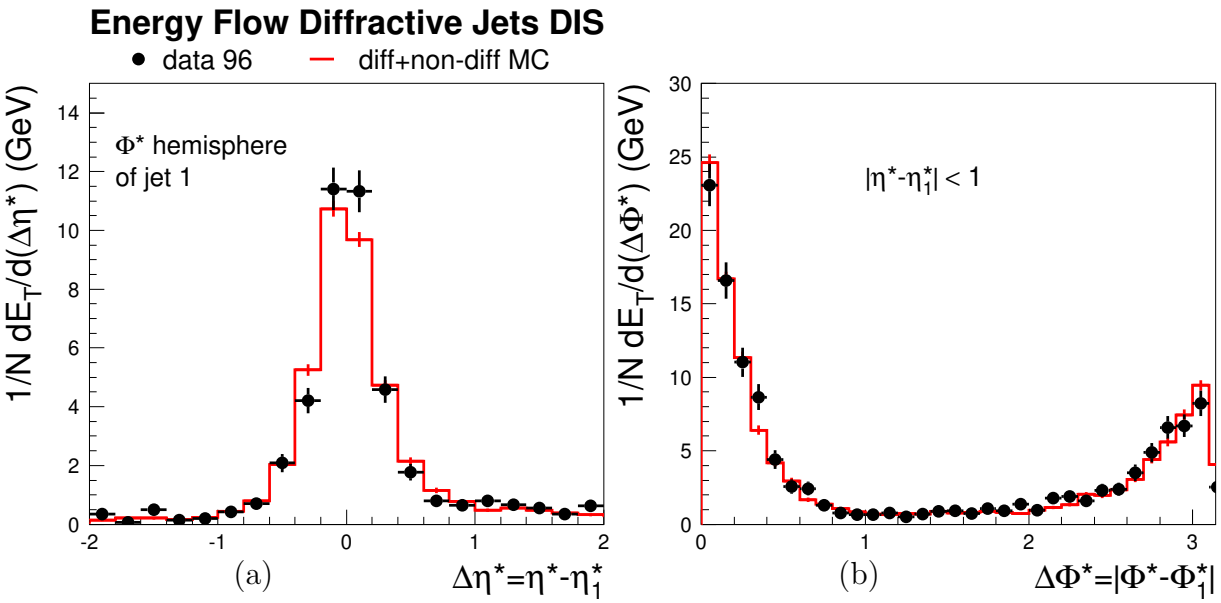

Fig. 6.22. Jet profiles for the diffractive dijet sample of 96 in the $\gamma^* p$ frame. Shown is the mean transverse energy per event around the leading jet as a function of (a) the pseudorapidity distance and (b) the distance in the azimuthal angle Φ^* with respect to the leading jet. For (a), only energy in the Φ^* hemisphere of the leading jet is taken into account. For (b), only energy within a pseudorapidity band $\eta^* \pm 1$ around the leading jet is considered.

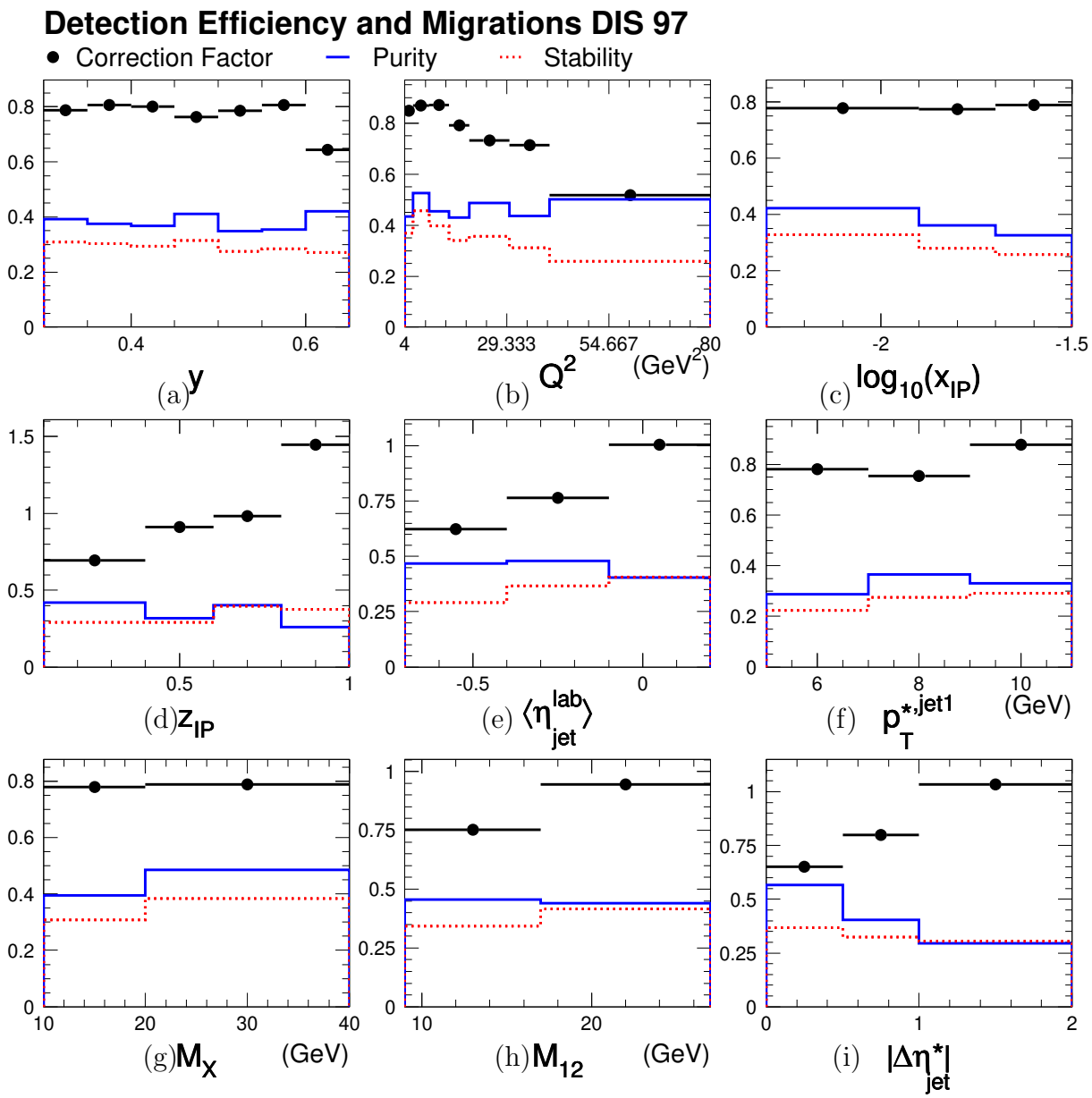

Fig. 6.23. Correction factor C_{det}, purity and stability for 97.

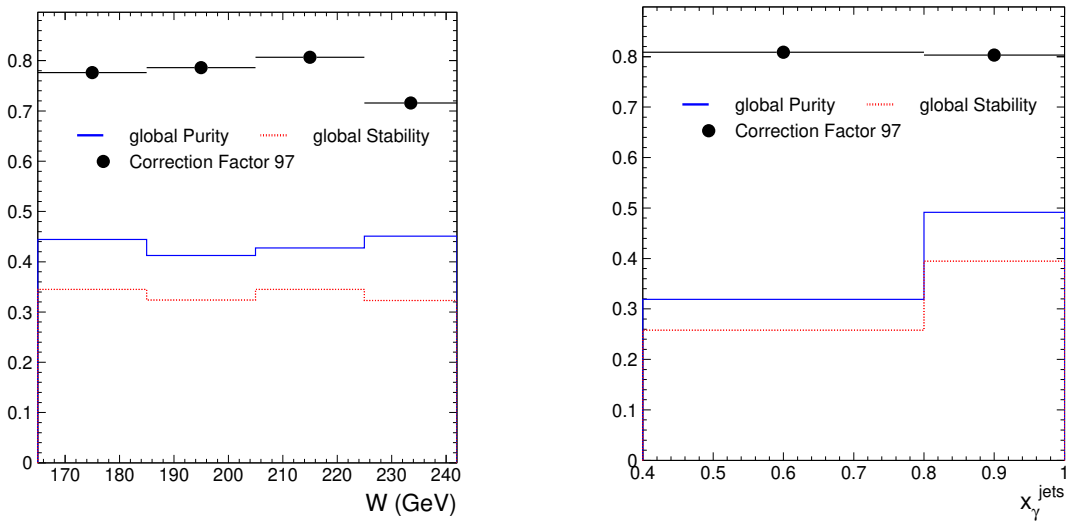

Fig. 6.24. Correction factor C_{det}, purity and stability for the spectrum of the variable (a) W and (b) x_γ evaluated with the diffractive DIS model for 97.

(-11%). This stems from the fact that $x_{I\!P}$ is reconstructed too small at the detector level for larger values of $x_{I\!P}$ (Fig. 6.1c). This effect is also visible for the migrations in reggeon exchange processes (Fig. 6.26). Dramatic migrations are seen across the cut $x_{I\!P}^{\mathrm{had}} < 0.03$. Due to the non-diagonal correlation for $x_{I\!P}$, the contribution of reggeon processes is 5% at the hadron level more than twice as large (11%) at the detector level.

The cut monitoring values for 96 are similar to 97. A difference occurs because in 96 more significant fiducial cuts had to be applied in the SPACAL. This leads to a reduced electron detection efficiency. Compared to 97, the efficiency is reduced by approximately 5%.

6.5.4 Inefficiency of the rapidity gap selection

It was shown in the cut monitoring tables, that the cuts applied to require a rapidity gap reject diffractive events. The cuts on $x_{I\!P}$, η_{max} and the forward muon and PRT detectors reject approximately 20% of the events with an exchanged pomeron. These events are rejected because they deposit energy in the forward region. The uncertainty on this inefficiency has been evaluated in [41] and was found to be approximately 30%. For the present analysis this translates into a 6% systematic error on the cross section. See Sec. 5.5.4 for a detailed discussion.

6.5.5 Correction for noise in the FMD and proton dissociation

To correct the cross section for events lost due to noise in the FMD, the same correction factor C_{FMD} as in the photoproduction analysis is used because the same cuts are applied in the forward region. See Sec. 5.5.5 for the discussion of the factor.

Cut monitoring pomeron 97

cut	N_event	reduction (%)
all hadron cuts	3167.7	---
+ SPACAL fiducial cuts	3088.5	2.5
+ ptjet>5,4 GeV	1948.2	36.9
+ -1 < etaˆlab_jet < 2	1777.8	8.7
+ 4 < Q2 < 80 GeV2	1770.4	0.4
+ |zvtx| < 35 cm	1766.7	0.2
+ E - pz < 35 GeV	1763.1	0.2
+ d(cluster-beam pipe) > 9 cm	1763.1	0.0
+ cluster radius < 3.5 cm	1700.3	3.6
+ E_spacal had in ring < 0.5 GeV	1696.5	0.2
+ E_spacal veto layer < 1.0 GeV	1695.1	0.1
+ d(closest BDC hit) < 3.0 cm	1676.2	1.1
+ E_electron > 8.0 GeV	1676.2	0.0
+ 156 < theta_electron < 176 deg	1661.8	0.9
+ 165 < W < 242 GeV	1592.8	4.1
+ x_pom < 0.03	1420.6	10.8
+ eta_max < 3.2	1307.8	7.9
+ FMD hit pairs < 2	1302.6	0.4
+ PRT hits = 0	1294.5	0.6

hadron cuts applied, detector cuts applied

cut	N_event	increase (%)
all hadron + detector cuts	1296.5	---
- -t < 1 GeV2	1297.0	0.0
- M_Y < 1.6 GeV	1297.0	0.0
- x_pom < 0.03	1456.8	12.3
- -3 < etaˆ*_jet < 0	1691.5	16.1
- pT*_jet(1,2) > 5,4 GeV	2067.4	22.2
- 165 < W < 242 GeV	2256.7	9.2
- 4 < Q2 < 80 GeV2	2321.8	2.9

Fig. 6.25. Cut monitoring for the diffractive MC in 97. The numbers refer to the pomeron component of the MC.

Cut monitoring reggeon 97

cut	N_event	reduction (%)
all hadron cuts	162.4	---
+ SPACAL fiducial cuts	158.8	2.2
+ ptjet>5,4 GeV	94.6	40.4
+ -1 < eta^lab_jet < 2	89.4	5.5
+ 4 < Q2 < 80 GeV2	87.7	1.9
+ |zvtx| < 35 cm	87.7	0.0
+ E - pz < 35 GeV	87.7	0.0
+ d(cluster-beam pipe) > 9 cm	87.7	0.0
+ cluster radius < 3.5 cm	80.3	8.4
+ E_spacal had in ring < 0.5 GeV	80.3	0.0
+ E_spacal veto layer < 1.0 GeV	80.3	0.0
+ d(closest BDC hit) < 3.0 cm	77.9	3.0
+ E_electron > 8.0 GeV	77.9	0.0
+ 156 < theta_electron < 176 deg	77.9	0.0
+ 165 < W < 242 GeV	67.2	13.8
+ x_pom < 0.03	55.1	18.1
+ eta_max < 3.2	45.2	17.9
+ FMD hit pairs < 2	45.2	0.0
+ PRT hits = 0	45.2	0.0

hadron cuts applied, detector cuts applied

cut	N_event	increase (%)
all hadron + detector cuts	45.2	---
- -t < 1 GeV2	45.2	0.0
- M_Y < 1.6 GeV	59.3	31.0
- x_pom < 0.03	183.3	209.4
- -3 < eta^*_jet < 0	204.8	11.7
- pT*_jet(1,2) > 5,4 GeV	263.3	28.5
- 165 < W < 242 GeV	280.4	6.5
- 4 < Q2 < 80 GeV2	298.1	6.3

Fig. 6.26. Cut monitoring for the diffractive MC in 97. The numbers refer to the reggeon component of the MC.

For the correction of the smearing of proton dissociation events across $M_Y = 1.6$ GeV, the same factor C_{M_Y} is used as in the photoproduction case (cf. Sec. 5.5.6). This factor has originally been evaluated in an analysis of diffractive dijets in DIS [37].

6.5.6 Radiative corrections

Before or after interacting with the proton, the electron can radiate real photons (initial or final state Bremsstrahlung). The cross sections presented here will not include this radiation. The effect is corrected for to ease comparisons with model predictions.

The correction factor C_{det} was calculated from the RAPGAP model with QED radiation enabled at both the detector and the hadron level. An additional factor C_{QED} is therefore needed which is calculated with the diffractive RAPGAP model. It is defined as

$$C_{\mathrm{QED}} = \frac{\sigma^{\mathrm{norad}}}{\sigma^{\mathrm{rad}}},$$

in which σ^{rad} and σ^{norad} are the hadron level cross sections for diffractive dijet production with and without QED radiation in the kinematic range of the measurement listed in Tab. 7.2. The QED correction factor is shown in Fig. 6.27. Within the statistical errors of the Monte Carlo events, the factor is compatible with unity. It is ensured that the statistical error is small compared to the statistical error of the data. The factor was calculated from a sample of Monte Carlo events corresponding to a luminosity of ≈ 800 pb^{-1}.

6.6 Systematic uncertainties

6.6.1 Incomplete understanding of detector parameters

The following sources of systematic uncertainties related to incomplete detector understanding are considered.

- **Hadronic LAr energy scale**
  The energy scale of the hadronic part of the LAr calorimeter has been varied by $\pm 4\%$. This leads to changes of the cross section of 4%. The influence of the hadronic LAr energy scale is reduced in DIS because of an interplay of the jet transverse momentum p_T cut and the diffractive $x_{I\!P}$ cut. If the LAr energy is larger, then the jets will generally have more p_T and more jets will be found across the p_T threshold. However, also M_X will be larger and this results in a larger value for $x_{I\!P}$ according to (2.4). The quantities Q^2 and W in (2.4) are reconstructed from the scattered electron and are not affected by the change of the LAr scale. Events will therefore be lost due to the cut $x_{I\!P} < 0.03$. These two effects cancel to large extend. In photoproduction, the p_T effect dominates over the diffractive cut. This is due to $x_{I\!P}$ being reconstructed differently (cf. (5.2)).

- **Hadronic SPACAL energy scale**
  The energy scale of the hadronic part of the SPACAL is known within 7%. This gives rise to variations of the cross section of approximately 1%.

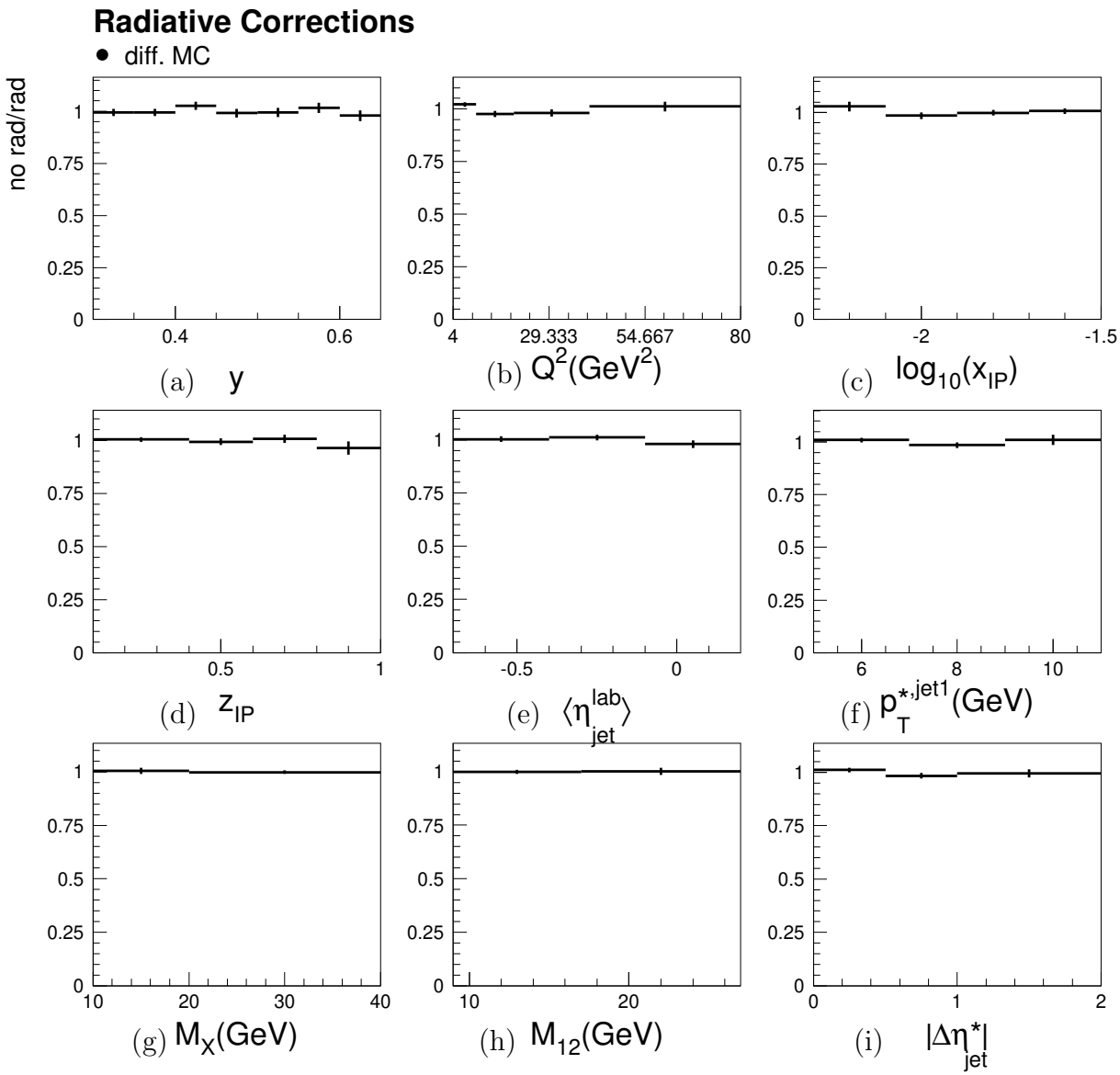

Fig. 6.27. QED radiative corrections. The correction factor $C_{\mathrm{QED}} = \sigma^{\mathrm{norad}}/\sigma^{\mathrm{rad}}$ is shown for the variables (a) y, (b) Q^2, (c) $\log_{10}(x_{I\!P})$, (d) $z_{I\!P}$, (e) $\langle\eta^{\mathrm{lab}}_{\mathrm{jet}}\rangle$, (f) p_T^{jet1}, (g) M_X, (h) M_{12} and (i) $|\Delta\eta_{\mathrm{jet}}|$

- **Track momenta in combined objects**
  A 3% uncertainty of the contribution of track momenta to the combined objects results in cross section errors of around 3%.

- **Electron scattering angle**
  A 1 mrad uncertainty in the θ_e measurement translates into a 2% cross section uncertainty.

- **Electron energy**
  The uncertainty of the electron energy measured in the SPACAL is 0.3% for $E'_e =$ 27.5 GeV and 2% for $E'_e = 8$ GeV with a linear interpolation inbetween. The uncertainty leads to variations of the cross of 4–5%.

- **Luminosity measurement**
  The luminosity measurement is accurate within 2%. This translates directly into an error on the cross section of 2%.

- **Trigger efficiency parameterisation**
  As was shown in Sec. 6.3.2, the parameterisation of the trigger efficiency can describe the efficiency determined from the data within 5%. This gives rise to an uncertainty of the cross section of 6%.

The errors on the energy scale, the track momenta and electron detector are evaluated with the diffractive Monte Carlo model. They affect the calculation of the correction factor C_{det}. The error of C_{det} translates directly into an error of the cross section (cf. (6.5)).

6.6.2 Imperfect description of data distributions

The following uncertainties result from the imperfect Monte Carlo modelling of the data distributions.

- **Inefficiency of the rapidity gap selection**
  A 30% uncertainty is assumed for the RAPGAP correction of the rapidity gap inefficiency. This value translates into a 6% systematic uncertainty on the cross section.

- **Number of migrations from $\mathbf{x_{I\!P}^{had} > 0.2}$**
  The amount of migrations from large $x_{I\!P}$ is determined by the normalisation of the non-diffractive Monte Carlo model. The normalisation of the model is varied by 50% leading to cross section changes of 3%. The largest influence (4%) is seen in the highest $x_{I\!P}$ bin where the non-diffractive model contributes most.

- **Shapes of Monte Carlo spectra**
  To evaluate the uncertainty of C_{det}, the shapes of the Monte Carlo are varied within the statistical errors of the data. The following kinematic distributions are varied:

  – $x_{I\!P}$ by ${x_{I\!P}}^{\pm 0.3}$

- $\hat{p}_T$ by $\hat{p}_T^{\pm 0.5}$
- t by $e^{\pm 2t}$
- y by $y^{\pm 0.5}$

The reweighting gives rise to cross section errors in the range of several percent. The largest deviation (9%) is due to the $x_{I\!P}$ reweight. The influence of the $x_{I\!P}$ reweighting is shown in Fig. 6.28. The variable $z_{I\!P}$ is correlated with $x_{I\!P}$ according to (2.7). Beyond the change observed due to the $x_{I\!P}$ reweight, no explicit variation of $z_{I\!P}$ is necessary.

- **Migrations across $\mathbf{M_Y = 1.6}$ GeV**
  The 7% uncertainty of the correction factor C_{M_Y} translates directly into a 7% systematic error for the cross section.

- **FMD noise correction**
  The uncertainty in the determination of the noise fraction π for the FMD (25%) translates into a 1.3% error for C_{FMD} which is also the uncertainty for the cross section.

The dominant systematic uncertainty on the cross section results from the reweighting of the correction Monte Carlo in $x_{I\!P}$. The total systematic uncertainty is approximately 15%. The statistical uncertainty of the measurement is in the range of 10%. For individual bins the statistical uncertainty can be significantly higher than the systematic uncertainty.

6.7 Summary

In this chapter, the selection of dijet events in diffractive DIS was presented. It was shown that the rate at which these events are measured is stable over the run periods considered in the analysis when the trigger inefficiency is taken into account. It was shown that the shapes of the event variable distributions can be described by LO Monte Carlo generated events which are based on diffractive parton densities as obtained in inclusive diffractive DIS. The energy flow per event is described by the Monte Carlo model. A correction factor to the level of stable hadrons was determined from the Monte Carlo. The largest migrations where seen to be due to the jet threshold p_T cut. The resulting cross sections are shown in Chap. 7 where they are compared with model predictions. The average event numbers and correction factors are listed in Tab. 6.2. The analysis was performed separately for 96 and 97 to check the consistency between the results obtained in the different years. The total cross sections for 96 and 97 agree within 7% which is much smaller than the statistical and systematic uncertainties of the measurements.

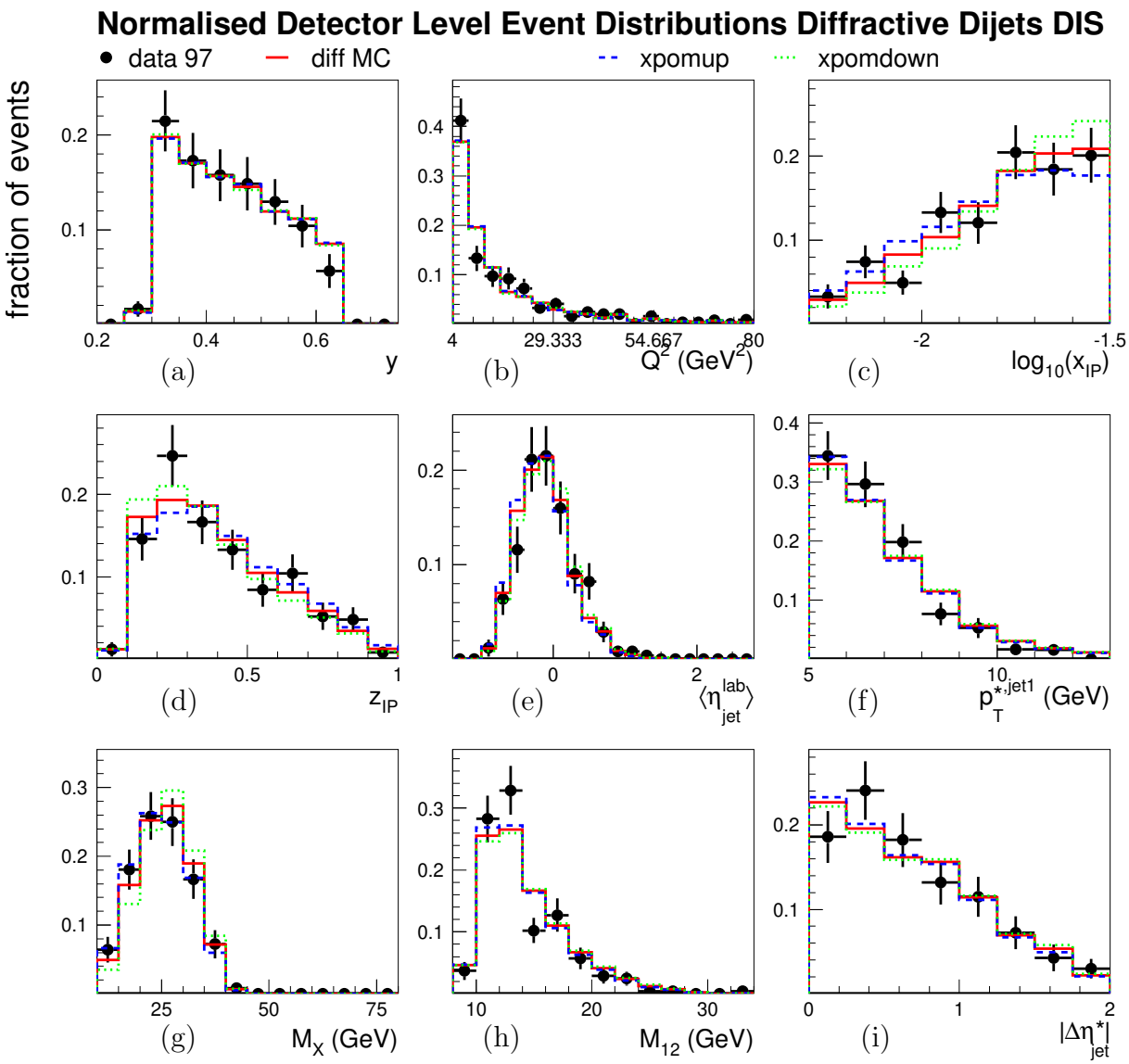

Fig. 6.28. Normalised event distributions for the diffractive DIS dijet sample for 97. Shown are variations of the diffractive Monte Carlo. The solid histogram is the central MC. The dashed (dotted) histogram is obtained by weighting every MC event by ${x_{I\!P}}^{0.3}$ (${x_{I\!P}}^{-0.3}$).

Quantity	**96**	**97**	$\frac{\mathbf{97-96}}{\mathbf{97}}$	**Comment**
L (pb^{-1})	5.44	10.14		
N_{raw}	101	221		
L1 prescale	1.0	1.12		
$N_{\mathrm{data}} \equiv N_{\mathrm{raw}} \times$L1 prescale	101	248		
$\varepsilon_{\mathrm{trig}}$	0.90	0.93	0.031	
$N_{\mathrm{non-diffr}}$	4.56	15.94		
$\frac{N_{\mathrm{non-diffr}}}{N_{\mathrm{data}}/\varepsilon_{\mathrm{trig}}}$	0.041	0.060		
C_{det}	0.70	0.79	0.110	different fiducial SPACAL cuts
C_{M_Y}	0.96	0.924	-0.039	degrading PRT efficiency
C_{FMD}	1.055	1.055		
C_{QED}	1.00	1.00		
N_{data}/L (pb)	18.57	24.46	0.241	
$N_{\mathrm{data}}/(\varepsilon_{\mathrm{trig}}\, L)$ (pb)	20.60	26.31	0.217	
$\frac{N_{\mathrm{data}}/\varepsilon_{\mathrm{trig}} - N_{\mathrm{non-diffr}}}{L}$ (pb)	19.77	24.74	0.201	
$\frac{N_{\mathrm{data}}/\varepsilon_{\mathrm{trig}} - N_{\mathrm{non-diffr}}}{C_{\mathrm{det}}\, L}$ (pb)	28.24	31.45	0.102	
$\frac{N_{\mathrm{data}}/\varepsilon_{\mathrm{trig}} - N_{\mathrm{non-diffr}}}{C_{\mathrm{det}}\, L}\, C_{M_Y}$ (pb)	27.11	29.06	0.067	
$\frac{N_{\mathrm{data}}/\varepsilon_{\mathrm{trig}} - N_{\mathrm{non-diffr}}}{C_{\mathrm{det}}\, L}\, C_{M_Y}\, C_{\mathrm{FMD}}\, C_{\mathrm{QED}}$ (pb)	28.62	30.68	0.067	

Tab. 6.2. Average event numbers and correction factors for the DIS analysis. The numbers in the last line correspond to the total diffractive dijet cross section.

Chapter 7

Results and interpretation

In this chapter, the cross sections are presented for diffractive dijet production in photoproduction and DIS. The cross sections are shown as a function of a number of characteristic variables. In all figures, the inner error bars represent the statistical uncertainty of the data and the outer error bars show the quadratic sum of the statistical and systematic errors. The shaded band indicates an additional correlated normalisation uncertainty which includes the uncertainties on the calorimeter energy scales (only SPACAL for DIS), the non-diffractive background, the forward gap selection, the smearing across $M_Y = 1.6$ GeV, the FMD noise and the luminosity calculation. The measured distributions are compared with LO predictions of the RAPGAP [5] implementation of the pomeron model using LO pomeron parton densities and the pomeron flux factor obtained in DGLAP QCD fits to inclusive diffractive DIS data. The H1 2002 fit is used as the best representation of recent data [3]. LO matrix elements for the hard QCD 2→ 2 subprocess are convoluted with the LO parton distributions of the pomeron and the photon, taken at the scale $\mu = \sqrt{\hat{p}_T^2 + m_{q\bar{q}}^2}$, where $\hat{p}_T$ is the transverse momentum of the emerging hard partons and $m_{q\bar{q}}$ is the mass of the produced quarks.

The strong coupling constant α_s is calculated with $\Lambda_{\rm QCD} = 0.2$ GeV for 4 flavours. The same value was used in the QCD fit extraction of the pomeron parton densities and for the LO PDFs of the photon that are used in photoproduction and DIS. The maximum number of flavours for α_s is set to 5.

Higher order effects are simulated using parton showers [6] in the leading $\log(\mu)$ approximation (MEPS), and the Lund string model [7] is used for hadronisation.

A small contribution from reggeon exchange is also simulated using the corresponding reggeon flux parameterisation from the pomeron PDF extraction and parton density functions of the pion [8].

Kinematic range of the γp cross section

$Q^2 < 0.01$ GeV^2
$165 < W < 242$ GeV
inclusive k_T jet algorithm
distance parameter 1.0
$N_{\text{jet}} \geq 2$
$E_T^{\text{jet(1)}} > 5$ GeV
$E_T^{\text{jet(2)}} > 4$ GeV
$-1 < \eta^{\text{lab}}_{\text{jet(1,2)}} < 2$
$x_{I\!P} < 0.03$
$M_Y < 1.6$ GeV
$-t < 1$ GeV^2

Tab. 7.1. Definition of the kinematic range of the diffractive photoproduction dijet cross section.

7.1 Dijet cross sections in diffractive photoproduction

The kinematic range of the photoproduction measurement is listed in Tab. 7.1. For the model prediction, the photon structure is given by the LO GRV photon parton distributions [9], which describe well the measured effective photon structure [10].

7.1.1 Total diffractive dijet cross section in photoproduction

The total diffractive dijet cross section is presented in Fig. 7.1. The measured result is

$$\sigma_{\text{tot}} = 243 \text{ pb} \pm 3\% \text{ (stat.)} \pm 13\% \text{ (syst.)}. \tag{7.1}$$

The prediction of the RAPGAP pomeron model based on the H1 2002 fit pomeron densities as obtained in inclusive DDIS predicts a cross section of

$$\sigma_{\text{tot}} = 228 \text{ pb}. \tag{7.2}$$

This value is indicated by the line in Fig. 7.1. The prediction is compatible with the measured cross section. The ratio of prediction to measurement in photoproduction is

$$\left.\frac{\text{model}}{\text{data}}\right|_{\gamma p} = 0.93 \pm 13\% \text{ (exp.)}. \tag{7.3}$$

The uncertainty is estimated from the total uncertainty of the measurement only. No model uncertainties are considered. Within the uncertainty, the measurement is consistent with QCD and Regge factorisation. Sub-leading reggeon exchange is predicted to contribute at $\approx 6\%$ and is indicated in Fig. 7.1 by the hatched histogram.

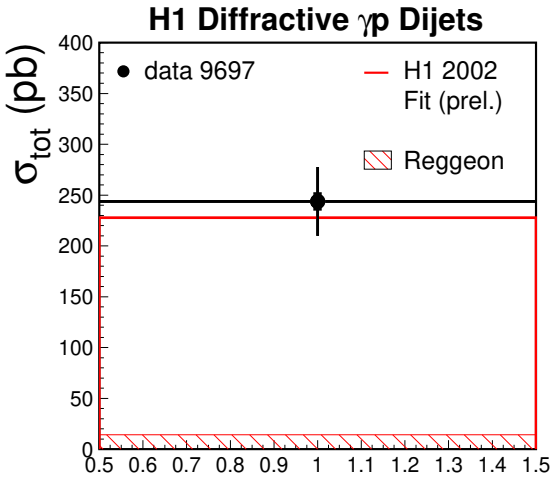

Fig. 7.1. The total cross section of the diffractive production of dijets in the photoproduction kinematic region specified in Tab. 7.1. The inner error bars represent the statistical errors and the outer error bars the quadratic sum of the statistical and systematic errors. Also shown is the LO prediction of the RAPGAP model with LO pomeron parton densities from the H1 2002 fit. The contribution of reggeon exchange processes is indicated by the hatched histogram.

7.1.2 Dependence on the fractional momenta x_γ, $z_{I\!P}$ and $x_{I\!P}$

The cross section as a function of the estimator x_γ^{jets} of the fractional parton momentum from the photon taking part in the hard scattering is presented in Fig. 7.2. The prediction based on the H1 2002 fit pomeron densities gives a very good description of the distribution. The contribution from direct photon processes (x_γ^{true}=1) is indicated by the hatched histogram. These interactions dominate the dijet cross section for $x_\gamma^{\text{jets}} > 0.6$. According to the model, approximately 50% of the total dijet cross section is due to direct photon processes.

The cross section differential in the estimator $z_{I\!P}^{\text{jets}}$ of the fractional parton momentum from the diffractive exchange is presented in Fig. 7.3. Because the pomeron is gluon dominated this distribution is effectively the gluon density in the pomeron. The prediction gives a good description of the $z_{I\!P}$ distribution.

In Fig. 7.4, the cross section is shown as a function of $x_{I\!P}$. The prediction gives a good description of the measurement.

7.1.3 Dependence on jet variables

The cross section is studied for jet variables in Fig. 7.5. The dependence on p_T^{jet1} is shown in Fig. 7.5a. The cross section is shown as a function of $\langle\eta_{\text{jet}}^{\text{lab}}\rangle$, $|\Delta\eta_{\text{jet}}|$, and M_{12} in Figs. 7.5b, c, and d, respectively. Within the statistical uncertainties of the data the pomeron model based on the H1 2002 fit pomeron parton densities gives a very good description of all distributions.

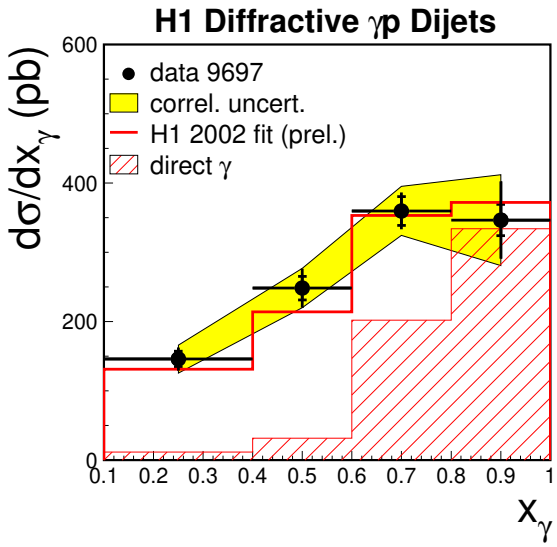

Fig. 7.2. Cross section differential in x_γ^{jets}. The inner error bars represent the statistical errors and the outer error bars the quadratic sum of the statistical and uncorrelated systematic errors. The shaded band shows correlated normalisation uncertainties of the data. Also shown is the LO prediction of the RAPGAP model with LO pomeron parton densities from the H1 2002 fit. The direct photon contributions from boson gluon fusion and QCD compton processes are indicated by the hatched histogram. The LO GRV parton distributions of the photon are used.

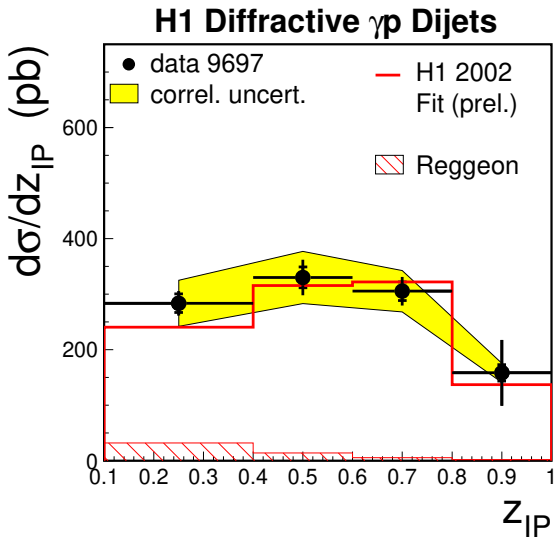

Fig. 7.3. Cross section differential in $z_{I\!P}^{\text{jets}}$. Also shown are LO predictions of the RAPGAP model with LO pomeron parton densities from the H1 2002 fit.

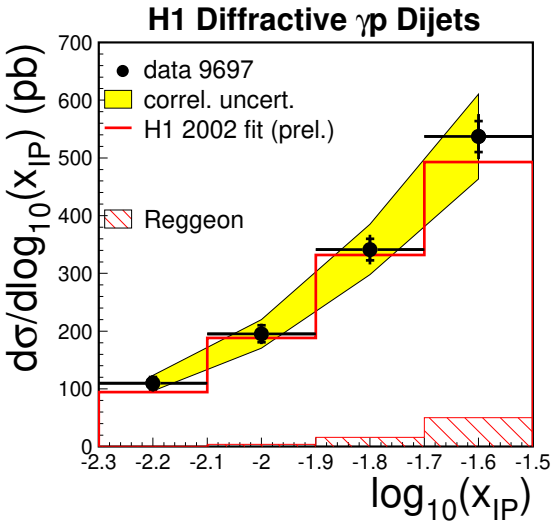

Fig. 7.4. Cross section differential in $\log_{10}(x_{I\!P})$ for diffractive dijet photoproduction. Also shown are LO predictions of the RAPGAP model with LO pomeron parton densities from the H1 2002 fit. The sub-leading Reggeon contribution is shown as the hatched histogram.

7.1.4 Dependence on other variables

The cross section is studied for further variables in Fig. 7.6. The dependence on the fractional photon momentum y, the photon-proton centre-of-mass energy W and M_X is shown in Figs. 7.6a, b and c, respectively. The prediction based on the H1 2002 fit pomeron parton densities describes the measured distributions very well within the uncertainty of the data.

7.1.5 Uncertainties of the model prediction

The pomeron gluon density at the LO is used in the predictions. The uncertainty of the gluon density at the NLO is shown in Fig. 2.3. The uncertainty is $\approx 25\%$ at for $z_{I\!P} \approx 0.5$ and increases to more than 50% for $z_{I\!P} > 0.7$.

The parameterisation of the photon structure has been varied within the experimental constraints, leading to negligible changes of the predicted cross sections. Variations of the renormalisation and factorisation scale μ by a factor 2 and 0.5 lead to changes in the predicted cross sections of about 20%. The variations are shown in Fig. 7.7. They have been evaluated with the POMPYT Monte Carlo program. It was not possible to obtain a reliable prediction from RAPGAP. Discrepancies are visible in the cross sections shown in Fig. 7.7 between the predictions of POMPYT and RAPGAP. They are due to a different prediction for the y distribution which is related to the photon emission from the electron. The other variables are then affected through kinematic correlations. It was not possible to clarify the discrepancies. The predictions shown in this thesis are based on the RAPGAP model in order to have the same generator in photoproduction and DIS.

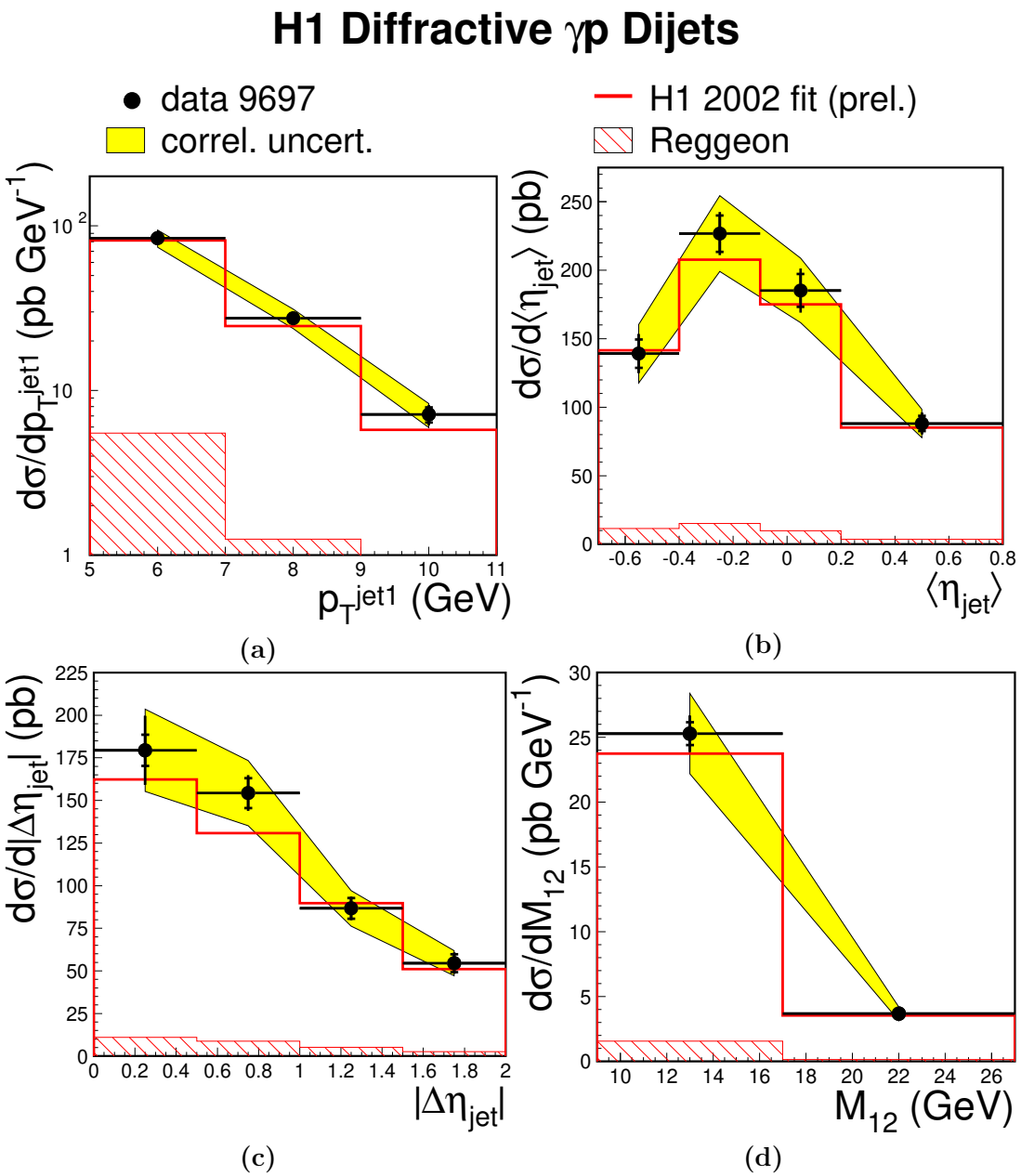

Fig. 7.5. Diffractive photoproduction dijet cross section as a function of the jet variables (a) p_T^{jet1}, (b) $\langle\eta_{\mathrm{jet}}^{\mathrm{lab}}\rangle$, (c) $|\Delta\eta_{\mathrm{jet}}|$, and (d) M_{12}. Also shown is the LO prediction of the RAPGAP model with LO pomeron parton densities from the H1 2002 fit. The contribution of reggeon exchange processes is indicated by the hatched histogram.

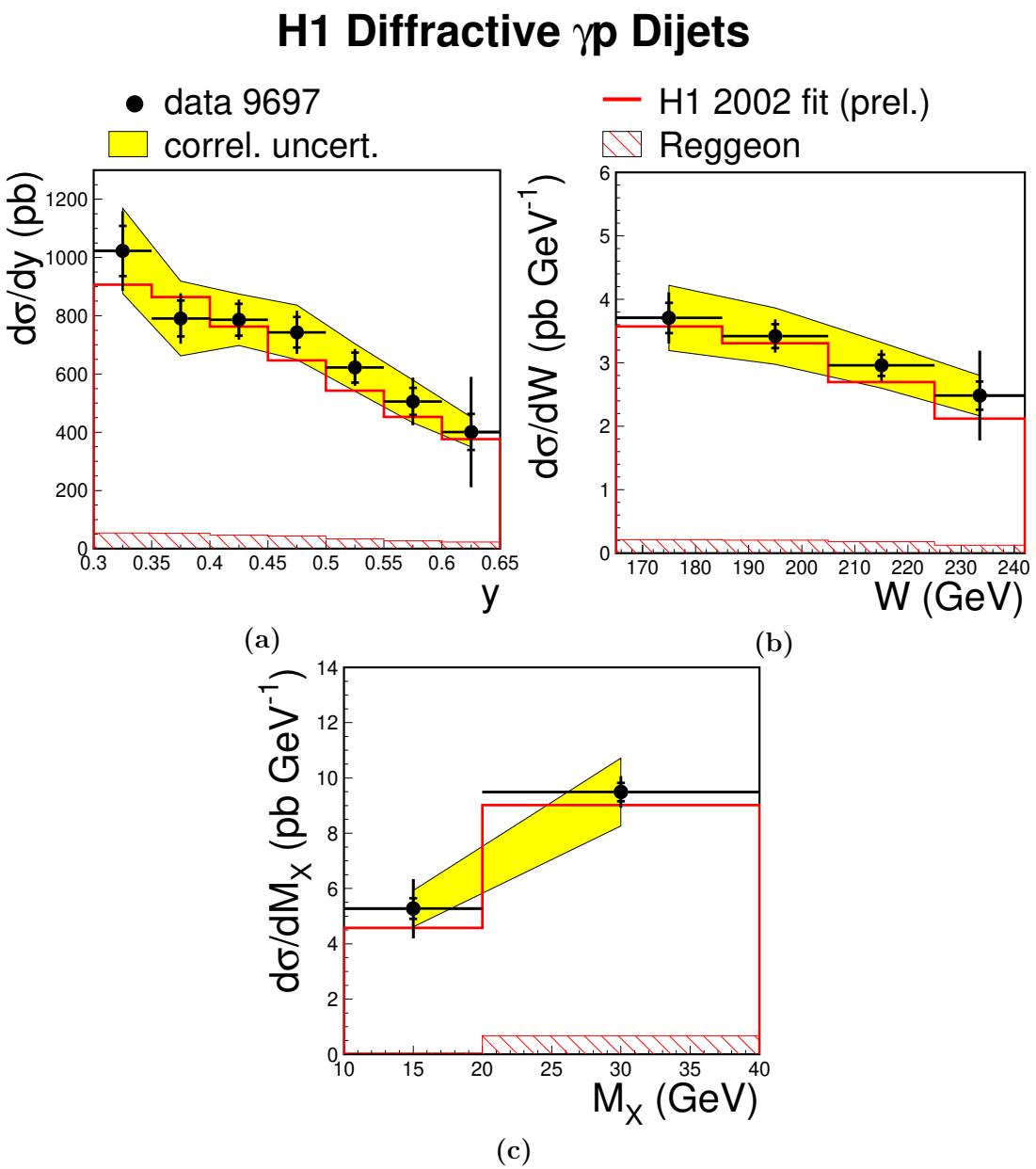

Fig. 7.6. Cross sections for the diffractive production of dijets in photoproduction as a function of (a) the fractional photon energy y, (b) the photon-proton centre-of-mass energy W, and (c) M_X. Also shown is the LO prediction of the RAPGAP model with LO pomeron parton densities from the H1 2002 fit.

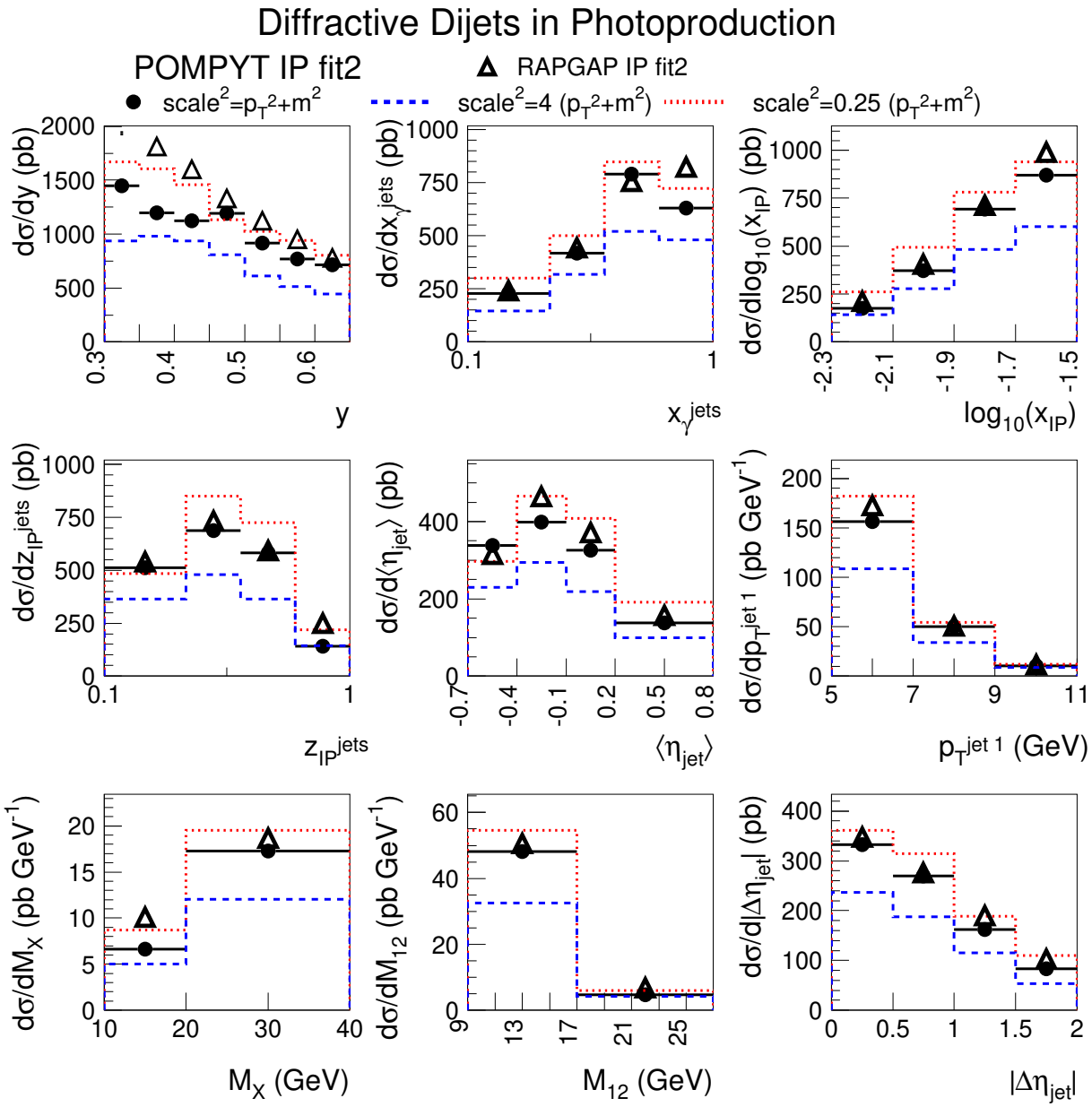

Fig. 7.7. Model predictions based on the H1 fit 2002 pomeron parton densities. Shown are predictions of the RAPGAP and the POMPYT Monte Carlo models with the factorisation and normalisation scale $\mu = \sqrt{p_T^2 + m^2}$. The POMPYT prediction is also shown with the scale varied by a factor 2 (dashed histogram) and 0.5 (dotted histogram).

Kinematic range of the DIS cross section

$4 < Q^2 < 80$ GeV^2
$165 < W < 242$ GeV
inclusive k_T jet algorithm
distance parameter 1.0
$N_{\text{jet}} \geq 2$
$E_T^{*,\text{jet1}} > 5$ GeV
$E_T^{*,\text{jet2}} > 4$ GeV
$-3 < \eta^*_{\text{jet(1,2)}} < 0$
$x_{I\!P} < 0.03$
$M_Y < 1.6$ GeV
$-t < 1$ GeV^2

Tab. 7.2. Definition of the kinematic range of the diffractive DIS dijet cross section.

7.2 Dijet cross sections in diffractive DIS

The kinematic range of the DIS measurement is listed in Tab. 7.2. The model prediction includes a small contribution from processes with a resolved virtual photon for which the photon structure is given by the SaS-2D parameterisation [11].

7.2.1 Total diffractive dijet cross section in DIS

The total diffractive dijet cross section is presented in Fig. 7.8. The measured result is

$$\sigma_{\text{tot}} = 29.9 \text{ pb} \pm 7\% \text{ (stat.)} \pm 15\% \text{ (syst.)}. \tag{7.4}$$

The prediction of the RAPGAP pomeron model based on the H1 2002 fit pomeron densities as obtained in inclusive DDIS predicts a cross section of

$$\sigma_{\text{tot}} = 24.7 \text{ pb}. \tag{7.5}$$

This value is indicated by the line in Fig. 7.8. The ratio of prediction to measurement in DIS is

$$\frac{1}{N_{\text{DIS}}} \equiv \left.\frac{\text{model}}{\text{data}}\right|_{\text{DIS}} = 0.83 \pm 17\% \text{ (exp.)}, \tag{7.6}$$

in which the uncertainty is estimated from the total uncertainty of the measurement only. Within this uncertainty, the prediction is compatible with the measurement. The measured result is therefore consistent with QCD and Regge factorisation. Sub-leading reggeon exchange is predicted to contribute at $\approx 7\%$ and is indicated in Fig. 7.8 by the hatched histogram.

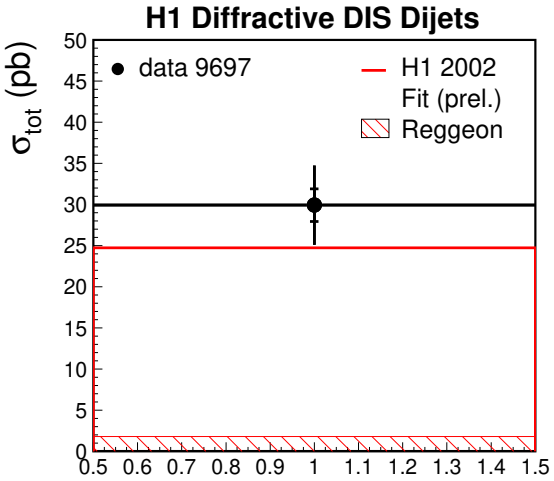

Fig. 7.8. The total cross section of the diffractive production of dijets in the DIS kinematic region specified in Tab. 7.2. Also shown is the LO prediction of the RAPGAP model with LO pomeron parton densities from the H1 2002 fit. The contribution of reggeon exchange processes is indicated by the hatched histogram.

7.2.2 Dependence on the fractional momenta x_γ, $z_{I\!P}$ and $x_{I\!P}$

The cross section as a function of the estimator x_γ^{jets} of the fractional parton momentum from the photon taking part in the hard scattering is presented in Fig. 7.9. The distribution is peaked at large x_γ which where direct photon processes contribute. Also shown is the LO prediction of the RAPGAP diffraction model based on LO pomeron parton densities obtained in inclusive DDIS and on LO SaS-2D virtual photon densities. Indicated by the hatched histogram is the contribution of direct photon processes. According to the model, the contribution of resolved photon processes is $\approx 8\%$. The description underestimates the cross section significantly for $x_\gamma < 0.7$. This cannot be attributed to a wrong photon structure because even in this x_γ region, the contribution from resolved photon processes is rather small. Instead, the discrepancy could result from NLO effects not included in the Monte Carlo prediction. This is discussed below.

The cross section differential in the estimator $z_{I\!P}^{\text{jets}}$ of the fractional parton momentum from the diffractive exchange is presented in Fig. 7.10. The distribution shows a falling behaviour. The model based on LO pomeron densities describes the distribution within the uncertainties of the measurement. The $z_{I\!P}$ distribution is effectively the gluon density in the pomeron and the agreement shows that the gluon density determined in inclusive diffractive DIS and dijet production is the same. At low values of $z_{I\!P}$, the prediction has the tendency to underestimate the cross section although this deviation is not very significant. It is however expected that the description will improve when calculations are performed at the NLO because the pomeron densities at the NLO are $\approx 20\%$ larger in the range $0.1 < z_{I\!P} < 0.5$ (cf. Fig. 2.3). Low values of $z_{I\!P}$ are kinematically correlated with low values of x_γ and large values of $x_{I\!P}$ through the requirement of a central dijet system. It is expected that also the x_γ and $x_{I\!P}$ prediction will improve at the NLO. The description would also be better in photoproduction where the same trend is observed in

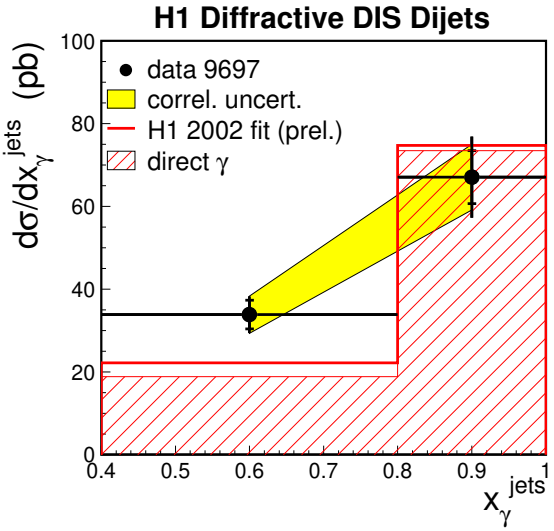

Fig. 7.9. Cross section differential in x_γ^{jets} for diffractive dijet production in DIS. Also shown is the LO prediction of the RAPGAP model with LO pomeron parton densities from the H1 2002 fit. The direct photon contributions (boson gluon fusion and QCD compton) are indicated by the hatched histogram. The LO SaS-2D parton distributions of the virtual photon are used.

x_γ, $z_{I\!P}$ and $x_{I\!P}$, although the deviation is even less significant than in DIS. However, the exact calculation at the NLO has to be awaited because the smaller value of α_s at the NLO will lead to a reduction of the dijet cross section.

In Fig. 7.11, the cross section is shown as function of $x_{I\!P}$. The H1 2002 fit prediction is also shown and gives a good description. The model has the tendency to underestimate the cross section at large $x_{I\!P}$. This regime is kinematically correlated with small $z_{I\!P}$ and the description could be improved at the NLO.

7.2.3 Dependence on jet variables

The cross section is studied for jet variables in Fig. 7.12. The dependence on $p_T^{\text{jet1},*}$ is shown in Fig. 7.12a. The distribution is exponentially falling. The pomeron model based on the pomeron parton densities extracted in the H1 fit to F_2^D data predicts a slightly flatter distribution but is compatible within the uncertainties of the measurment. The cross section is shown as a function of $\langle\eta_{\text{jet}}^{\text{lab}}\rangle$, $\left|\Delta\eta_{\text{jet}}^*\right|$, and M_{12} in Figs. 7.12b, c and d, respectively. Within the statistical uncertainties of the data the pomeron model gives a good description of the shapes of all distributions.

7.2.4 Dependence on other variables

The cross section is shown as a function of the photon virtuality Q^2, the inelasticity y, the photon-proton centre-of-mass energy W and M_X in Figs. 7.12a, b, c and d, respectively. The distributions are all described within the uncertainties of the data.

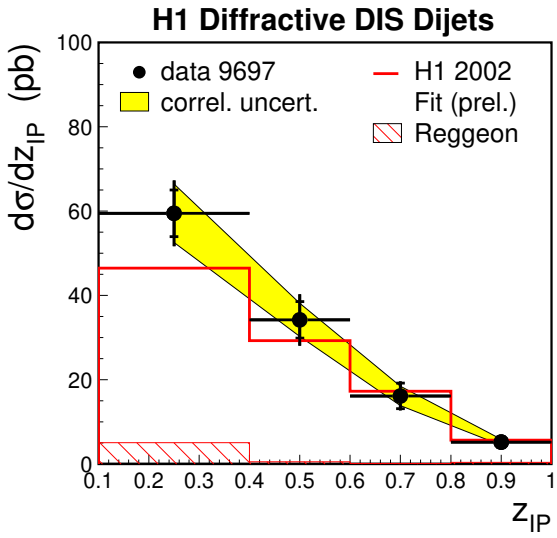

Fig. 7.10. Cross section differential in $z_{I\!P}^{\text{jets}}$ for the diffractive production of dijets in the DIS kinematic region specified in Tab. 7.2. Also shown is the LO prediction of the RAPGAP model with LO pomeron parton densities from the H1 2002 fit. The contribution of reggeon exchange processes is indicated by the hatched histogram.

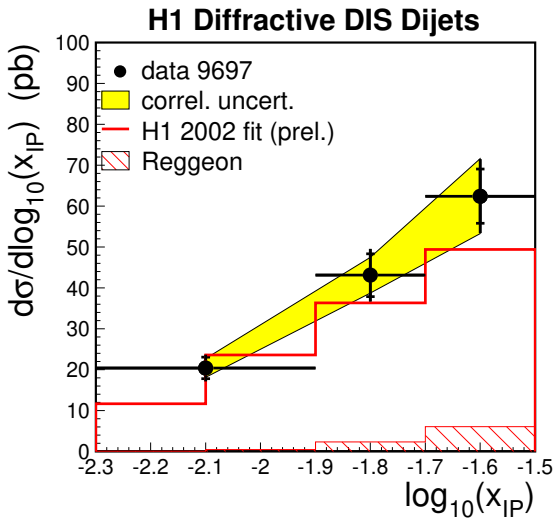

Fig. 7.11. Cross section differential in $\log_{10}(x_{I\!P})$ for diffractive dijet production in DIS. Also shown is the LO prediction of the RAPGAP model with LO pomeron parton densities from the H1 2002 fit. The contribution of reggeon exchange processes is indicated by the hatched histogram.

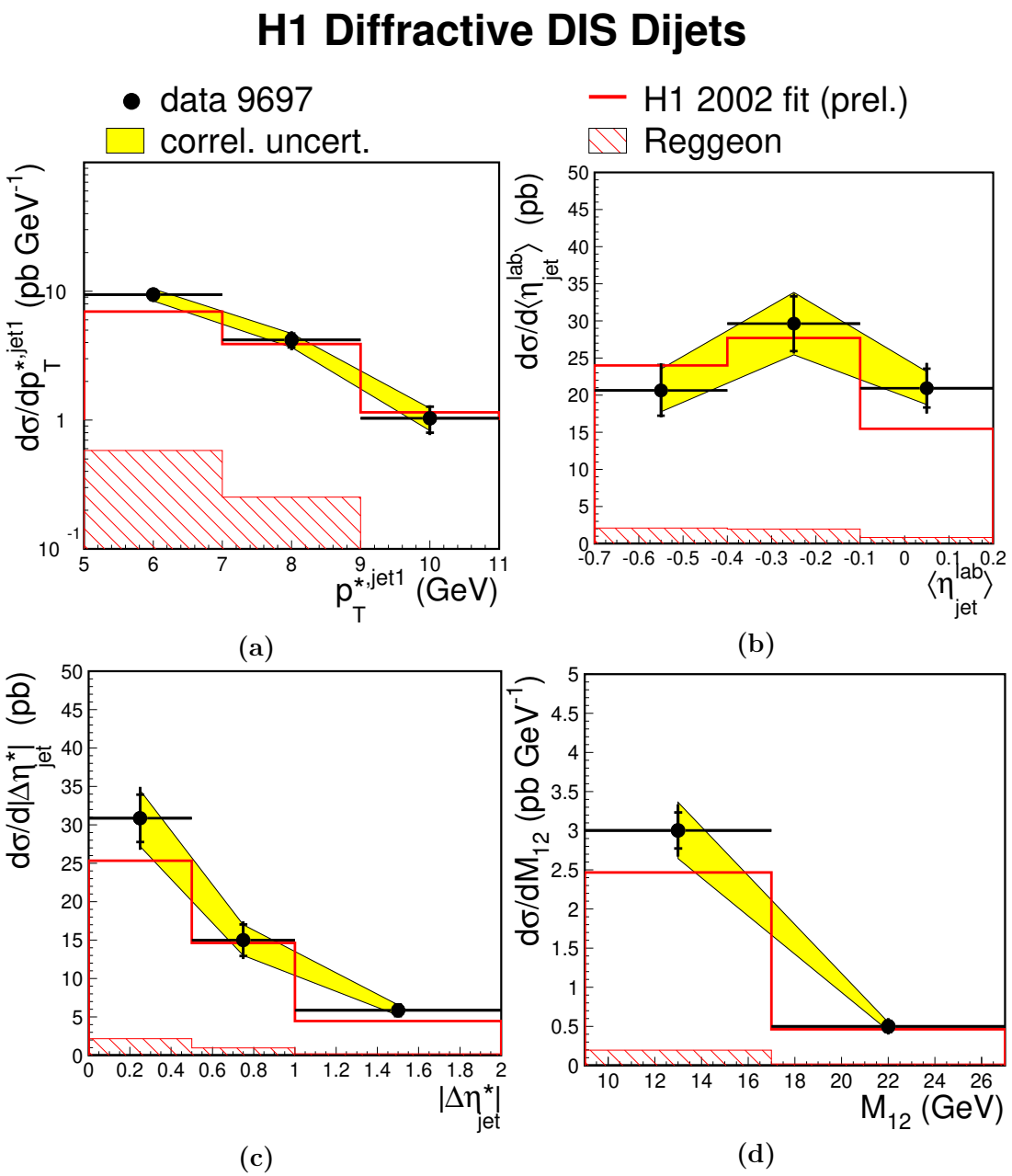

Fig. 7.12. Diffractive DIS dijet cross section as a function of the jet variables (a) $p_T^{\mathrm{jet1},*}$, (b) $\langle\eta_{\mathrm{jet}}^{\mathrm{lab}}\rangle$, (c) $\left|\Delta\eta_{\mathrm{jet}}^{*}\right|$, and (d) M_{12}. Also shown is the LO prediction of the RAPGAP model with LO pomeron parton densities from the H1 2002 fit. The contribution of reggeon exchange processes is indicated by the hatched histogram.

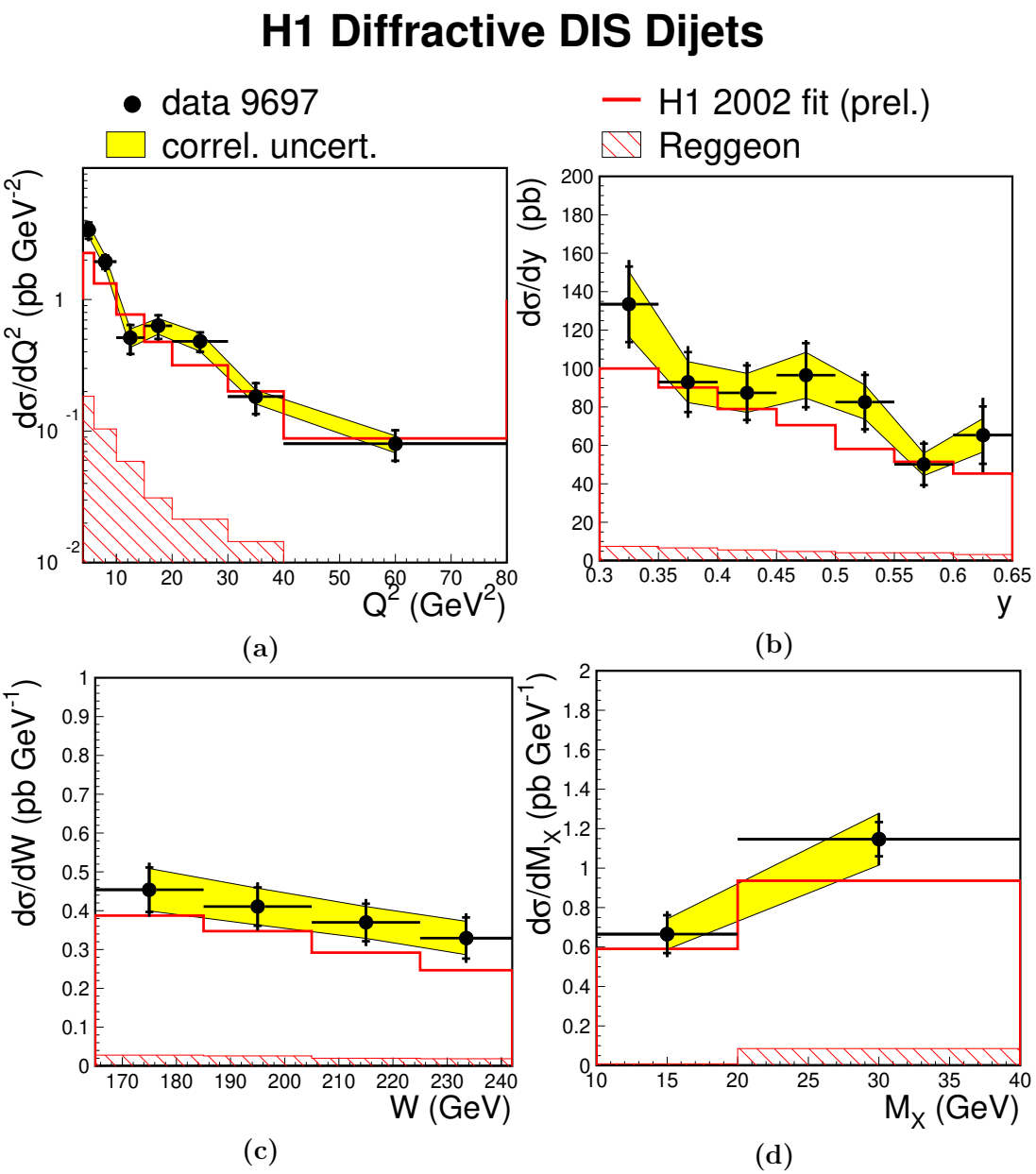

Fig. 7.13. Diffractive DIS dijet cross section as a function of (a) the photon virtuality Q^2, (b) the inelasticity y, (c) the photon-proton system centre-of-mass energy W, and (d) M_X. Also shown is the LO prediction of the RAPGAP model with LO pomeron parton densities from the H1 2002 fit. The contribution of reggeon exchange processes is indicated by the hatched histogram.

7.2.5 Uncertainties of the model prediction

Variations of the renormalisation and factorisation scale μ by a factor 2 and 0.5 lead to changes in the predicted cross sections of about 25% in average and up to 50% at $z_{I\!P} > 0.6$. The variations are shown in Fig. 7.14. For direct photon processes, the dijet cross section is proportional to α_s and a change of about 15% occurs through the variation of $\alpha_s(\mu^2)$.

7.3 Survival probability in diffractive dijet photoproduction

To measure the gap survival probability in diffractive dijet photoproduction, one would in principle like to compare measurements of dijet production in diffractive DIS and photoproduction directly. However, the regions of the phase space covered by the detector are different in DIS and photoproduction. The electron scattering angle is much larger in DIS which leads to a tilt of the photon-proton axis with respect to the beam axis. In photoproduction, the γp axis is almost parallel to the beam axis. Therefore, the detector acceptance for the particles produced in the hard subprocess within the photon-proton system is different. These phase space effects can be evaluated with Monte Carlo models. To correct for the phase space effects one has to use a model which describes the measurement in DIS as closely as possible, i.e. the shapes of all distributions and the normalisation. It was shown that the DIS measurement can be described by the RAPGAP implementation of the pomeron model based on pomeron parton densities obtained in inclusive DDIS up to a normalisaton factor N_{DIS} (7.6). This RAPGAP model (modified by the normalisation factor N_{DIS} to resemble the DIS measurement) is then used to make a prediction for diffractive dijet photoproduction. The difference between this prediction and the photoproduction measurement is attributed to the gap survival probability. Therefore, the gap survival probability S in photoproduction relative to DIS in diffractive dijet processes is given by

$$S = \frac{1}{N_{\mathrm{DIS}}} \left.\frac{\mathrm{data}}{\mathrm{model}}\right|_{\gamma p} = \frac{\left.\frac{\mathrm{data}}{\mathrm{model}}\right|_{\gamma p}}{\left.\frac{\mathrm{data}}{\mathrm{model}}\right|_{\mathrm{DIS}}} = 0.89 \pm 0.15 \text{ (exp.)}. \tag{7.7}$$

in which the ratio determined in photoproduction (7.3) is used. The uncertainty is estimated by adding the total experimental errors which are not correlated between the two measurements in quadrature. The systematic uncertainties related to the rapidity gap selection (6%), the smearing across $M_Y = 1.6$ GeV (5%), the FMD noise (1.3%) and the luminosity calculation (2%) cancel in this ratio.

The model dependencies on the factorisation and renormalisation scales cancel to large extend when the pomeron and photon parton densities are taken at the same scale ($\mu = \sqrt{p_T^2 + m^2}$) in DIS and photoproduction. This approach is adopted here. The probability is largely independent of the pomeron parton densities used in the model. Within the quoted uncertainty, the same value is obtained if, e.g., the H1 fit 2 densities are used. The survival probability depends however on the correction of the phase space effects which are determined from the resolved pomeron model as implemented in RAPGAP.

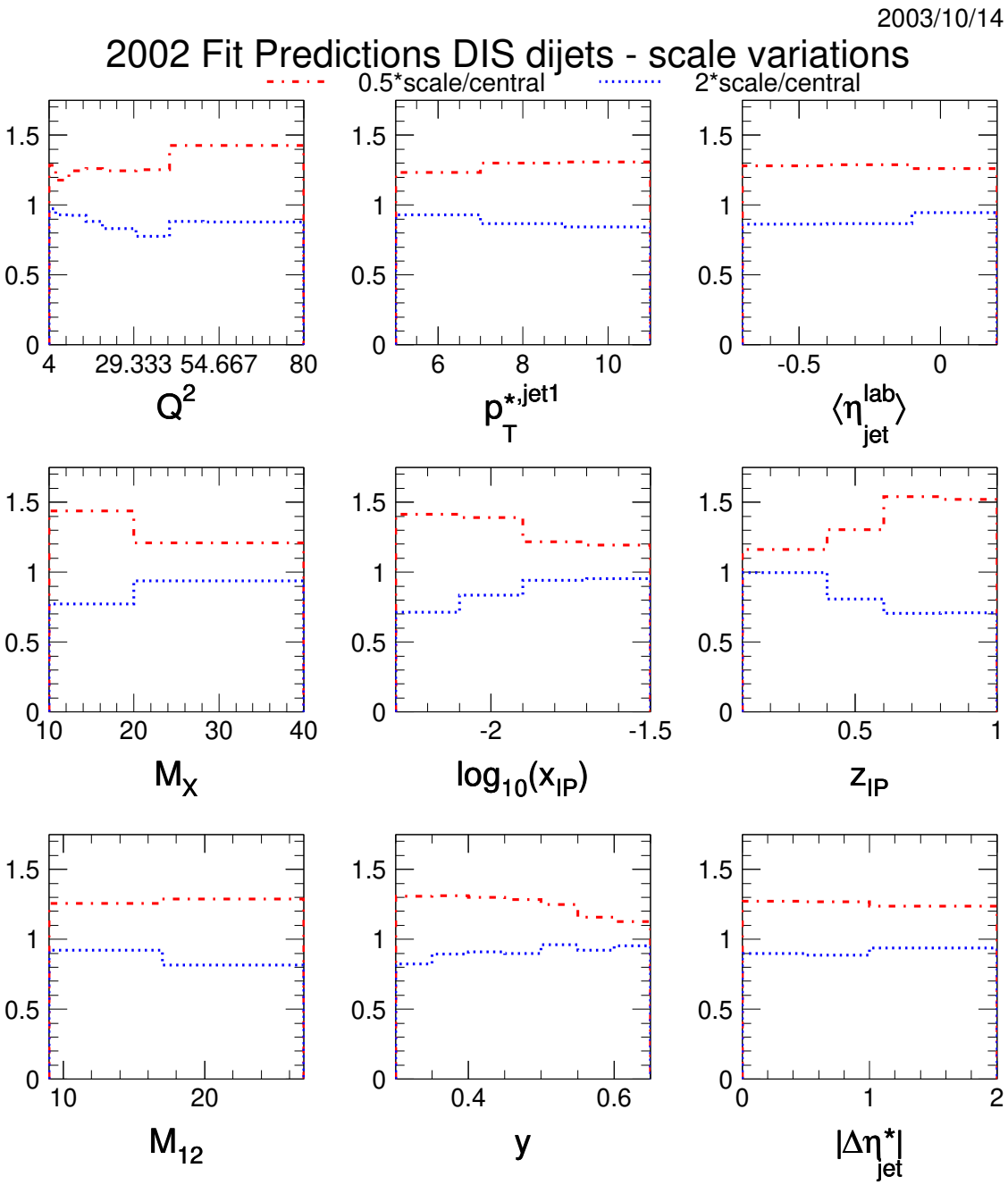

Fig. 7.14. Dependence of the model predictions based on the H1 fit 2002 pomeron parton densities on the factorisation and normalisation scale μ. Shown are the ratios of the RAPGAP predictions with the scale $\mu = 2\sqrt{p_T^2 + m^2}$ (dotted) and $\mu = 0.5\sqrt{p_T^2 + m^2}$ (dash-dotted) to the prediction with $\mu = \sqrt{p_T^2 + m^2}$.

At the present level of experimental accuracy, no significant suppression in photoproduction is observed. This result for diffractive photoproduction dijets is to be compared to a survival probability of about 0.1 for single diffractive dijet production at the Tevatron. The fact that no significant suppression is seen in photoproduction could be related to the much smaller centre-of-mass energy $W \approx 200$ GeV compared to 1.8 TeV at the Tevatron.

7.4 Summary and outlook

Cross sections are presented for the diffractive production of two jets in the photoproduction regime $Q^2 < 0.01$ GeV^2. Compared to previous H1 measurements, the luminosity is increased by one order of magnitude to $L = 18$ pb^{-1}. The inclusive k_T algorithm is used to identify events with at least 2 jets with transverse energies larger than 5 GeV and 4 GeV. Differential cross sections are measured for various characteristic variables. Pomeron parton densities determined in a recent H1 QCD fit to inclusive diffractive deep-inelastic scattering data lead to predictions for diffractive dijet photoproduction which describe well the shapes and the normalisation of the measured distributions. The photoproduction measurement is consistent with QCD and Regge factorisation within the experimental uncertainties.

Cross sections are also presented for the diffractive production of two jets in the deep-inelastic scattering regime $4 < Q^2 < 80$ GeV^2. The same jet algorithm as in photoproduction is used and the same kinematic cuts are applied. Differential cross sections are measured for various characteristic variables. The measured distributions are described by the resolved pomeron model with parton densities determined in a recent H1 QCD fit to inclusive diffractive deep-inelastic scattering. Within the experimental uncertainties, the DIS measurement is consistent with QCD and Regge factorisation.

At the present level of experimental and theoretical uncertainties, a consistent description of dijets in diffractive DIS and photoproduction is obtained using pomeron parton densities determined in QCD fits to inclusive diffractive DIS data. The measured dijet distributions can be compared to predictions at the NLO which will be available in the near future.

The survival probability in diffractive dijet photoproduction relative to the same process in DIS is determined by relating the two measurements with the RAPGAP Monte Carlo model to correct phase space effects. An overall scale factor for diffractive dijet photoproduction is found of 0.89 ± 0.15 (exp.), in which the uncertainty is determined from the uncertainties of the measurements only. The factor does not significantly deviate from unity at the present level of precision and no evidence is found that the factor is different for direct and resolved photon processes. Survival probability models which describe the suppression in diffractive hadron-hadron collisions at the Tevatron must describe the survival probability in diffractive photoproduction. Some of these models predict that resolved photon processes in photoproduction are suppressed which is not observed. The presented measurement can therefore lead to refined models which can be used to obtain improved predictions for Higgs production in double diffractive processes at the LHC.

For the future, more precise measurements based on larger event samples can be expected. The HERA collider has been upgraded and can now deliver an even higher

luminosity. A new forward proton spectrometer has been installed in H1 which will be used to measure elastic proton events. In these diffractive events, the background from standard DIS or photoproduction background is small. A diffractive jet analysis of the remaining H1 data sets obtained during the years 1999–2000 is presently ongoing. With this increased statistics, it is possible to study diffraction in multi-jet events which are sensitive to NLO corrections.

Bibliography

[1] T. Regge, Nuovo Cim. **14** (1959) 951;
T. Regge, Nuovo Cim. **18** (1960) 947.

[2] G. Ingelman, P. Schlein, Phys. Lett. **B152** (1985) 256.

[3] H1 Collaboration, paper 980 submitted to 31. Intl. Conf. on High Energy Physics, ICHEP 2002, Amsterdam.

[4] J. Collins, Phys. Rev. **D57** (1998) 3051
and erratum ibid. **D61** (2000) 019902.

[5] H. Jung, Comp. Phys. Commun. **86** (1995) 147.

[6] M. Bengtsson, T. Sjöstrand, Z. Phys. **C37** (1988) 465.

[7] T. Sjöstrand, Comp. Phys. Commun. **39** (1986) 347;
T. Sjöstrand, M. Bengtsson, Comp. Phys. Commun. **43** (1987) 367.

[8] J. Owens, Phys. Rev. **D30** (1984) 943.

[9] M. Glück, E. Reya, A. Vogt, Phys. Rev. **D46** (1992) 1973;
M. Glück, E. Reya, A. Vogt, Phys. Rev. **D45** (1992) 3986.

[10] H1 Collaboration, Phys. Lett. **B483** (2000) 36.

[11] G. Schuler, T. Sjöstrand, Z. Phys. **C68** (1995) 607;
G. Schuler, T. Sjöstrand, Phys. Lett. **B376** (1996) 193.

[12] H1 Collaboration, Eur. Phys. J. **C13** (2000) 397.

[13] A. Kwiatkowski, H. Spiesberger, H. Möhring, Comp. Phys. Commun. **69** (1992) 155.

[14] T. Sjöstrand *et al.*, Comp. Phys. Commun. **135** (2001) 238.

[15] H. L. Lai *et al.*, Eur. Phys. J. **C12** (2000) 375.

[16] M. Glück, E. Reya, A. Vogt, Z. Phys. **C67** (1995) 433.

[17] B. List, Diploma Thesis, Techn. Univ. Berlin, Germany, (1993), unpublished;
B. List, A. Mastroberardino, DIFFVM: A Monte Carlo Generator for diffractive processes in *ep* scattering in Monte Carlo Generators for HERA Physics, A. Doyle, G. Grindhammer, G. Ingelman, H. Jung (eds.), DESY-PROC-1999-02 (1999) 396.

[18] H1 Collaboration, C. Adloff *et al.*, Eur. Phys. J. **C20** (2001) 29.

[19] H1 Collaboration, C. Adloff *et al.*, Z. Phys. **C76** (1997) 613.

[20] T. Affolder *et al.*, Phys. Rev. Lett. **84** (2000) 5043.

[21] F. Abe *et al.*, Phys. Rev. Lett. **78** (1997) 2698;
T. Affolder *et al.*, PRL**84** (2000) 232.

[22] M. Derrick *et al.*, Z. Phys. **C76** (1997) 613;
M. Derrick *et al.*, Phys. Lett. **B356** (1995) 129;
M. Derrick *et al.*, Eur. Phys. J. **C1999** (43) 129.

[23] A.B. Kaidalov, V.A. Khoze, A.D. Martin, M.G. Ryskin, Eur. Phys. J. **C21** (2001) 521.

[24] A. Edin, G. Ingelman, J. Rathsman, Phys. Lett. **B366** (1996) 371;
A. Edin, G. Ingelman, J. Rathsman, Z. Phys. **C75** (1997) 57.

[25] C. Adloff *et al.*, Eur. Phys. J. **C6** (1999) 421.

[26] P. Bruni, G. Ingelman, Proc. of the Europhysics Conference, Marseilles, France, July 1993, 595;
see also `http://www3.tsl.uu.se/thep/pompyt/`.

[27] J.L. Augneres *et al.*, HERA A Proposal for a large Electron-Proton Colliding Beam Facility at DESY, DESY HERA 81/10, 1981.

[28] H1 Collaboration, The H1 Detector at HERA, Internal Report DESY H1-96-01, 1996.

[29] T. Nicholls *et al.*, Nucl. Instrum. Methods **A374** (1996) 149.

[30] H1 Collaboration, ELAN working group, internal communication (2000).

[31] S. Caron, PhD Thesis, RWTH Aachen, 2002.

[32] J. Meyer (ed.), Guide to Simulation Program H1SIM, H1 Software Notes 03-11/89.

[33] R. Brun, et. al., *GEANT Long Writeup,* CERN Program Library **W5013**, 1994.

[34] S. Levonian, Help for the e-tagger related analyses,
`http://www-h1.desy.de/~levonian/QPETAC.html`.

[35] H1 Collaboration, C. Adloff *et al.*, Z. Phys. **C74** (1997) 221.

[36] S. Ellis, D. Soper, Phys. Rev. **D48** (1993) 3160;
S. Catani, Y. Dokshitzer, M. Seymour, B. Webber, Nucl. Phys. **B406** (1993) 187.

[37] F.-P. Schilling, PhD Thesis, Univ. Heidelberg, 2001.

[38] P. Thompson, PhD Thesis, Univ. Birmingham, 1999.

[39] G. Gustafson, Phys. Lett. **B175** (1986) 453.

[40] G. Ingelman, Proc. of the HERA workshop Vol. 3, W Buchmüller, G. Ingelman (eds.), DESY (1992) 1366.

[41] S. Schenk, Diploma Thesis, Univ. Heidelberg, 2003.